

JAN EVANGELISTA PURKYNĚ UNIVERSITY IN ÚSTÍ NAD
LABEM

FACULTY OF SCIENCE

DEPARTMENT OF PHYSICS

Doctoral Thesis

ADVANCED MHD MODELLING OF PLASMA PROCESSES IN SOLAR PHYSICS

Author: *Mgr. Jan Skála*

Study branch: *Computer methods in science and technology*

Supervisor: *Mgr. Miroslav Bárta, Ph.D*

Advisor: *RNDr. Michal Varady, Ph.D*

ÚSTÍ NAD LABEM 2015

Herewith I declare that I have not used this work or any part thereof to obtain any other academic degree. I also declare that I have worked out this Thesis myself and I have used only those literature sources that are cited in the list of references.

Göttingen, April 28, 2015

Jan Skála

First of all, I would like to express my sincere gratitude to Dr. Miroslav Bárta, who has been my supervisor since the beginning of my study. He provided me with many helpful suggestions, important advice and constant encouragement during the course of this work; it has been a great honor for me to work under his supervision. I would also like to thank Dr. Michal Varady for important advices and great help with finalizing thesis, Pavel Petrus for help with correction of thesis and last but not least Dr. Michael Rouha for valuable discussions. Further, I would like to express my gratitude to my alma mater, Faculty of Science, and the Department of Physics, for trust and support. Next thanks go to Markus Rampp, Fabio Baruffa and Bernhard Bandow for the advices in HPC and code optimizations. Moreover, I would like to thank Jörg Büchner for giving me the opportunity to work at Max Planck Institute for Solar System Research and for many valuable advices. My deepest gratitude goes to my family for their unbroken support throughout my life. Finally, I would like to convey thanks to all the others who have helped and inspired me during my doctoral study. The sources of financial funding are acknowledged at the end of thesis.

Contents

1 Sun and solar activity	4
1.1 Structure of the Sun	4
1.2 Solar activity	5
1.3 Solar flares	6
1.3.1 'Standard' flare scenario	6
1.3.2 SOC flare model	8
2 Magnetic reconnection	11
2.1 Sweet-Parker reconnection model	12
2.2 Petschek reconnection model	13
2.3 2D vs. 3D reconnection	14
2.4 Cascading reconnection and multi-scale processes	15
3 Description of magnetized plasmas	18
3.1 Kinetic theory	18
3.2 Two fluid description	19
3.3 MHD	24
4 Least Squares Finite Element Method	27
4.1 Motivation	27
4.2 Formulation of LSFEM	29
4.3 Boundary conditions	30
4.4 The LS solution of overdetermined systems	31
4.5 Natural coordinate of triangular element	32
4.6 Natural coordinate of tetrahedral element	34
4.7 Coordinate transformation	35
4.8 Basis functions	36
4.9 Time discretization and linearization	40
4.10 Element-by-Element	42
4.11 Gaussian quadrature	43
4.12 Iteratively re-weighted LSFEM	45
4.13 LSFEM implementation of MHD	46
4.14 Influence of overdetermined system	48
4.15 Parallelization	50
4.16 2D Burgers' equation	52
4.17 3D Burgers' equation	55
5 Results	60
5.1 Ryu-Jones ideal MHD test	60
5.2 Tang-Orszag ideal MHD test	61
5.3 Resistive decay of cylindric current	62

5.4	Mesh refinement	64
5.5	Magnetic field reconnection	65
5.6	Parallel scaling	68
6	Discussion and conclusions	70
7	Appendix	72
7.1	MHD equations	72
7.2	Dimensionless 3D MHD equations	73
7.3	Conjugate Gradient Method	74
7.4	Preconditioned Conjugate Gradient Method	74
7.5	MHD operator	75
7.6	Table of basis functions	81
	Bibliography	87

Introduction

The Sun is the nearest star which supply energy to our Earth. This energy is the by far greatest energy source for the Earth. However, influence of the Sun to its vicinity, including Earth, is multifold and more complex.

From the observations performed by a naked eye, the Sun looks like a static object. On the other hand, many dynamical processes can be revealed when we use more sophisticated instruments. Collection of such dynamical phenomena – commonly referred to as *solar activity* – changes quasi-periodically in the well-known *eleven years cycle* (see, e.g., Usoskin, 2008, and references therein). Some of these processes have a big impact to the interplanetary space, and – consequently – to the Earth and its vicinity.

As the modern human civilization becomes more dependent on advanced technologies, which frequently use sensitive electronics, satellite/space devices or global communications, some aspects of our broader natural environment, which were out of scope of our interest in the past, become significant now. Namely, rapidly varying Earth's magnetic field, beams of high-energy particles, strong decimetric radio emission, or ionospheric disturbances can cause damages on electric power lines, communication networks and satellites, jeopardize astronauts in space and even crews and passengers of the flights over polar regions, or cause malfunctions in navigation systems, respectively. The parameters of our broader vicinity (ionosphere, magnetosphere, or near-space plasma) and their dynamical variations are now commonly called *space weather* (see, e.g., the review by Gopalswamy, 2007, 2009).

From the above mentioned reasons predictions of the space weather have increasing significance as the knowledge of approaching disturbance can be – similarly as in case of the 'classical' tropospheric weather – used for minimizing potential damages. Since the solar activity – namely solar flares accompanied often by a coronal mass ejections (CMEs) – is the dominant driver of the space weather, deep understanding of the nature and underlying physics of the solar eruptive processes is a key to desired space-weather predictions. Thus, research in solar physics is not of purely academic interest but has also important applications.

On the other hand, since the solar atmosphere is in highly ionized state, the active phenomena observed at the Sun represent manifestation of many basic plasma processes, among them the reconnection of magnetic field lines. The Sun can be thus considered as a large plasma-physics laboratory and relations between our models of dynamical solar processes and their observations as a test bed for basic theoretical concepts in plasma physics. For example, the above mentioned magnetic reconnection is not only supposed to be a key process of energy release in solar flares but plays important role also in the fusion, laboratory, and space/astrophysical plasmas. Indeed, many theoretical concepts, which appeared first in the context of solar physics, were applied later, e.g., for explanation of X-ray flares observed in accretion discs around black holes. Hence, understanding of plasma processes in the solar atmosphere brings us much general knowledge largely exceeding the frontiers of solar physics.

Generally speaking, the fundamental principles of dynamics of magnetized plasmas as an ensemble of charged particles based on the Maxwell's electromagnetic-field theory and Einsteins special relativity are known for more than hundred years. Nevertheless, enormous complexity prevents us to make almost any sensible prediction about evolution of large-scale plasmatic

systems from *ab initio* calculations. Therefore, using various simplifying assumptions, more applicable approaches have been developed. Among them the magnetohydrodynamics (MHD), the approach, which handles plasma as a single magnetized fluid, is widely used in the context of astrophysical/space plasmas since it is – in spite of its constraints rooted in many simplifications and assumptions – so far only plausible description of magnetoplasma dynamics at huge scales, which we are facing when handling astrophysical plasma problems. Nevertheless, even the MHD approach, though reducing the complexity a lot, represents a great challenge when applied to physical systems found in nature, e.g., to the dynamical processes in the solar atmosphere in our case. The governing equations – a set of MHD partial differential equations – represents highly non-linear, mixed advection/diffusion problem whose analytical treatment is possible only in a few exceptional cases. Therefore, set of the MHD equations – representing the initial-value problem – is most usually handled numerically, by means of computer simulations.

However, many problems in physics are inherently of multi-scale nature. The issue of MHD processes in the hot and sparse, almost collision-less plasmas, can stand as clear example. Namely, the huge gap between the characteristic size of structures, where the magnetic energy is accumulated, and the scales where the energy dissipation takes place (via kinetic processes), represents a fundamental problem. This is, in particular, quite challenging for numerical treatment of MHD system since the numerical approach is inherently discrete, with a limited number of mesh points. For a homogeneous structured mesh the number of grid points in one dimension is clearly given by the ratio between the size of the entire computational box and the size of the grid cell. Hence, for affordable number of grid cells, the scale separation is far from required value. Fortunately, the small-scale dynamics does not occupy entire simulation domain but usually it is concentrated into much smaller subspace. This allows selective increase of resolution just in the regions where small-scale dynamics takes place. Technique, widely applied in finite-difference based numerical methods for this sake, is known as *Adaptive Mesh Refinement* (AMR). Nevertheless, this method has its own drawbacks related to the (artificial) boundaries between the fine and coarse meshes. Therefore, it worths searching for different approach which lacks this problem.

The Finite Element Method (FEM) with self-adaptive gridding appears to be such appropriate numerical implementation for handling the broad range of scales contained in many MHD systems. It is based on an unstructured mesh and thus no artificial boundaries are introduced by numerics to the studied system. Moreover, in addition to the adaptive mesh refinement also the order of the functions interpolating the solution over given element can be dynamically changed (so called h-p refinement), which increases flexibility of the solver and, consequently, the fidelity of the numerical solution. And just this approach, its numerical implementation, and application to the selected test problems as well as the numerical study of magnetic reconnection in large-scale problems (e.g., solar flares), represents core of the presented work.

From various FEM formulations we have chosen the least-squares FEM (LSFEM) because it is robust, universal (it can solve all kinds of partial differential equations) and it is efficient – it leads always to the system of linearized equations with symmetric, positive definite matrix Jiang (1998). The LSFEM keeps many key properties of Rayleigh-Ritz formulation even for systems of equations for which the equivalent optimization problem (in Rayleigh-Ritz sense) does not exist Bochev and Gunzburger (2009).

Despite the FEM applications in the fluid dynamics made a substantial development in the past years and is now routinely used in the engineering practice, its usage for numerical solution of MHD equations is still rather rare. For example, the NIMROD Sovinec et al. (2004) and M3D codes Jardin and Breslau (2005) – based on the Galerkin formulation – belong to a few known implementations of FEM-based MHD solvers. Related work has been done also by Lukin (2008) who implemented the MHD (and two-fluid) equations within a more general code framework SEL Glasser and Tang (2004) based on the Galerkin formulation with high-order Jacobi polynomials as the basis functions. However, the LSFEM implementation of MHD solver

described in the current work is the first attempt of this kind.

The work is organized as follows: In order to introduce the reader into the research context in which the developed numerical code is being applied, the first chapter describes briefly the Sun and solar activity, namely solar (eruptive) flares. The process of magnetic reconnection, accepted now commonly as a key mechanism of energy release in the solar flares and its various aspects represents the main subject of the second chapter. In the third chapter, the set of MHD equations in the general flux/source (conservative) form (i.e. suitable for numerical integration) is rigorously derived from the first principles, showing all the assumptions that need to be taken into account. Then, the properties of least-square formulation of FEM are summarized, focusing on the temporal discretization, reduction to the first-order system, and linearization procedure. Some practical arrangements of the LSFEM implementation of the MHD solver follows. Finally, the code is tested on a couple of standardized model problems and the results are discussed with respect to the intended application of the code to the current-layer filamentation and decay during the magnetic reconnection in solar flares.

Partial results of this work has already been published in a couple of papers co-authored by the candidate: Skála et al. (2015), Skála et al. (2011), Skála and Bárta (2012) and Bárta et al. (2011b). Presented thesis represents extended synthesis of the candidate's own contribution and its incorporation into the framework of the current research in numerical modelling of plasma processes in solar active phenomena.

Chapter 1

Sun and solar activity

The main aim of this work is development of an advanced FEM-based MHD code capable to handle complex multi-scale problems and its application to the open question of contemporary solar physics, namely the issue of magnetic reconnection in the solar flares. In order to introduce the reader into context, in which the MHD numerical modelling is going to be used, let us briefly summarize a couple of basic facts about our Sun and its activity (see, e.g., Aschwanden (2005), Goedbloed and Poedts (2004), Kirk et al. (1994)).

1.1 Structure of the Sun

From the point of view of the classical astrophysics the Sun is a normal star of spectral type G2V on the Main Sequence of the HR diagram approximately in the middle of its lifetime. Based on physics, the Sun can be divided into several layers according to the processes which there dominate – see Fig. 1.1. In the center of Sun is a *core* where the energy is produced by a nuclear fusion. The main fusion process is proton-proton chain, this process converts hydrogen into helium. During the fusion process, the energy is mainly released in the form of a heat and photons (gamma rays and X-rays). The size of core is 20% – 25% of a solar radius. The temperature goes up to the 15×10^6 K and density 1.5×10^5 kg.m $^{-3}$.

Below about 70% of a solar radius is a *radiative zone*. There, a solar material is hot enough that a thermal radiation is sufficient to transfer an intense heat from the core outwards – opacity of the solar plasmas is quite low under those conditions. Therefore, the temperature gradient is not sufficient to promote convective instability. The temperature of radiative zone varies from 7×10^6 to 2×10^6 K. The density is $20 - 0.2$ kg.m $^{-3}$.

Above the radiative zone there is *convective zone* which reach the surface of the Sun. When we are approaching to the surface, the temperature and density decrease. Such conditions do not allow an efficient radiative transfer. Instead of radiative transfer the energy is delivered to the surface by convective flows. The temperature of convective zone is $2 \times 10^6 - 6 \times 10^3$ K and the density is $2 \times 10^{-1} - 2 \times 10^{-4}$ kg.m $^{-3}$.

The visible surface of Sun is called *photosphere*. Above the photosphere most of the light can escape to the space (almost) without absorption. The photosphere is tens to hundreds of kilometers thick. The photosphere light spectrum more or less corresponds to the black body radiation with temperature around 5700 K. The density is approximately 10^{-4} kg.m $^{-3}$. The photosphere is covered by a convection cells – granules. The typical horizontal size of granules is 10^6 m and life time is about 5 min.

Upper layers of the solar atmosphere consist of chromosphere, transition region and corona. The *chromosphere* layer about 2000 km thick is visible only during total eclipses like a colored ring when the solar disc is covered by the Moon and a glare photosphere is hidden. The temperature increases gradually with altitude from the temperature minimum related to the temperature of photosphere up to around 2×10^4 K. The particle density is approximately

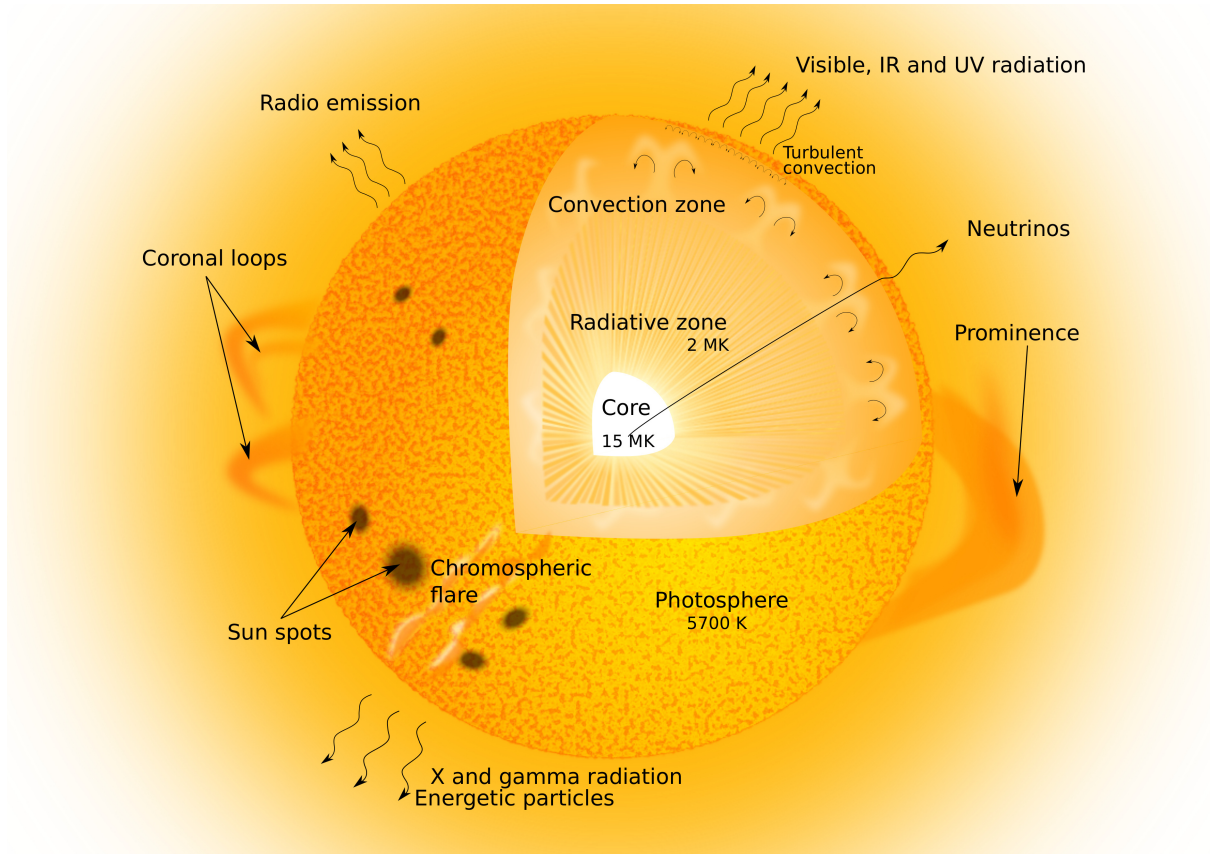


Figure 1.1: Structure of the Sun.

10^{16} m^{-3} (mass density $\sim 10^{-11} \text{ kg.m}^{-3}$).

The *transition region* is the thinnest layer of atmosphere. It represents an interface between the chromosphere and the corona. On the distance of hundreds kilometers, the temperature rises rapidly from around $2 \times 10^4 \text{ K}$ in the upper chromosphere to coronal temperatures closer to 10^6 K , so the temperature gradients in the transition region are very steep, almost forming a discontinuity. The hydrogen number density changes from the chromospheric values 10^{16} m^{-3} (on top of chromosphere) to the coronal values $\sim 10^{14} - 10^{15} \text{ m}^{-3}$.

The *corona* is formed by hot $\sim 10^6 \text{ K}$ and low density $\sim 10^{14} - 10^{15} \text{ m}^{-3}$ plasma which is completely transparent for basically all wavelengths. The corona fills much larger volume than the rest of the Sun and continuously expands into space forming the solar wind. Steep increase of temperature to the solar corona remains as one of the open questions in the current solar physics.

1.2 Solar activity

The Sun, as the closest star to the Earth, represents the far most important source of energy for the Earth's ecosystem. It is well known that the Sun is not a quiet star, but due to the presence of variable magnetic fields, solar atmosphere represents a very active environment. There are many different manifestations of activity in the solar atmosphere: Active regions located around sunspots can host prominences, solar flares, or coronal mass ejections (CMEs), one can detect variability in the solar wind parameters etc. Due to the extreme energy releases related to some kinds of the solar activity, not only the atmosphere of the Sun, but also the vicinity of the star including the surroundings of the Earth and the life conditions on the planet itself, can

be affected by such events. The influence is now known as the space weather. The impact of the processes is further magnified by the existence of advanced technologies, human civilization relies on, and which are particularly liable to be influenced by the space weather. Therefore there is a growing interest in the essentials of the energetic processes in the solar atmosphere which is reflected by a large number of expensive space missions devoted to the observations of the Sun.

The most prominent events in this sense are the solar eruptive flares on which we focus in the following.

1.3 Solar flares

Solar flare is process associated with rapid energy release in the solar corona – it is the biggest explosion in the solar system. Now, it seems to be clear that the primary source of energy for solar flares is the energy deposited in the coronal magnetic fields and related current density systems. The trigger mechanism that starts the flare is not yet completely clear and even it seems that there are more types of solar flares with different causes. At least two subclasses are commonly mentioned: The *eruptive flares* connected with a filament eruption and subsequent Coronal Mass Ejections (CMEs) and so called *compact flares*. However, regardless of the type of instability that starts the process and actual configuration, most of the current models employs *magnetic reconnection* (see 2 as the key mechanism for conversion of magnetic energy into other forms. Such an energy release process results in acceleration of non-thermal particles and in heating of coronal and chromospheric plasma. These processes finally lead that radiation is emitted in almost all wavelengths: radio, white light, UV/EUV, soft X-ray, hard X-ray, and even γ -rays in the cases of large flares. Figure 1.2 shows the active region NOAA 11429 with X5.4 solar flare from March 7th, 2012 in the EUV. The flash from rapid energy release is clearly visible in the middle of the image. The magnitude classification of solar flares is based on the soft X-ray observations of the Sun in the 1-8Å band by satellites. The magnitude of flares are denoted by the letter – A,B,C,M and X – corresponding to the power of 10: -8,-7,-6,-5,-4, respectively, of the peak emission flux. The second part of classification is number that act as a multiplier. For example the flare X5.4 correspond to 10^{-4} , from X, times 5.4 then the peak emission flux in the band 1-8Å is $5.4 \times 10^{-4} \text{ W.m}^{-2}$. More details and another possible classification can be found in the work of Cliver (2000). The energy released during solar flares is enormous – it can reach energy 10^{25} J (e.g. Hudson and Willson (1983); Emslie et al. (2005)).

From the observational point of view, the solar flares are quite enigmatic phenomena. They exhibit (at least the eruptive flares) *well organized large-scale dynamics* with long-distance coherence manifested, e.g., by the regular structures such as the arcade of the flare loops visible in UV/EUV radiation, and signatures of multi-site, small-scale and highly time-variable *fragmented energy release* at the same moment. Based on these observations, two main classes of the models of solar flares were developed, stressing one or the other of those aspect of observations.

1.3.1 'Standard' flare scenario

The evolution of the flare theoretic model is several decades old. The most widely accepted – so called *standard scenario* – for flares employs magnetic reconnection in the global current layer formed behind the erupting flux rope/filament. The model evolved from the concepts of Carmichael (1964), Sturrock (1966), Hirayama (1974), Kopp and Pneuman (1976), and is now frequently referred as the *CSHKP* model according to the initials of the five authors (see, e.g., Shibata (1998) and references therein). The CSHKP model fits well with the observed large-scale dynamics of the eruptive flares and has a well-understood and described theoretical foundation (see, e.g. Mandrini (2010); Magara et al. (1996); Shibata and Tanuma (2001) and

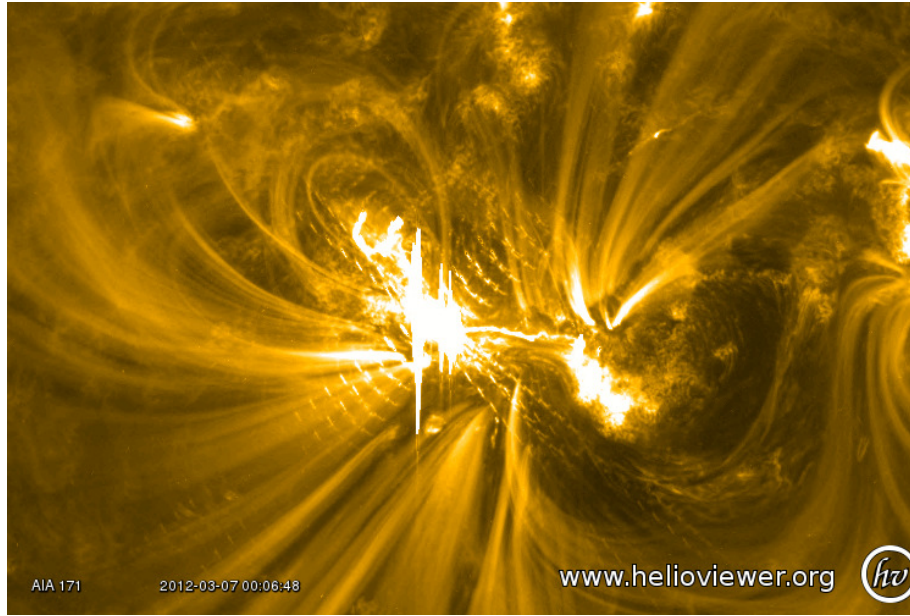


Figure 1.2: The active region 11429 during X5.4 solar flare. The data are obtained by SDO AIA in wavelength 171Å.

references therein).

The initial impulse of the flare process is a rising twisted filament/prominence above the neutral line in a flare active region (see Fig. 1.3). The rising filament stretches and extends a current sheet above the neutral line, which is consequently prone to magnetic reconnection. The change of connectivity of the magnetic field lines adds more flux to the rising filament and increases its magnetic pressure. A lower loop arcade is formed below the reconnection region. The filament continues rising until it reaches a state where no equilibrium is possible and the originally slow reconnection becomes fast. The filament accelerates and erupts. The magnetic reconnection is accompanied by lateral inflow of plasma from both sides of current sheet. The X-type reconnection region is assumed to be the location of major magnetic energy dissipation, which heats the local coronal plasma and accelerates non-thermal particles. These two processes produce thermal conduction flows and precipitating particles which both heat the chromospheric footpoints (places where the coronal loop enters into the dense chromosphere) of the newly reconnected field lines. When energetic particles reach chromosphere, hard X-rays are emitted by bremsstrahlung. As a result of this impulsive and fast heating, chromospheric plasma evaporates and fills the newly reconnected field lines with dense heated plasma. The hot flare loops produce soft X-ray radiation and EUV.

The first particular evidence for the standard flare scenario was observed with the Yohkoh satellite and presented by Tsuneta et al. (1992). In their paper the consecutively rising flare loops are shown. The apex of the SXR loops rises while the footpoint separation increases. The complex temperature structure of the X-ray loop suggested that the magnetic reconnection process is located near to the top of the loop. Forbes and Acton (1996) showed that newly reconnected cusp loops shrink and relax due to magnetic tension. Hanaoka et al. (1994) observed a prominence eruption and coronal brightening. The elongated magnetic field reconnects below the prominence and the reconnected magnetic field creates an arcade of closed loops according to CSHKP model. The observations with SOHO/LASCO revealed many evidences of flux rope and disconnection events (e.g. Dere et al. (1999); Simnett et al. (1997)). Yokoyama et al. (2001) found a clear evidence for magnetic reconnection inflow in a flare on 1999 March 18. McKenzie and Hudson (1999) showed observation in 1999 January 20 by Yohkoh where many motions and structures in the region above the flare arcade are present. They interpret the data as the first

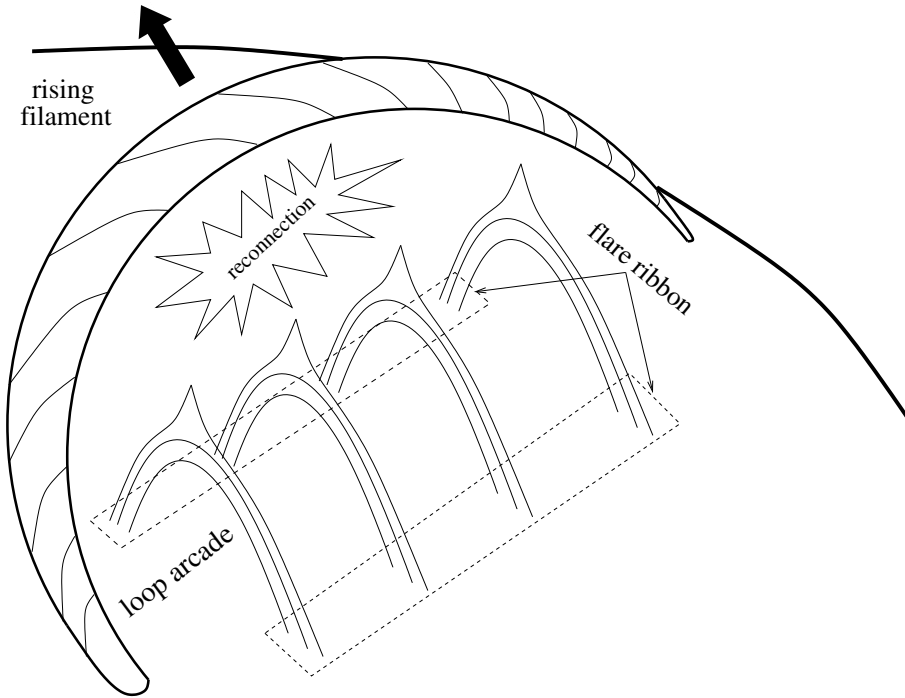


Figure 1.3: The standard CSHKP flare model. The rising filament stretches a current sheet above the neutral line and triggers the magnetic reconnection. The figure inspired by Priest and Forbes (2000).

direct evidence of high-speed flows in the region immediately above flare loops. Czaykowska et al. (1999) and Harra et al. (2005) found up-flowing plasma along the outer edges of flare ribbons, while down-flows were seen in the inner ribbon edges. Magara et al. (1996) performed 2D MHD simulation of cusp-type flare and they found a high temperature and density region at the loop top, which is heated by slow shocks. It is in good agreement with hard X-rays discovered in the impulsive flares.

All the above observations of the large-scale dynamics strongly support the CSHKP model. However, there are two observational facts that are difficult to explain in the frame of the standard flare scenario that is based on the reconnection in a single global current layer. First of all, the classical CSHKP flare model presumes a single X-line (or X-point in 2D projection), where the field lines reconnect, surrounded by the dissipation region with finite DC electric field. However, the number of particles accelerated in such a small region would be far too small than it is derived based on the hard X-ray (HXR) emission observed during the flares. This discrepancy is therefore known as a number problem. In addition to that, the analysis of HXR and radio data reveals that the particles are accelerated rather in many small-scale, short-living sites than in a single macroscopic region – this feature is known as fragmented acceleration or fragmented energy release (see, e.g., Vlahos (2007)). In order to reach such a qualitative nature of particle acceleration the alternative flare models, based on *Self-Organized Criticality/SOC*, have been developed.

1.3.2 SOC flare model

Because of the above described insufficiency of the CSHKP scenario to account for signatures of fragmented energy release and high efficiency of the flares as particle accelerators the standard model with the single global current layer was doubted and an alternative scenario based on the magnetic reconnection in many thin and short current layers that appear as a consequence of chaotic driving of the coronal magnetic field by the random photospheric motions was suggested

– see Fig. 1.4.

This class of models addresses mostly the issues of fragmented energy release and particle acceleration in flares. Occurrence of a large scale events in such chaotic configurations is explained by the so called avalanche principle (see below), the mechanism known from the SOC theory. Self-Organized Criticality (see Bak et al. (1987)) is a state (critical point) to which the dynamical (initially random) system naturally evolve. SOC-type models emphasize the need to explain the properties of accelerated particles – namely fragmented nature of acceleration and also large particle fluxes. The principal idea behind is rooted in the fact, that multiple small scale current sheets hosting multiple diffusion/acceleration regions are the naturally conforming idea of fragmented energy release and because of their multiplicity they provide also larger (and perhaps sufficient) acceleration volume to account for particle fluxes also quantitatively. In order to get many chaotic current sheets the SOC models involve chaotic boundary conditions: Chaos is pumped into the system via boundaries. In the case of solar flares this can be done quite naturally: chaotic photospheric motions cause random braiding of magnetic field in the corona and, consequently, many current sheets are formed there, see Fig. 1.4.

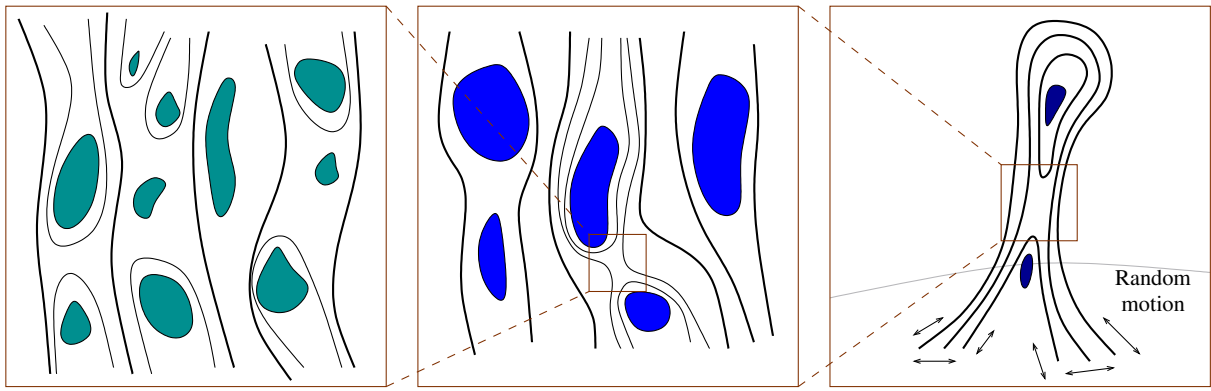


Figure 1.4: The scheme of Self-Organized Criticality flare model. The reconnection in limited small scale current sheet trigger a similar event in its vicinity provided the system is in marginally stable state. The left zoomed window shows fragmented random currents. The larger scale reconnection is triggered in the middle panel. The right window represent the global scale – flare.

It is, however, difficult to reconcile this flare scenario with a well-organized large-scale structures observed in solar flares in visible light or UV/EUV radiation as coherent flare-loop arcades, or filament eruption followed by a CME (see Fig. 1.3). As mentioned above, the answer to this issue is formulated as an avalanche principle in the frame of SOC models. The idea is, that small event (reconnection in limited small scale current sheet) can trigger a similar event in its vicinity provided the system is in marginally stable state. Then even a large scale event (large avalanche) can be eventually observed. A popular way of numerical modeling of this kind of behavior are so called cellular automaton (Bak et al. (1987)). From the global point of view such models fit very well with statistics of flare importance. Galsgaard and Nordlund (1996) performed 3D MHD simulation of initially strait magnetic field which was perturbed by boundary velocities. They found length spectrum of current sheets over whole domain ending at the resistive length scale. Vlahos et al. (2004) studied acceleration of electron and protons in the stochastic multiple small scale dissipation regions. They used 3D magnetic field extrapolated from magnetogram as a guiding field for testing particles. The modeling of unstable currents sheets was based on the extended cellular automaton (see Isliker et al. (2001) and references therein). They found extremely efficient acceleration of particles and agreement with HXR and microwave spectra from observation with theirs results. Aschwanden (2007) explore scaling laws of flare from the size of nanoflares to giant stellar flares. He shows that the power-law of

frequency distribution of flares energies can be explained by SOC model.

However, although the avalanche principle may explain even the large events and the scaling law for the flare magnitude, it is difficult to believe that it can account for the observed coherent large-scale structures (e.g., global flux ropes and arcades). Hence, modifications of the CSHKP model that would address also the physics on smaller scales are being searched. The most promising attempts include some kind of either externally driven (see, e.g. Lazarian and Vishniac, 1999) or self-generated (e.g. Shibata and Tanuma, 2001; Bárta et al., 2011b) MHD turbulence in the current sheet. This issue is going to be discussed in more details in Section 2.4.

Chapter 2

Magnetic reconnection

Magnetic field reconnection is an important physical process in plasma physics in basically all contexts from laboratory and fusion to astrophysical plasmas (see, e.g., the books by Priest (1984) and Biskamp (2000) and references therein for review). In particular, in this work we would like to stress its key significance for energy release in the solar flares as described in the previous chapter. The process is characterized by change of connectivity of the magnetic field lines. This is inherently connected with the formation of a nonzero projection of the electric intensity to the magnetic field strength, i.e. $E_{\parallel} \equiv \mathbf{E} \cdot \mathbf{B} / |\mathbf{B}| \neq 0$ in the so called *diffusion region*, where the change of magnetic topology takes place. Existence of the parallel component of electric field E_{\parallel} leads to particle acceleration and/or plasma heating, the reconnection is therefore non-ideal plasma process that involves at least partial dissipation of the magnetic energy. However, the dissipation and $E_{\parallel} \neq 0$ is not a sole characterisation of the magnetic reconnection – also specific plasma velocity field is important in order to really change the magnetic field topology, which justifies the term *reconnection* for the process. In the 2-D geometrical configurations, where the magnetic reconnection properties are most well known, the necessary condition for the change of the connectivity says that the velocity field has to cross the magnetic separatrices (see, e.g. Schindler et al., 1988; Nickeler and Wiegmann, 2012). In the 2-D geometry the reconnection forms a characteristic velocity pattern with two inflows and two outflow jets – see Fig. 2.1.

Change of the field lines connectivity is possible only if the magnetic field has some gradient. The most suitable configurations for reconnection therefore, because of the Faraday law $\mu_0 \mathbf{j} = \nabla \times \mathbf{B}$, involve current layers at which at least some component of the magnetic field changes its orientation. The mechanism of magnetic reconnection can be well illustrated in the 2-D geometrical configuration in Fig. 2.2. Situation in the panel (a) displays an equilibrium between the Lorenz force $\mathbf{j} \times \mathbf{B}$ and the pressure gradient. If a small perturbation appears, like in Fig. 2.2b, it tends to further growth as the Lorenz force along the current layer is not compensated and the shrinking magnetic field lines evacuate the diffusion region in the center. This leads to decrease of the pressure gradient and the Lorentz force acting to the plasma from above and below is no more perfectly balanced. This leads to the inflow of magnetized plasmas from the regions above and below the current layer and processing of fresh magnetic flux. As a result, the characteristic velocity pattern as seen in Fig. 2.1 appears. Continuation of the process thus represents the “engine” that converts free magnetic energy accumulated along the current layer to the plasma bulk kinetic energy and – because of presence of the parallel component of electric field in the diffusion region – also to particle acceleration and heat.

As can be seen in Fig. 2.2b, the positive feedback to the perturbation (local compression) of the current layer leads to farther thinning and eventually tearing of the current density structure. Hence, from the “current-centric” point of view the process of magnetic field line reconnection is described as *tearing instability*. Properties of this instability were studied in the classical paper by Furth et al. (1963). The critical parameter that controls the the growth rate

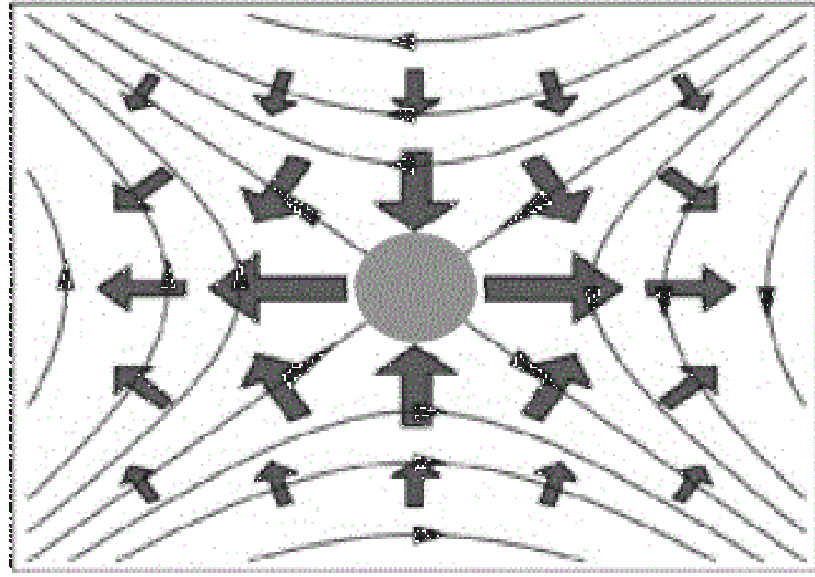


Figure 2.1: Schematic view on the magnetic reconnection process in 2D. Both non-zero electric field in the central diffusion region and characteristic flow pattern is required for magnetic reconnection to operate

of the instability is magnetic Reynolds number R_m . The Reynolds number is defined as a ratio of typical length scale times typical plasma velocity and electric resistivity $R_m = \frac{L_0 v_0}{\eta}$. In the case of high diffusion coefficient η , the Reynolds number is smaller than unity and plasma can flow across the field. This is connected with presence of parallel electric field and easy change of magnetic field line topology. In the opposite case of a weak η , the Reynolds number is greater than unity and the magnetic field is mostly frozen in the plasma and flows with it. As has been written above, during the reconnection process plasma flows into the diffusion region in directions perpendicular to the magnetic field and a current sheet bringing a new magnetic flux to be reconnected. The efficiency of the process is characterized by *reconnection rate*:

$$M_A = \frac{v_e}{v_A}, \quad (2.1)$$

where v_e is a inflow speed and $v_A = B/\sqrt{\mu_0 \rho}$ is the Alfvén velocity. The reconnection rate depends on the size of the diffusion region and overall the magnetic field settings. In the following sections, we take closer look on several reconnection regimes..

2.1 Sweet-Parker reconnection model

Sweet and Parker (Parker (1957), Sweet (1958)) introduced the first quantitative reconnection model in two dimensions and an incompressible plasma. In their model a magnetic diffusion region lies in the entire boundary of opposite magnetic fields. The diffusion region length is equal to the global external length L_e . The scheme of Sweet-Parker magnetic field and current sheet configuration is shown in the figure 2.3. The magnetic field forms characteristic shape – a magnetic field vanish in an X-like structure and create so-called X-point. The reconnection rate M_A is given by speed which magnetic field lines are entering the diffusion region. The inflowing magnetic field can be considered as uniform. The speed of plasma flowing into the diffusion

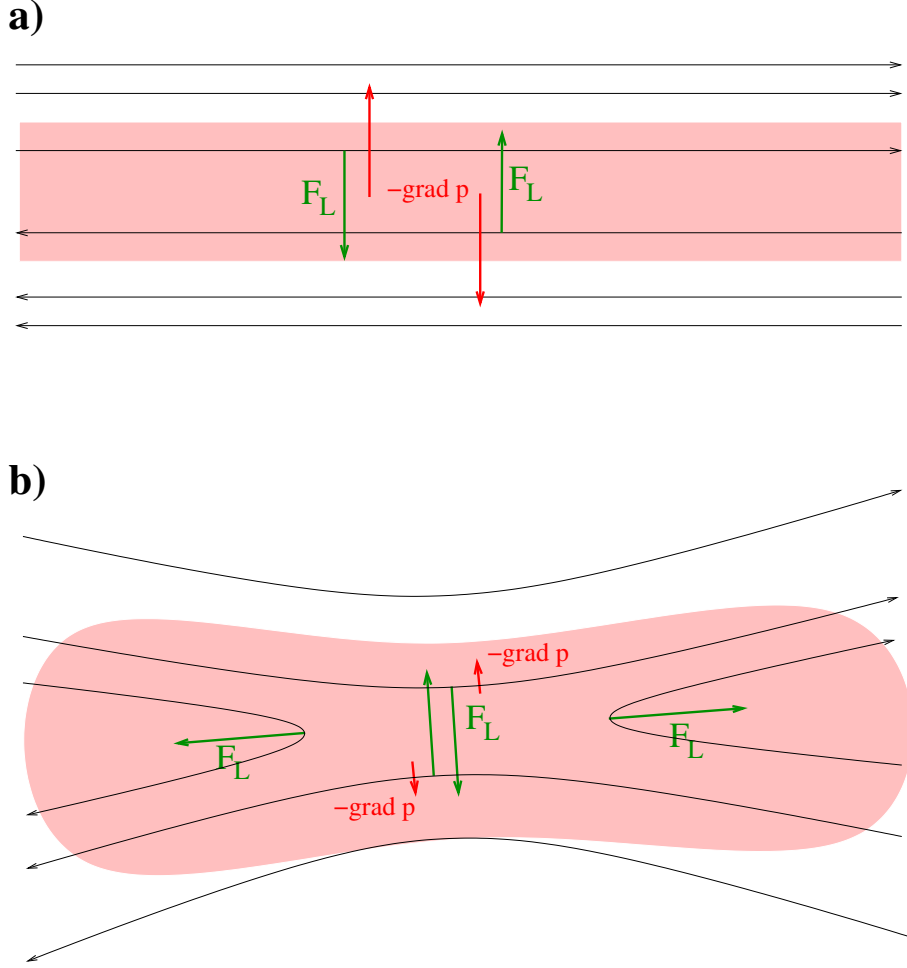


Figure 2.2: Physical mechanism of magnetic reconnection/tearing instability.

region is approximately

$$v_e = v_A S^{\frac{1}{2}}, \quad (2.2)$$

where $S = \mu_0 L_e v_A / \eta$ is the Lundquist number, representing the ratio between the time scales of resistive diffusion and typical Alfvén time and $v_A = B / \sqrt{\mu_0 \rho}$ is the Alfvén speed in the inflow region. We can put an inflow velocity into the equation for reconnection rate 2.1 and we get the Sweet-Parker reconnection rate

$$M_A = S^{-\frac{1}{2}}. \quad (2.3)$$

In the case of an astrophysical plasma S is very large $S > 10^6$ therefore the Sweet-Parker reconnection rate is too small to explain the amount of released energy during solar flares.

2.2 Petschek reconnection model

Petschek proposed a model (see Petschek (1964)) with much shorter diffusion region then in the Sweet-Parker model. The diffusion region is also thinner and the diffusion process can proceed faster. This change allows significant increase of reconnection rate. The inflowing magnetic field is nonuniform and the slow MHD shock waves are formed in the outflow regions, see figure 2.4. The most part of conversed energy comes from the shock waves which accelerate and heat the plasma to form two hot outflow jets. The Petschek's formula for the reconnection rate is

$$M_A = \frac{\pi}{8 \ln S}. \quad (2.4)$$

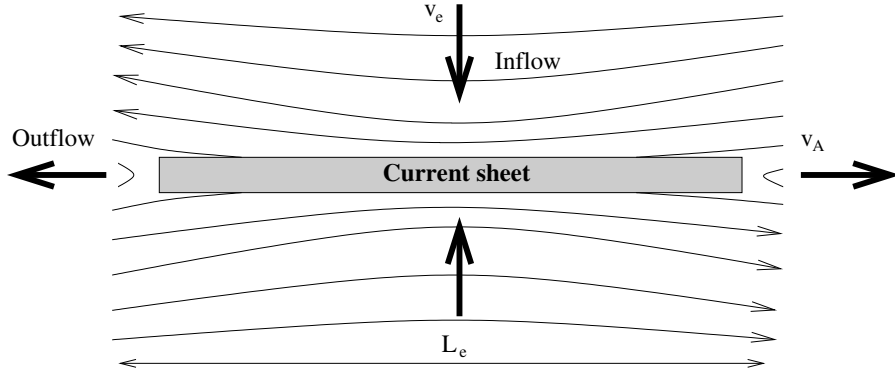


Figure 2.3: The scheme of Sweet-Parker magnetic field reconnection. The plasma inflows are located above and below a diffusion region. The length of diffusion region is equal to the global length L_e . The figure is inspired by Priest and Forbes (2000).

We see that the Petschek reconnection is much faster than the Sweet-parker rate because the rate is logarithmic dependent on S .

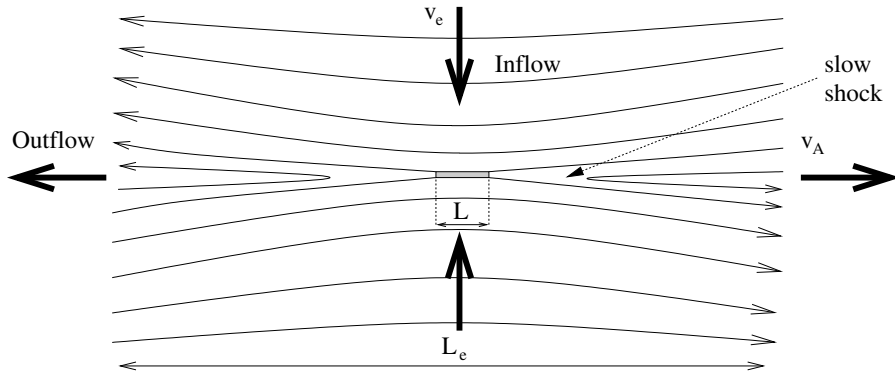


Figure 2.4: The scheme of Petschek reconnection. The length L of the diffusion region is much shorter than the global length L_e . The slow mode shock waves are propagating from sides of the diffusion region. The figure is inspired by Priest and Forbes (2000).

2.3 2D vs. 3D reconnection

Two-dimensional reconnection has been already largely developed, unfortunately, many of its concepts and definitions based on the two-dimensional models do not transfer to the three-dimensional configurations without inherent symmetry.

In two dimensions, a magnetic configuration can be separated by *separatrix curves*, which divide the plane into topologically distinct regions. In each region the magnetic field lines generally start and also end in the same region. The X-point is located at the intersection of two separatrix lines. The magnetic field vanish at the X-point and the field lines are breaking and rejoining. The magnetic flux is transferred across the separatrices from one topological region to another.

In three dimensions, we can use analogical approach. *Separatrix surfaces* are used instead of separatrix curves, see Fig. 2.5. Again similarly, the separatrix surfaces separate a volume into topologically distinct regions. A *separator* is created of the intersection of two separatrix surfaces. The separator ends at the null point (points) or on the boundary. The global structure of magnetic field called *skeleton* is a complex structure due to many sources including

null points, spine curves and separatrix fan surfaces. The *null spine* is the isolated field line which approaches or recedes from the null point. Its neighboring magnetic field lines form two opposite directed bundles which spread out as they approach the vicinity of null point. This magnetic structure is called *null fan*. The separatrix surfaces can be divided into two types. The first, separatrix fan surfaces are extensions of the fan surfaces at the null points. The second, separatrix touching surfaces are touching a boundary in a curve known as a *touch curve* or a *bald patch*.

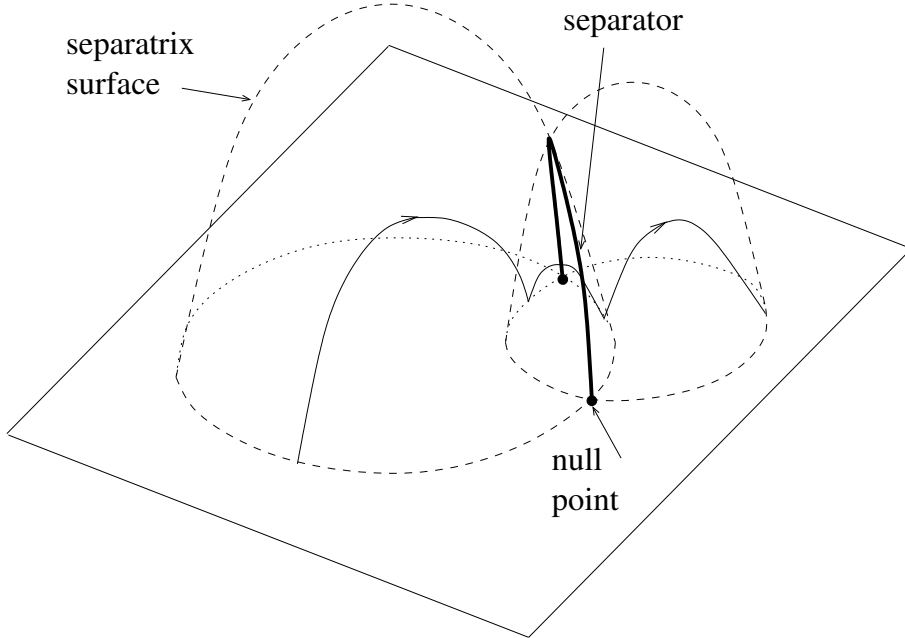


Figure 2.5: Three-dimensional separatrix surfaces intersect in a separator. The figure is inspired by Priest and Forbes (2000).

The rate of the reconnection flux is given by the following general form – the integral over measurable set of field lines

$$M_A = \int E_{||} dl, \quad (2.5)$$

where $||$ denotes component parallel to magnetic field lines. The equation 2.5 can be also assumed as a necessary and sufficient condition for a general magnetic field reconnection if it is nonzero.

2.4 Cascading reconnection and multi-scale processes

For plasma with a large magnetic Reynolds (or Lundquist) number – which is the case of solar corona and most of the space and astrophysical plasmas - the theory of magnetic reconnection faces yet another problem: There is a huge scale gap between the global scale of reconnection, where magnetic field energy is accumulated along the current layer, and the micro scale, where the energy dissipation and acceleration particles takes place (see Büchner (2006)). This can be clearly seen from the so called generalized Ohm's law for plasmas that results from the transition between kinetic/two-fluid and MHD description of plasmas (see the next chapter):

$$\mathbf{E} + \mathbf{v} \times \mathbf{B} = \eta \mathbf{j} + \frac{\eta}{\nu_c} \frac{\partial \mathbf{j}}{\partial t} + \frac{1}{ne} (\mathbf{j} \times \mathbf{B} - \nabla p_e) \quad (2.6)$$

Setting $\partial/\partial y \approx 1/\delta$ and $\partial/\partial t \approx 1/\tau_A$ one can make a simple dimension analysis in order to

see at which typical current layer thickness is the contribution to the parallel electric field from the terms on the RHS of the Ohms law comparable with the ideal term $\mathbf{v} \times \mathbf{B}$. For the case of solar coronal plasmas with low resistivity the last term describing off-diagonal components of the electron pressure tensor comes first into play (Büchner, 2006) at scales ≈ 10 m. However, the typical estimated thickness of the flare current layer is around 1000 km.

In order to bridge this enormous scale-gap Shibata and Tanuma (see Shibata and Tanuma (2001)) suggested schematic concept of *fractal* (better *cascading*) reconnection. This speculative idea has been based on observed results of many MHD simulations, which exhibited formation of magnetic islands, a.k.a. *plasmoids* in much shorter dynamic times than expected by analytical theory by Parker (1957) and Furth et al. (1963). The plasmoid formation in such early stages was unclear until *plasmoid instability* has been revealed recently by Loureiro et al. (2007, see below). Prediction by Shibata and Tanuma (2001) was later confirmed by numerical simulations by Bárta et al. (2011b), which have shown formation of plasmoids on multiple spatial scales – see Fig. 2.7. The key idea of this scenario is based on the cascade of tearing modes working at consecutively smaller-scale parts of current sheets which interleave magnetic islands/plasmoids formed by the higher-level tearing – see Fig. 2.6. In this scenario magnetic reconnection proceeds through the cascade of subsequent tearing modes until the dissipation scale is reached where the anomalous resistivity is working. The cascade reconnection can also explain huge number of accelerated particles inferred from hard X-rays (HXR) observations (see Vlahos (2007)). The cascade reconnection is supported by the analytical theory of Loureiro et al. (2007). Their theory shows that high Lundquist number systems with high enough current sheet ratio of length to width are inherently unstable to formation of plasmoids on very small time scales. Samtaney et al. (2009), Bhattacharjee et al. (2009), and Huang and Bhattacharjee (2010) confirmed predictions of Loureiro analytical theory by numerical simulations with high Lundquist numbers. Moreover, Bárta et al. (2010) and Bárta et al. (2011b) studied a cascade reconnection by multi-scale simulations on five orders of magnitude, where the numerical simulation reveals forming perpendicular current sheet during secondary plasmoids merging where another plasmoid cascade can take place and even more increase reconnection rate. The multi-scale simulations support the idea of cascade of tearing instabilities and driven coalescence processes.

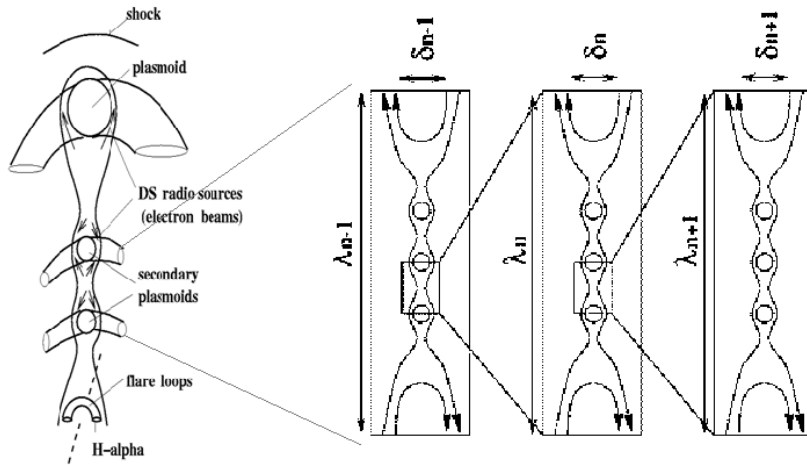


Figure 2.6: The concept of cascading/fractal reconnection Bárta et al. (2010) and its relation to the multi-plasmoid picture of current layer in the (eruptive) solar flare suggested by Karlický (2004) for explanation of multiple observed DPS radio bursts.

Cascading reconnection not only that solves the theoretical problem of the scale gap but it attracts also attention of solar physicists as it can reconcile the two distinct aspects of solar

flares described in the previous chapter. Cascading reconnection is inherently connected with many small-scale short-living plasmoids interleaved by dissipative current sheets. Hence, the global flare current layer is populated by many embedded current sheets, diffusion regions and X-lines. This fact explains naturally observed signatures of fragmented energy release (Bárta et al., 2011a) and – because of much larger total volume of all diffusion regions – it has potential to account for the necessary flux of energetic particles. On the other hand, it retains all the properties of the standard CSHKP flare scenario on the large scales.

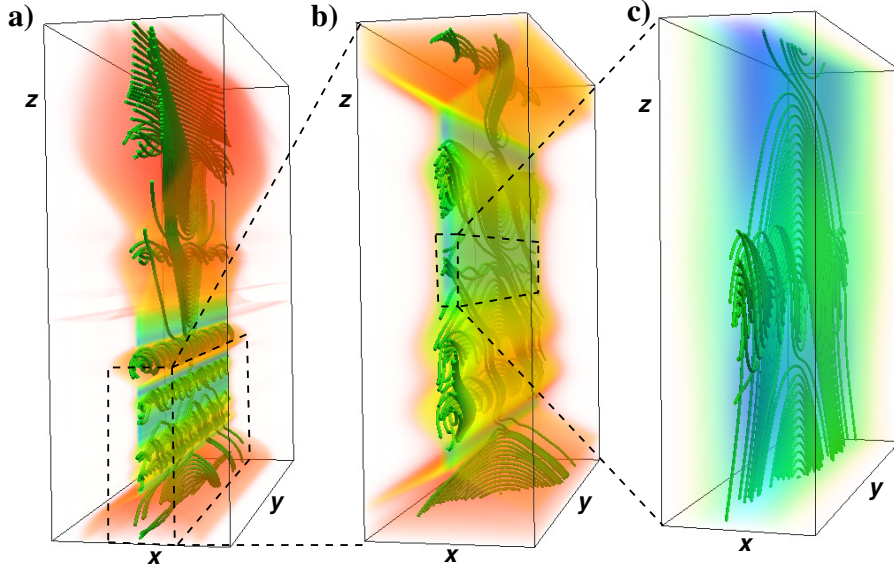


Figure 2.7: Numerical simulation of cascading reconnection by Bárta et al. (2011b). Formation of plasmoids at multiple scales in line with the idea of Shibata and Tanuma (2001) is clearly visible.

The cascading reconnection concept resembles strongly the transition to turbulence in the classical fluid dynamics (FD). The role of vortex tubes played in the FD in cascading of energy from large to dissipative scale is played by twisted magnetic flux-ropes – plasmoids, in the MHD process leading to the magnetic reconnection. This idea is very promising but also hard to handle via numerical simulations because of the intrinsically multi-scale nature of the process. An attempt has been made in Bárta et al. (2011b) to do so via hierarchically embedded MHD subsystems – a kind of the Adaptive Mesh Refinement (AMR) technique. In this work we are going to grasp it via more natural and promising approach – solving the set of MHD equations on the unstructured and dynamic mesh of finite elements. Before doing this, a brief overview of description of magnetized plasmas is presented from the very accurate and detailed one based on Liouville theorem and statistical physics up to the MHD. Simplifications that are done in each step under some assumptions will help to understand us which aspects of magnetic reconnection we are able to calculate correctly in the multiscale MHD model and what is the hidden physics on the subgrid scale in our approach.

Chapter 3

Description of magnetized plasmas

In the solar physics we deal with a matter in the form of an ionized gas – plasma. In general we can use two approaches for description of physical phenomena. The first is a particle approach where we study the microscopic and fast events – by the kinetic theory. The second approach is described by magnetohydrodynamic (MHD) equations – like as a fluid theory. It is a good approximation for large-scale and long-time plasma processes. The MHD model is a good approximation for astrophysical simulations where we deal with large scales (see Priest (1982), Aschwanden (2005)). The MHD can be derived from the kinetic theory by the terms of statistical quantities. In this chapter we derive MHD equations from the kinetic theory. The details of the derivation of MHD equations are presented, e.g., in Somov (2006), Goedbloed and Poedts (2004), Chen (1984) and Kracík and Tobiáš (1966).

3.1 Kinetic theory

The plasma is a state of matter in which particles interact mutually by an electromagnetic force on the long distances. Therefore, the plasma behavior is collective. The plasma consist of electrons, protons and ions mutually driven by the electromagnetic force (in the case of partially ionization, plasma generally contains also neutral particles which contribute to collisions). In the classical physics the system of N particles can be represented by a point in the $6N$ -dimensional phase space with coordinates $[\mathbf{x}_1, \mathbf{p}_1, \mathbf{x}_2, \mathbf{p}_2, \dots, \mathbf{x}_N, \mathbf{p}_N]$ where $\mathbf{x}_i = (x_i, y_i, z_i)$ and $\mathbf{p}_i = m_i \mathbf{v}_i = (p_x^i, p_y^i, p_z^i)$ are the radius vectors, momenta of single particles and v_i , m_i are velocities and masses of particles. In order to manage a huge number of particles we use a statistical physics. We can define an ensemble averaged probability density for finding a randomly chosen system from the ensemble of time t in the phase point $\mathbf{z}_i = (\mathbf{x}_i, \mathbf{p}_i)$

$$f_N(\mathbf{z}_i, t) \equiv f_N(\mathbf{z}_1, \mathbf{z}_2, \mathbf{z}_3, \dots, \mathbf{z}_N, t). \quad (3.1)$$

This function of $6N$ phase space coordinates and time is called the phase density or the N -particle distribution function. In addition to this function we can define the s -particle distribution function as an integral over part of phase space variables

$$f_s(\mathbf{z}_i, t) = \int f_N(\mathbf{z}_i, t) d\mathbf{z}_{s+1} d\mathbf{z}_{s+2} \cdots d\mathbf{z}_N, \quad i = 1, \dots, s. \quad (3.2)$$

In the phase space the each point represent the state of some system. From this imply that the no state can rise or disappear. Flow of phase density accomplish continuity equation

$$\frac{\partial f_N}{\partial t} + \nabla \cdot f_N \mathbf{v} = 0, \quad (3.3)$$

where $\mathbf{v} = [\dot{\mathbf{x}}_1, \dot{\mathbf{p}}_1, \dot{\mathbf{x}}_2, \dot{\mathbf{p}}_2, \dots, \dot{\mathbf{x}}_N, \dot{\mathbf{p}}_N]$ is velocity of phase density flow and ∇ is generalized

divergent. The evolution of systems in phase space on their phase space trajectories is given Hamiltonian equations

$$\dot{x}_i = \frac{\partial \mathcal{H}}{\partial p_i}, \quad \dot{p}_i = -\frac{\partial \mathcal{H}}{\partial x_i}, \quad (3.4)$$

Substitution equations (3.4) to continuity equation (3.3) we get

$$\frac{\partial f_N}{\partial t} + \sum_{i=1}^{3N} \left[\frac{\partial \mathcal{H}}{\partial p_i} \frac{\partial f_N}{\partial x_i} - \frac{\partial \mathcal{H}}{\partial x_i} \frac{\partial f_N}{\partial p_i} \right] = 0. \quad (3.5)$$

Foregoing equations is the Liouville theorem.

We use the phase density for single particle $f_1(\mathbf{z}_i, t)$ in the Liouville theorem then we obtain an equation which describes a time evolution of system

$$\frac{\partial f}{\partial t} + \mathbf{v} \frac{\partial f}{\partial \mathbf{x}} + \frac{\mathbf{F}}{m} \frac{\partial f}{\partial \mathbf{v}} = \left(\frac{\partial f}{\partial t} \right)_c. \quad (3.6)$$

This single particle equation is called Boltzmann equation, where $\mathbf{F} = q(\mathbf{E} + \mathbf{v} \times \mathbf{B})$ is the Lorentz force with electric field \mathbf{E} , magnetic field \mathbf{B} and q, \mathbf{v} are electric charge and velocity of particle, respectively.

3.2 Two fluid description

Now we can proceed to averaging the Boltzmann equation over velocities. The zeroth moment of the Boltzmann equation is a simple integration

$$\int \frac{\partial f}{\partial t} d\mathbf{v} + \int \mathbf{v} \frac{\partial f}{\partial \mathbf{x}} d\mathbf{v} + \frac{q}{m} \int (\mathbf{E} + \mathbf{v} \times \mathbf{B}) \frac{\partial f}{\partial \mathbf{v}} d\mathbf{v} = \int \left(\frac{\partial f}{\partial t} \right)_c d\mathbf{v}. \quad (3.7)$$

From the first term we get

$$\int \frac{\partial f}{\partial t} d\mathbf{v} = \frac{\partial}{\partial t} \int f d\mathbf{v} = \frac{\partial n}{\partial t}, \quad (3.8)$$

where n is the plasma density. In the second term the \mathbf{v} is an independent variable with regard to the operator $\frac{\partial}{\partial \mathbf{x}}$

$$\int \mathbf{v} \frac{\partial f}{\partial \mathbf{x}} d\mathbf{v} = \frac{\partial}{\partial \mathbf{x}} \int \mathbf{v} f d\mathbf{v} = \nabla \cdot (n \bar{\mathbf{v}}) \equiv \nabla \cdot (n \mathbf{u}), \quad (3.9)$$

where $\mathbf{u} = \bar{\mathbf{v}}$ is the mean velocity of plasma. The electric field \mathbf{E} term is zero

$$\int \mathbf{E} \cdot \frac{\partial f}{\partial \mathbf{v}} d\mathbf{v} = \int \frac{\partial}{\partial \mathbf{v}} \cdot (f \mathbf{E}) d\mathbf{v} = \int_{S_\infty} f \mathbf{E} \cdot d\mathbf{S} = 0. \quad (3.10)$$

The integral is converted to a surface integral using Gauss's theorem. The necessary condition for any distribution with finite energy is $f \rightarrow 0$ vanishes faster than v^{-2} as $v \rightarrow \infty$. The term $\mathbf{v} \times \mathbf{B}$ can be written as follows

$$\int \mathbf{v} \times \mathbf{B} \frac{\partial f}{\partial \mathbf{v}} d\mathbf{v} = \int \frac{\partial}{\partial \mathbf{v}} \cdot (f \mathbf{v} \times \mathbf{B}) d\mathbf{v} - \int f \frac{\partial}{\partial \mathbf{v}} \times (\mathbf{v} \times \mathbf{B}) d\mathbf{v}. \quad (3.11)$$

Two integrals are obtained by the product rule. The first integral can be again transformed to a surface integral. The phase density f exponentially falls (for the Maxwellian distribution or any distribution function which sufficiently rapidly falls) as $v \rightarrow \infty$ that is faster than any power of v and therefore the integral vanishes. The second integral vanishes because term $\mathbf{v} \times \mathbf{B}$ is perpendicular to $\partial/\partial \mathbf{v}$. The right hand side term in equation 3.7 is zero because

collisions cannot change the total number of particles (recombination and nuclear reactions are not considered here). Finally, we can write the continuity equation

$$\frac{\partial n}{\partial t} + \nabla \cdot (n\mathbf{u}) = 0. \quad (3.12)$$

The next moment of Boltzmann equation we get when we multiply the equation (3.7) by a term $m\mathbf{v}$ and integrate over $d\mathbf{v}$

$$m \int \mathbf{v} \frac{\partial f}{\partial t} d\mathbf{v} + m \int \mathbf{v} \left(\mathbf{v} \cdot \frac{\partial f}{\partial \mathbf{x}} \right) d\mathbf{v} + q \int \mathbf{v} (\mathbf{E} + \mathbf{v} \times \mathbf{B}) \frac{\partial f}{\partial \mathbf{v}} d\mathbf{v} = m \int \mathbf{v} \left(\frac{\partial f}{\partial t} \right)_c d\mathbf{v}. \quad (3.13)$$

The first term gives

$$m \int \mathbf{v} \frac{\partial f}{\partial t} d\mathbf{v} = m \frac{\partial}{\partial t} \int \mathbf{v} f d\mathbf{v} = m \frac{\partial}{\partial t} (n\mathbf{u}). \quad (3.14)$$

The second integral can be written

$$m \int \mathbf{v} \left(\mathbf{v} \cdot \frac{\partial f}{\partial \mathbf{x}} \right) d\mathbf{v} = \int \frac{\partial}{\partial \mathbf{x}} \cdot (f \mathbf{v} \mathbf{v}) d\mathbf{v} = \frac{\partial}{\partial \mathbf{x}} \cdot \int (f \mathbf{v} \mathbf{v}) d\mathbf{v}. \quad (3.15)$$

Again, like in the continuity equation we use the fact that \mathbf{v} is not related to the operator $\frac{\partial}{\partial \mathbf{x}}$. Since the average quantity is calculated $1/n$ times its weighted integral over \mathbf{v} , we have average value of $\mathbf{v}\mathbf{v}$ times n

$$\frac{\partial}{\partial \mathbf{x}} \cdot \int f \mathbf{v} \mathbf{v} d\mathbf{v} = \nabla \cdot n \bar{\mathbf{v}} \bar{\mathbf{v}}. \quad (3.16)$$

The particle velocity \mathbf{v} can be separated into the average (fluid) velocity \mathbf{u} and the thermal velocity \mathbf{w}

$$\mathbf{v} = \mathbf{u} + \mathbf{w} \quad (3.17)$$

then we can write

$$\nabla \cdot n \bar{\mathbf{v}} \bar{\mathbf{v}} = \nabla \cdot (n \mathbf{u} \mathbf{u}) + \nabla \cdot (n \bar{\mathbf{w}} \bar{\mathbf{w}}) + 2 \nabla \cdot (n \mathbf{u} \bar{\mathbf{w}}). \quad (3.18)$$

The average of thermal velocity is obviously zero. The first term can be written as follows

$$\nabla \cdot (n \mathbf{u} \mathbf{u}) = \mathbf{u} \nabla \cdot (n \mathbf{u}) + n (\mathbf{u} \cdot \nabla) \mathbf{u}. \quad (3.19)$$

The second term in equation (3.18) multiplied by particle mass m is definition of the stress tensor \mathbf{P} :

$$\mathbf{P} \equiv mn \bar{\mathbf{w}} \bar{\mathbf{w}} \quad (3.20)$$

The third term in equation (3.13) of first moment of Boltzmann equation is

$$\begin{aligned} q \int \mathbf{v} (\mathbf{E} + \mathbf{v} \times \mathbf{B}) \frac{\partial f}{\partial \mathbf{v}} d\mathbf{v} &= q \int \frac{\partial}{\partial \mathbf{v}} \cdot [f \mathbf{v} (\mathbf{E} + \mathbf{v} \times \mathbf{B})] d\mathbf{v} - \\ &- q \int f \mathbf{v} \frac{\partial}{\partial \mathbf{v}} \cdot (\mathbf{E} + \mathbf{v} \times \mathbf{B}) d\mathbf{v} - q \int f (\mathbf{E} + \mathbf{v} \times \mathbf{B}) \cdot \frac{\partial \mathbf{v}}{\partial \mathbf{v}} d\mathbf{v}. \end{aligned} \quad (3.21)$$

The first two integrals on the right hand side vanish for the same reason like integral in the continuity equation. The term $\partial \mathbf{v} / \partial \mathbf{v}$ is identity tensor. Therefore we obtain

$$-q \int f (\mathbf{E} + \mathbf{v} \times \mathbf{B}) \cdot \frac{\partial \mathbf{v}}{\partial \mathbf{v}} d\mathbf{v} = -q \int f (\mathbf{E} + \mathbf{v} \times \mathbf{B}) d\mathbf{v} = -qn (\mathbf{E} + \mathbf{u} \times \mathbf{B}). \quad (3.22)$$

The last part of first moment is collision integral. Than we will continue, we make several general suggestions. The total number of particles of species i at a certain position is not

changed by the collisions with particles of species j .

$$\int \left(\frac{\partial f}{\partial t} \right)_{ij} d\mathbf{v} = 0 . \quad (3.23)$$

The momentum and energy are conserved for collisions between particles of same species

$$m_i \int \mathbf{v} \left(\frac{\partial f}{\partial t} \right)_{ii} d\mathbf{v} = 0 \quad (3.24)$$

$$\frac{1}{2} m_i \int v^2 \left(\frac{\partial f}{\partial t} \right)_{ii} d\mathbf{v} = 0 \quad (3.25)$$

and momentum and energy is also conserved for collisions between particles i and j

$$m_i \int \mathbf{v} \left(\frac{\partial f}{\partial t} \right)_{ij} d\mathbf{v} + m_j \int \mathbf{v} \left(\frac{\partial f}{\partial t} \right)_{ji} d\mathbf{v} = 0 \quad (3.26)$$

$$\frac{1}{2} m_i \int v^2 \left(\frac{\partial f}{\partial t} \right)_{ij} d\mathbf{v} + \frac{1}{2} m_j \int v^2 \left(\frac{\partial f}{\partial t} \right)_{ji} d\mathbf{v} = 0 . \quad (3.27)$$

Then the influence of microscopic collisions to the macroscopic fluid can be described by term \mathbf{P}_{ij} which represents momentum gain of fluid of particle species i caused by collisions with particles of species j and vice versa.

$$\mathbf{P}_{ij} \equiv m \int \mathbf{v} \left(\frac{\partial f}{\partial t} \right)_c d\mathbf{v} . \quad (3.28)$$

Collecting results from equations (3.14),(3.19),(3.20),(3.22) and (3.28), we get

$$mn \frac{\partial}{\partial t} (n\mathbf{u}) + m\mathbf{u}\nabla \cdot (n\mathbf{u}) + mn(\mathbf{u}\nabla)\mathbf{u} = qn(\mathbf{E} + \mathbf{u} \times \mathbf{B}) - \nabla P + \mathbf{P}_{ij} , \quad (3.29)$$

With substitution of continuity equation (3.12) into second term we can finally gain the second moment of Boltzmann equation - the momentum equation:

$$mn \left[\frac{\partial \mathbf{u}}{\partial t} + (\mathbf{u} \cdot \nabla) \mathbf{u} \right] = qn(\mathbf{E} + \mathbf{u} \times \mathbf{B}) - \nabla P + \mathbf{P}_{ij} , \quad (3.30)$$

In general, in order to find the energy equation, we should multiply Boltzmann equation by a factor $m\mathbf{v}_i\mathbf{v}_j$ and integrate over \mathbf{v} . The resulting system contains matrix equation in partial derivatives. For our aims, a more simple derivation is sufficient. We multiply the kinetic equation (3.7) by a term $\frac{1}{2}m\mathbf{v}^2$ and integrate over velocity space \mathbf{v} then we obtain scalar equation for energy conservation

$$\frac{m}{2} \int v^2 \frac{\partial f}{\partial t} d\mathbf{v} + \frac{m}{2} \int v^2 \left(\mathbf{v} \frac{\partial f}{\partial \mathbf{x}} \right) d\mathbf{v} + \frac{q}{2} \int v^2 (\mathbf{E} + \mathbf{v} \times \mathbf{B}) \frac{\partial f}{\partial \mathbf{v}} d\mathbf{v} = \frac{m}{2} \int v^2 \left(\frac{\partial f}{\partial t} \right)_c d\mathbf{v} . \quad (3.31)$$

The first term contains a temporal change of the mean kinetic energy ε_k . The second term represents the internal kinetic energy flux or the divergence of heat flux density $F_C = \frac{1}{2}mn \langle v_j^2 v_i \rangle$. The third term is the work done by the force $(\mathbf{E} + \mathbf{v} \times \mathbf{B})$, which can include an acceleration by an electric field \mathbf{E} . Work by the magnetic part (Lorenz force) is, of course, zero. Let us derive it in detail. The first temporal term can be written as

$$\frac{m}{2} \int v^2 \frac{\partial f}{\partial t} d\mathbf{v} = \frac{m}{2} \frac{\partial}{\partial t} \int v^2 f d\mathbf{v} = \frac{m}{2} \frac{\partial}{\partial t} n \overline{v^2 \mathbf{v}} . \quad (3.32)$$

We separate velocity \mathbf{v} into average and thermal velocity (see Eq. (3.17)) then v^2 is

$$v^2 = u^2 + w^2 + 2uw , \quad (3.33)$$

with using these relations we gain

$$\frac{m}{2} \frac{\partial}{\partial t} n \overline{v^2} \mathbf{v} = \frac{m}{2} \frac{\partial}{\partial t} n \left(u^2 + \overline{w^2} + 2u\overline{w} \right) . \quad (3.34)$$

The term u^2 corresponds to the macroscopic fluid kinetic energy, the second term $\overline{w^2}$ represents mean kinetic energy of chaotic motion per single particle ε . The last term is zero. Using all these relations we have

$$\frac{\partial}{\partial t} \left(\frac{\rho u^2}{2} + \rho \varepsilon \right) , \quad (3.35)$$

where $\rho = mn$ is mass density. Next integral in equation (3.31) is

$$\frac{m}{2} \int v^2 \left(\mathbf{v} \frac{\partial f}{\partial \mathbf{x}} \right) d\mathbf{v} = \frac{m}{2} \frac{\partial}{\partial \mathbf{x}} \int f v^2 \mathbf{v} d\mathbf{v} = \frac{m}{2} \nabla \cdot n \overline{v^2} \mathbf{v} . \quad (3.36)$$

Again, we separate velocities and obtain

$$\frac{m}{2} \nabla \cdot n \overline{v^2} \mathbf{v} = \frac{m}{2} \nabla \cdot n \left(u^2 \mathbf{u} + \mathbf{u} \overline{w^2} + 2\mathbf{u} \overline{w} + u^2 \overline{w} + \overline{w^2} \mathbf{w} + 2\mathbf{u} \overline{w} \mathbf{w} \right) . \quad (3.37)$$

The third and fourth terms are obviously zero. The first term represents flow of macroscopic kinetic energy, second is flow of thermal energy, the quality $w^2 w$ corresponds to the heat flux density g and last term is work done by pressure $\mathbf{u} \cdot \mathbf{P}$. Then we have

$$\nabla \cdot \left[\rho \mathbf{u} \left(\frac{v^2}{2} + \varepsilon \right) + \mathbf{u} \cdot \mathbf{P} + g \right] . \quad (3.38)$$

The force integral in the second momentum equation (3.31) can be solved similar to the momentum equation

$$\begin{aligned} \frac{q}{2} \int v^2 (\mathbf{E} + \mathbf{v} \times \mathbf{B}) \frac{\partial f}{\partial \mathbf{v}} d\mathbf{v} &= \frac{q}{2} \int \frac{\partial}{\partial \mathbf{v}} \cdot [f v^2 (\mathbf{E} + \mathbf{v} \times \mathbf{B})] d\mathbf{v} - \\ &- \frac{q}{2} \int f v^2 \frac{\partial}{\partial \mathbf{v}} \cdot (\mathbf{E} + \mathbf{v} \times \mathbf{B}) d\mathbf{v} - \frac{q}{2} \int f (\mathbf{E} + \mathbf{v} \times \mathbf{B}) \cdot \frac{\partial v^2}{\partial \mathbf{v}} d\mathbf{v} . \end{aligned} \quad (3.39)$$

The first two integral on the the right hand side vanish for the same reason as before and term $\partial v^2 / \partial \mathbf{v} = 2\mathbf{v}$. If we take in account that the magnetic part of Lorenz force cannot do work then we have

$$qn\mathbf{u} \cdot \mathbf{E} \quad (3.40)$$

Finally the last term, the right-hand term of the energy equation describes the energy changes due to collisions between particle of different species.

$$\frac{m}{2} \int v^2 \left(\frac{\partial f}{\partial t} \right)_c d\mathbf{v} = \frac{m}{2} u^2 \int \left(\frac{\partial f}{\partial t} \right)_c d\mathbf{v} + \frac{m}{2} \int w^2 \left(\frac{\partial f}{\partial t} \right)_c d\mathbf{v} + m\mathbf{u} \cdot \int \left(w \frac{\partial f}{\partial t} \right)_c d\mathbf{v} , \quad (3.41)$$

where the equation 3.33 is used. The first integral corresponds to change energy due to change of the total number of particles. If we consider system without ionization, recombination or other processes which can change number of particles then this term is zero. The second term is the rate of thermal energy release Q_{ij} in the gas due to collisions with other particles. The last term is the work done by the collisional force of friction \mathbf{F}_{ij} of particles with other particles.

Collecting results from equations (3.35),(3.38),(3.40) and collisional terms, we can, finally, write fluid energy equation

$$\frac{\partial}{\partial t} \left(\frac{\rho u^2}{2} + \rho \varepsilon \right) + \nabla \cdot \left[\rho \mathbf{u} \left(\frac{u^2}{2} + \varepsilon \right) + \mathbf{u} \cdot \mathbf{P} + g \right] - q n \mathbf{u} \cdot \mathbf{E} = \mathbf{Q}_{ij} + \mathbf{F}_{ij} . \quad (3.42)$$

The energy can generally contain contributions of gravitational force F_g , emission of radiation E_R , or the energy sources E_H .

The complete HMD equations contain also induction equation. Its derivation is straightforward. We have Faraday's law

$$\frac{\partial \mathbf{B}}{\partial t} = -\nabla \times \mathbf{E} , \quad (3.43)$$

where electric field can be substituted by general Ohm's laws

$$\mathbf{E} = -\mathbf{u} \times \mathbf{B} + \frac{\eta}{\mu_0} \mathbf{J} , \quad (3.44)$$

where $\mathbf{J} = \nabla \times \mathbf{B}$ is current density, η is electric resistivity and μ_0 is permeability of vacuum. The induction equation is

$$\frac{\partial \mathbf{B}}{\partial t} + \nabla \times (\mathbf{B} \times \mathbf{u}) = -\frac{1}{\mu_0} \nabla \times (\eta \nabla \times \mathbf{B}) . \quad (3.45)$$

To derive conservation law for (electro-)magnetic energy let us start with Faraday's law multiplied by \mathbf{B}/μ_0

$$\frac{\mathbf{B}}{\mu_0} \cdot \frac{\partial \mathbf{B}}{\partial t} = -\frac{\mathbf{B}}{\mu_0} \cdot \nabla \times \mathbf{E} . \quad (3.46)$$

Left hand side is obviously the time derivate of magnetic energy per unit volume

$$\frac{\partial U_m}{\partial t} = \frac{\partial}{\partial t} \frac{B^2}{2\mu_0} = \frac{\mathbf{B}}{\mu_0} \frac{\partial \mathbf{B}}{\partial t} . \quad (3.47)$$

The right hand side can be manipulated as follows

$$-\frac{\mathbf{B}}{\mu_0} \cdot \nabla \times \mathbf{E} = \frac{1}{\mu_0} \nabla \cdot (\mathbf{B} \times \mathbf{E}) - \frac{1}{\mu_0} \mathbf{E} \cdot \nabla \times \mathbf{B} . \quad (3.48)$$

Using definition of current density $\nabla \times \mathbf{B} = \mu_0 \mathbf{j}$ we have

$$\frac{\partial}{\partial t} \frac{B^2}{2\mu_0} = \frac{1}{\mu_0} \nabla \cdot (\mathbf{B} \times \mathbf{E}) - \mathbf{E} \cdot \mathbf{j} . \quad (3.49)$$

Adding foregoing equation into equation (3.42) we have total energy equation

$$\frac{\partial}{\partial t} \left(\frac{\rho u^2}{2} + \rho \varepsilon + \frac{B^2}{2\mu_0} \right) + \nabla \cdot \left[\rho \mathbf{u} \left(\frac{u^2}{2} + \varepsilon \right) + \mathbf{u} \cdot \mathbf{P} - \frac{1}{\mu_0} \mathbf{B} \times \mathbf{E} + g \right] = \mathbf{Q}_{ij} + \mathbf{F}_{ij} , \quad (3.50)$$

where we used the definition of current density $q n \mathbf{u} \cdot \mathbf{E} \equiv \mathbf{E} \cdot \mathbf{J}$ and the electric term vanished. Finally, we can write all two (multi) fluid MHD equations

$$\frac{\partial \rho_i}{\partial t} + \nabla \cdot (\rho_i \mathbf{u}_i) = 0 , \quad (3.51)$$

$$\rho_i \left[\frac{\partial \mathbf{u}_i}{\partial t} + (\mathbf{u}_i \cdot \nabla) \mathbf{u}_i \right] = q_i n_i (\mathbf{E} + \mathbf{u}_i \times \mathbf{B}) - \nabla P_i + P_{ij} , \quad (3.52)$$

$$\frac{\partial}{\partial t} \left(\frac{\rho_i u_i^2}{2} + \rho_i \varepsilon_i + \frac{B^2}{2\mu_0} \right) + \nabla \cdot \left[\rho \mathbf{u}_i \left(\frac{u_i^2}{2} + \varepsilon_i \right) + \mathbf{u}_i \cdot \mathbf{P}_i - \frac{1}{\mu_0} \mathbf{B} \times \mathbf{E} + g_i \right] = \mathbf{Q}_{ij} + \mathbf{F}_{ij}, \quad (3.53)$$

$$\frac{\partial \mathbf{B}}{\partial t} + \nabla \times (\mathbf{B} \times \mathbf{u}_i) = -\frac{1}{\mu_0} \nabla \times (\eta \nabla \times \mathbf{B}), \quad (3.54)$$

where the indexes i and j denote a kind of fluid. The fluids interact mutually through the transport coefficients \mathbf{P}_{ij} , \mathbf{Q}_{ij} and \mathbf{F}_{ij} due to collisions between particles of different species.

3.3 MHD

From moments of Boltzmann equation we got a two-fluid (ions and electron fluids) continuity equation, motion equation and energy equation. For simplification, we do not consider emission of radiative losses or the energy sources and the energy dissipation due to particle collisions. The coronal plasma has a temperature about $\sim 1 MK$ and low density $\sim 10^{15} \text{ m}^{-3}$ due to the collisions are very rare. The equations for ion and electron components can be summed and we obtain an one-fluid resistivity MHD equations. The one fluid variables are defined as follows

$$\rho = n_e m_e + n_i m_i, \quad (3.55)$$

$$\rho \mathbf{u} = n_e m_e \mathbf{u}_e + n_i m_i \mathbf{u}_i, \quad (3.56)$$

$$\mathbf{j} = e n_e \mathbf{u}_e + e n_i \mathbf{u}_i, \quad (3.57)$$

$$p = p_e + p_i = (n_e + n_i) k_B T. \quad (3.58)$$

With one fluid variables we can write MHD equations

$$\frac{\partial \rho}{\partial t} + \nabla \cdot (\rho \mathbf{u}) = 0, \quad (3.59)$$

$$\rho \left(\frac{\partial \mathbf{u}}{\partial t} + \mathbf{u} \cdot \nabla \mathbf{u} \right) = \mathbf{j} \times \mathbf{B} - \nabla p + \rho \mathbf{g}, \quad (3.60)$$

$$\mathbf{E} + \mathbf{u} \times \mathbf{B} = \eta \mathbf{j}, \quad (3.61)$$

$$\frac{\partial}{\partial t} \left(\frac{\rho u^2}{2} + \rho \varepsilon + \frac{B^2}{2\mu_0} \right) = -\nabla \cdot \left[\rho \mathbf{u} \left(\frac{u^2}{2} + \varepsilon \right) + \mathbf{u} \cdot \mathbf{P} - \frac{1}{\mu_0} \mathbf{B} \times \mathbf{E} \right] + \rho \mathbf{g} \cdot \mathbf{u}, \quad (3.62)$$

where ρ is the mass density, \mathbf{u} is the macroscopic plasma velocity, \mathbf{E} and \mathbf{B} are electric and magnetic field respectively. We neglected the electric field term $e n \mathbf{E}$ in the momentum equation. The magnitude of electric field is smaller than the magnetic field by the factor $\sim u^2/c^2$. This system equations needs to be supplied by the state equation for plasma pressure $p = p(\rho, T)$ (where T is a plasma temperature), the Faraday's law

$$\frac{\partial \mathbf{B}}{\partial t} = -\nabla \times \mathbf{E}, \quad (3.63)$$

and the Ampere's law in a non-relativistic approximation

$$\nabla \times \mathbf{B} = \mu_0 \mathbf{j}, \quad (3.64)$$

which binds the current density with the magnetic field and can be considered as a definition of the current density \mathbf{j} from the computational point of view. The constant $\mu_0 = 4 \cdot 10^{-7} \pi$ is the magnetic permeability. The electric field \mathbf{E} is given by Ohm's law

$$\mathbf{E} = -\mathbf{u} \times \mathbf{B} + \eta \mathbf{j}. \quad (3.65)$$

In the computational physics equations is suitable to have in the conservative form (in the following equation set, the current density is denoted by capital \mathbf{J} because minuscule j is used as a index).

$$\begin{aligned} \frac{\partial \rho}{\partial t} + \frac{\partial \rho u_j}{\partial x_j} &= 0, \\ \frac{\partial(\rho u_i)}{\partial t} + \frac{\partial}{\partial x_j} \left[\rho u_i u_j - \frac{B_i B_j}{\mu_0} + \delta_{ij} \left(p + \frac{\mathbf{B}^2}{2\mu_0} \right) \right] &= \rho g_i, \\ \frac{\partial B_i}{\partial t} + \frac{\partial}{\partial x_j} (u_j B_i - u_i B_j) &= -\frac{\partial}{\partial x_j} (\varepsilon_{ijk} \eta J_k), \\ \frac{\partial U}{\partial t} + \frac{\partial}{\partial x_j} S_j &= \rho g_j u_j. \end{aligned} \quad (3.66)$$

The energy flux \mathbf{S} , and the plasma pressure p for the ideal gas are given by the following relations:

$$U = \frac{p}{\gamma - 1} + \frac{1}{2} \rho u^2 + \frac{\mathbf{B}^2}{2\mu_0} \quad (3.67)$$

$$\mathbf{S} = \left(U + p + \frac{\mathbf{B}^2}{2\mu_0} \right) \mathbf{u} - \frac{(\mathbf{u} \cdot \mathbf{B})}{\mu_0} \mathbf{B} + \frac{\eta}{\mu_0} \mathbf{j} \times \mathbf{B}. \quad (3.68)$$

In the (almost) collision-less plasma, we are mostly interested in, the classical resistivity plays usually a small role. Instead of that, various microscopical (kinetic) effects influence the plasma dynamics via other terms in the generalized Ohms law (see Büchner and Elkina (2006)). In order to mimic these processes, whose modeling is beyond the scope of the MHD approach, we re-consider the parameter η as a generalized resistivity, including the effects like wave-particle interactions or off-diagonal components in the electron pressure tensor into it. As such effects are – in general – observed in the highly filamented, intense current sheets we model the anomalous generalized resistivity as follows

$$\eta(\mathbf{r}, t) = \begin{cases} 0 & : |v_D| \leq v_{cr} \\ C \frac{(|v_D(\mathbf{r}, t)| - v_{cr})}{v_0} & : |v_D| > v_{cr} \end{cases}. \quad (3.69)$$

Thus, the non-ideal effects are turned on whenever the current-carrier drift velocity

$$v_D(\mathbf{r}, t) = \frac{|\mathbf{j}(\mathbf{r}, t)|}{e n_e}, \quad (3.70)$$

exceeds the critical threshold v_{cr} , which corresponds to the thickness of current sheet.

In order to solve the Eqs. (3.66) numerically, it is convenient to rescale all the quantities to the dimensionless units. Thus, all the spatial coordinates are expressed in the characteristic size L_0 and times in Alfvén transit time $\tau_A = L_0/v_A$, where $v_A = B_0/\sqrt{\rho_0}$ is a typical Alfvén speed. Magnetic field strength \mathbf{B} and plasma density ρ are given in the units of their characteristic values B_0 and ρ_0 and similar scaling holds for the other quantities – see Kliem et al. (2000) or Bárta et al. (2011b) for details. The normalization of MHD quantities is summarized in the table 3.1.

In order to utilize more universal LSFEM implementation for the more general form of equations (see Lukin (2008)) the set of MHD Eqs. (3.66) is rewritten into the conservative (flux/source) formulation (for the expanded form see Appendix 7.2)

$$\frac{\partial \Psi}{\partial t} + \frac{\partial \mathbf{F}_i(\Psi, \frac{\partial \Psi}{\partial x_j})}{\partial x_i} = \mathbf{S}(x_j, \Psi, t). \quad (3.71)$$

Variable	Normalization	Description
L	L_0	length
ρ	ρ_0	plasma density
\mathbf{B}	B_0	magnetic field
\mathbf{u}	$v_A = \frac{B_0}{\sqrt{\mu_0 \rho_0}}$	plasma velocity
t	$\tau_A = \frac{L_0}{v_A}$	time
p	$\frac{B_0^2}{2\mu_0}$	plasma pressure
\mathbf{E}	$v_A B_0$	electric field
\mathbf{j}	$\frac{B_0}{\mu_0 L_0}$	current density
η	$\mu_0 L_0 v_A$	electric resistivity
U	$\frac{1}{2} \rho_0 v_A^2$	energy
T	$\frac{p_0}{k_B n_0}$	temperature

Table 3.1: Normalization of MHD equations.

Here the local state vector $\Psi = (\rho, \pi, \mathbf{B}, U)$, the momentum density $\pi = \rho \mathbf{u}$, the flux \mathbf{F} and the source-term \mathbf{S} are defined as

$$\mathbf{F} = \begin{pmatrix} \pi \\ \rho \mathbf{u} \mathbf{u} - \mathbf{B} \mathbf{B} + \hat{\mathbf{I}}_{3 \times 3} (p + B^2) \\ \hat{\epsilon}_{3 \times 3} \cdot \mathbf{E} \\ (h + E_k) \mathbf{u} + 2 \mathbf{E} \times \mathbf{B} \end{pmatrix}, \quad \mathbf{S} = \begin{pmatrix} 0 \\ \rho \mathbf{g} \\ \mathbf{0} \\ \pi \cdot \mathbf{g} \end{pmatrix}, \quad (3.72)$$

where $\hat{\mathbf{I}}_{3 \times 3}$ is the 3×3 unit matrix, $\hat{\epsilon}_{3 \times 3}$ is the permutation pseudo-tensor, $\mathbf{E} = -\mathbf{u} \times \mathbf{B} + \eta \mathbf{j}$ is the electric field strength, and the enthalpy and kinetic energy densities are $h = \gamma p / (\gamma - 1)$ and $E_k = \rho v^2$, respectively.

Chapter 4

Least Squares Finite Element Method

The two past decades showed, that the finite element method (FEM) is one of the most general techniques for the numerical solution of differential equations. It has widely been used in broad fields of engineering and applied science. The solution of partial differential equations using the FEM is based on variational principle. The solution appears in the integral form over the computation domain Ω . The integral over entire domain can be separated into integrals over smaller sub-domains Ω_e – elements. The behavior of the solution on the elements is adequately described by polynomial functions. The most important features can be summarized as follows. The FEM can be applied onto arbitrary shape of the domain. The solution given by the FEM is expressed by series of basis functions – the solution is defined in each point in the whole domain. The FEM has rich and solid mathematical basis (see, i.g., Jiang (1998), Bochev and Gunzburger (2009)) due to we can mathematically analyze and estimate accuracy of the solution.

This chapter contains basic mathematical foundation of FEM methods, natural coordinates of elements and linearization and time discretization of partial differential equation. In the end of this chapter we introduce practical application of LSFEM and describe its behavior.

4.1 Motivation

One of the oldest numerical method for solving partial differential equations is the finite difference method (FDM). It is a fast method and its implementation is straightforward. The FDM is based on a sampling of continuous state variables on a discrete Cartesian mesh. The spatial derivatives are replaced by differences and the time is also discretized – the state is defined only at discrete time steps. The FDM has widely been used for simulations in the fluid dynamics and plasma physics in the last several decades. Its mathematical foundation is deeply investigated and also method limitations are found.

There are many ways how to make discretization of system of MHD Eq. (3.71) – the individual implementations are known as various numerical schemes. In our FDM MHD simulation we use a generalization of two-step explicit Lax-Wendroff scheme which in 1D takes form Chung (2002)

$$\begin{aligned}\Psi_i^{n+1} &= \frac{1}{2} (\Psi_{i+1}^n + \Psi_{i-1}^n) - \frac{\Delta t}{2\Delta x} (\mathbf{F}(\Psi_{i+1}^n) - \mathbf{F}(\Psi_{i-1}^n)) , \\ \Psi_i^{n+2} &= \Psi_i^n - \frac{\Delta t}{\Delta x} (\mathbf{F}(\Psi_{i+1}^{n+1}) - \mathbf{F}(\Psi_{i-1}^{n+1})) .\end{aligned}\quad (4.1)$$

The Cartesian mesh can involve only a limited range of scales due to the finite resolution. The traditional MHD simulations of current sheet dynamics Bárta et al. (2008), Kliem et al. (2000)

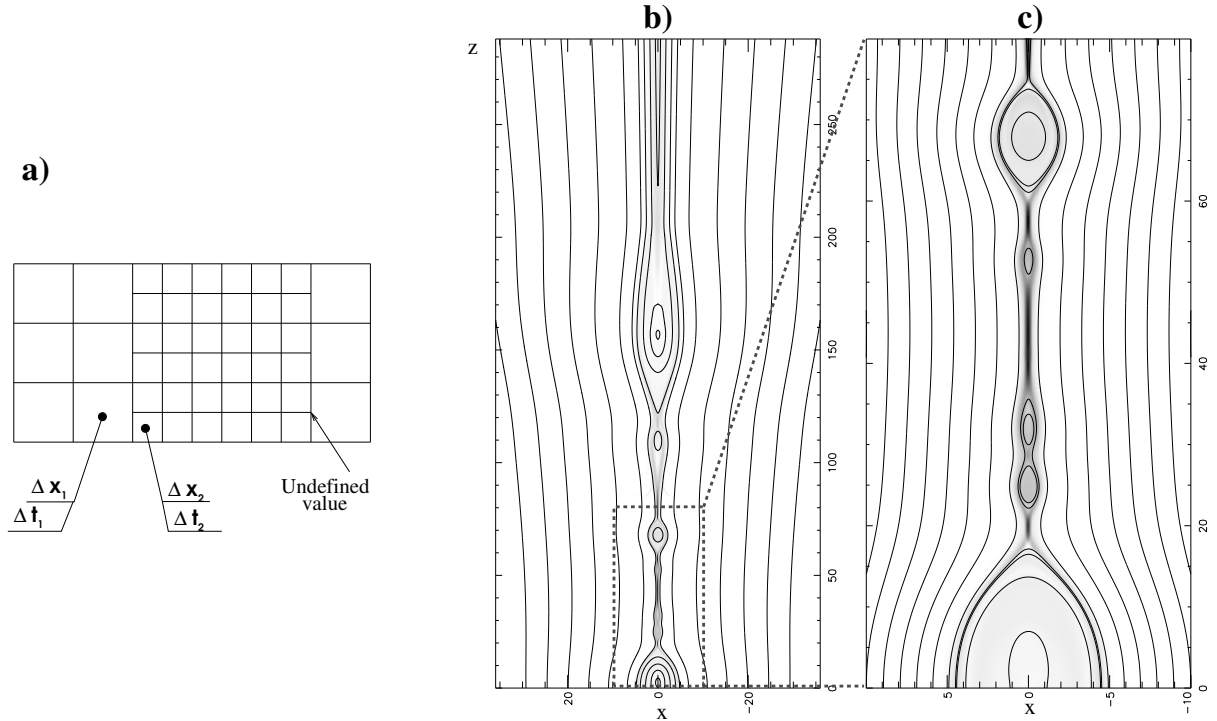


Figure 4.1: a) Adaptive mesh of Finite Difference Method. b) and c): The results of 2.5D FDM-AMR MHD code. The consecutively smaller magnetic islands/plasmoids are formed in the filamenting current sheet Bárta et al. (2010). Compare with the scenario of cascade reconnection in Fig. 2.6.

thus show only very-large-scale dynamics of studied system. Since we do not need a detailed sampling of areas with smooth dynamics, a local mesh refinement in the areas of high gradients might be sufficient for broadening the range of scales covered by the simulation. This simple idea (see Fig. 4.1) is behind the AMR technique.

The larger scale-range coverage is essential for study of multi-scale processes such as the cascading reconnection. Bárta therefore incorporated AMR into his existing 2.5D MHD FDM-based numerical model. Then he used the code for study of fragmentation of global flare current layer. For details on initial and boundary conditions see Bárta et al. (2010). The results of his modelling are shown in Figs. 4.1 b) and c) where the global and the detailed views of current density and magnetic field are displayed. Part b) shows the secondary plasmoid formation at coordinates $x = 0, z = 70$ and $x = 0, z = 110$ in the tearing current sheet between the main plasmoid and the flare loop arcade. Panel c) represents a zoomed view of rectangle denoted in b). Between the plasmoid located at coordinates $x = 0, z = 70$ and the flare loop-top even smaller plasmoids are formed in the further thinned current sheet.

The plasmoid formation at the smaller scale and the current sheet filamentation found in Bárta's simulation corresponds well to the scenario of cascade reconnection Shibata and Tanuma (2001) – cf. Fig. 2.6. As a new aspect Bárta's results also show the significance of plasmoid coalescence. Plasmoids interactions lead to formation of a perpendicular current sheet and a secondary reconnection in this sheet, which can be subjected to the same cascade as the global vertical flare current layer. We assume that this process continues down to the kinetic scales where the plasmoids kinetic coalescence could be the probable mechanism of the magnetic energy dissipation Drake et al. (2005).

The results represent undoubtedly advance in research of energy transport across the scales in magnetic reconnection in solar flares (and other large-scale systems). Nevertheless, a detailed analysis of AMR-FDM model shows also some drawbacks of this approach which prevent us

from continued scale-range extension towards higher resolution and may also have an impact on the credibility of results with super-refined meshes. The problems are related to the internal boundary between the meshes with different resolutions and they range from a small violation of magnetic-flux conservation to the artificial wave-reflections on the internal boundaries. To avoid this problems we focused our effort to the alternative FEM models, which are principally free of these difficulties since they does not use structured meshes. In the next section we are going to briefly describe the principles of FEM and first results of FEM MHD implementation.

4.2 Formulation of LSFEM

The FEM was originally proposed to numeric computations of deformations in the solid mechanics and it brings terminology of solid mechanics to the FEM. Formally we solve this kind of problem

$$\begin{aligned} \mathcal{A}\mathbf{u} &= \mathbf{f} \text{ on } \Omega \\ \mathcal{B}\mathbf{u} &= \mathbf{g} \text{ on } \Gamma \end{aligned} \tag{4.2}$$

where Ω is the considered domain, $\Gamma = \partial\Omega$ is a domain boundary of Ω , \mathcal{A} is a linear partial differential operator, \mathcal{B} is a boundary operator, \mathbf{f} is a source vector and \mathbf{g} is a border condition. In most cases we can transform a higher order equation to a first order system of equations. The operator \mathcal{A} is generally given in the form

$$\mathcal{A} = \mathcal{A}_0 + \sum_i \mathcal{A}_i \frac{\partial}{\partial x_i}, \tag{4.3}$$

where $\mathcal{A}_0, \mathcal{A}_i$ are constant matrices. We are looking for a solution of (4.2) using a variational method on the whole domain. We attempt to found the extreme of the functional of set (4.2). According to the underlining variational principle, the FEM can be classified into three major groups: Rayleigh-Ritz method, Galerkin method and the least-squares method. The Rayleigh-Ritz method is seeking minimum of the total potential energy. It is most widely used in the commercial finite element codes in engineering. The Galerkin method is based on the weighted residual form

$$\int_{\Omega} \mathbf{v}_i^T (\mathcal{A}\mathbf{u} - \mathbf{f}) d\Omega + \int_{\Gamma} \bar{\mathbf{v}}_i^T \mathcal{B}\mathbf{u} d\Gamma = 0, \tag{4.4}$$

where $\Gamma = \partial\Omega$ is a border of domain Ω , function $\mathbf{u} = \sum \Phi_j \mathbf{u}_j$ is approximated by a set of unknown parameters \mathbf{u}_j and *basis* (trial) functions $\Phi_j(\mathbf{x})$ where \mathbf{x} is an independent variable. The superscript T denotes the transposition and \mathbf{v}_i and $\bar{\mathbf{v}}_i$ are suitably chosen test functions. In the Galerkin method \mathbf{v}_i and $\bar{\mathbf{v}}_i$ are given by basis function

$$\mathbf{v}_i = \bar{\mathbf{v}}_i = \Phi_i. \tag{4.5}$$

The Galerkin method is more general than the Rayleigh-Ritz method because it can be used for solving equations with non-self-adjoint operator.

The Least Squares Finite Element Method (LSFEM) is strong and robust method for solving of first order partial differential equations. The method has several useful advantages, we present few of them in the following text. The LSFEM can solve all kind of equations parabolic, hyperbolic, elliptic and mixed. Moreover, the LSFEM for linear partial differential equations always leads to the symmetric positive definite matrices. The LSFEM theory is in a detail described by Jiang (1998) and Bochev and Gunzburger (2009).

The LSFEM is based on the minimization of residuals in the least-squares sense. The

method seeks the minimizer of the following functional

$$I(\mathbf{u}) = \int_{\Omega} (\mathcal{A}\mathbf{u} - \mathbf{f})^2 d\Omega. \quad (4.6)$$

The state variables are represented by unknown functions \mathbf{u} which are approximated by series of *basis functions* – usually low order polynomial. A necessary condition that \mathbf{u} be a minimizer of functional I in (4.6) is that its first variation vanish at \mathbf{u} – we seek the extreme of functional I

$$\lim_{t \rightarrow 0} \frac{\partial}{\partial t} I(\mathbf{u} + t\mathbf{v}) \equiv 2 \int_{\Omega} (\mathcal{A}\mathbf{v})^T (\mathcal{A}\mathbf{u} - \mathbf{f}) d\Omega = 0; \quad \forall \mathbf{v}. \quad (4.7)$$

At first we divide the computational domain into a union of finite elements and introduce a finite element basis. Let n denotes a number of nodes in one element and Φ_j is a basis function. We get an approximate function for an element e

$$\mathbf{u}^e = \sum_{j=1}^n \Phi_j u_j \quad (4.8)$$

We can substitute the function (4.8) into the equation (4.7) and separate the integrals corresponding to the node u_j

$$\int_{\Omega_e} \mathcal{A}^T \Phi_i \mathcal{A} \Phi_j d\Omega = \int_{\Omega_e} \mathcal{A}^T \Phi_i \mathbf{f} d\Omega, \quad (4.9)$$

where $\Omega_e \subset \Omega$ is the domain of e -th element in the global domain Ω . The equation (4.9) represents a sub-matrix \mathbf{S}_{ij} and a sub-vector \mathbf{R}_i . When we put all sub-matrices \mathbf{S}_{ij} together and all sub-vectors \mathbf{R}_i for one element we obtain the element matrix \mathbf{S}_e and element vector \mathbf{R}_e . The global matrix \mathbf{S} is assembled from the element matrices \mathbf{S}_e and the global vector \mathbf{R} is assembled from the element vectors \mathbf{R}_e . Finally we have the linear algebraic equations

$$\mathbf{S}\mathbf{U} = \mathbf{R}, \quad (4.10)$$

where \mathbf{S} is the sparse *stiffness matrix*, \mathbf{R} is the right hand side vector (in terminology of FEM so-called *load vector*) and \mathbf{U} is a discrete form of the state vector \mathbf{u} . The set of equations is solved by a numeric method which is suitable for solving set of equations with a sparse matrix – our code uses the conjugate gradient method (CGM). The advantages of FEM are an easy mesh refinement (h-adaptivity) and a possibility to increase the order of the basis functions (p-adaptivity) for more accurate description of a smooth solution on the element domain, see Fig. 4.2.

4.3 Boundary conditions

In the LSFEM we have several ways how to implement the boundary conditions. The first is a general way by using the Lagrange multipliers where we add additional boundary condition equations into the stiffness matrix. The additional equations enforce boundary conditions but this approach has inappropriate feature – the stiffness matrix with Lagrange multipliers is no more symmetric and positive definite.

The another (better) way to implement boundary conditions is using the shape functions which fulfill boundary conditions naturally on border elements. It leads to the correct LSFEM matrix. Unfortunately, it may be difficult to assemble such border shape function for all possible kind of boundary conditions.

The LSFEM can also involve boundary conditions into the functional $I_{tot}(\mathbf{u}) = I(\mathbf{u}) + I_{BC}(\mathbf{u})$ (see Bochev and Gunzburger (2009)) and evade all disadvantages of previous method.

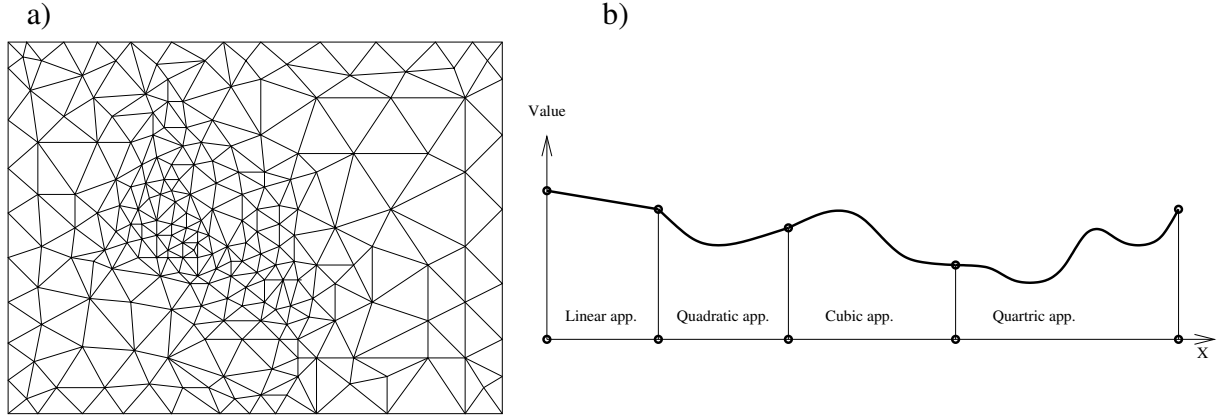


Figure 4.2: a) An example of h-adaptivity. The elements with higher gradients/error are divided into several smaller elements. b) An example of p-adaptivity, where a smooth solution with high gradient can be approximated by the various order of basis functions.

The boundary conditions functional I_{BC} in least-squares sense reads

$$I_{BC}(\mathbf{u}) = h^{-1} \int_{\Gamma} (\mathcal{B}\mathbf{u} - \mathbf{g})^2 d\Gamma, \quad (4.11)$$

where $\Gamma = \partial\Omega$ is a domain border Ω and h^{-1} is a mesh-dependent weight chosen to proper scaling between integral over Ω and its border Γ . We can use the same derivation as in the case of Eq. (4.6) then we obtain similar computational form

$$h^{-1} \int_{\Gamma_e} \mathcal{B}^T \Phi_i \mathcal{B} \Phi_j d\Gamma = h^{-1} \int_{\Gamma_e} \mathcal{B}^T \Phi_i \mathbf{g} d\Gamma. \quad (4.12)$$

These terms are added into the stiffness matrix and the load vector in the position corresponding to the nods i and j .

4.4 The LS solution of overdetermined systems

One of the advantages of the LSFEM is possibility to solve overdetermined system. This property is useful when we want to add additional restriction to our physical system. Let us consider a system of linear algebraic equations

$$\begin{pmatrix} k_{11} & k_{12} & \cdots & k_{1m} \\ k_{21} & k_{22} & \cdots & k_{2m} \\ \vdots & \vdots & \ddots & \vdots \\ k_{n1} & k_{n2} & \cdots & k_{nm} \end{pmatrix} \begin{pmatrix} u_1 \\ u_2 \\ \vdots \\ u_m \end{pmatrix} = \begin{pmatrix} f_1 \\ f_2 \\ \vdots \\ f_n \end{pmatrix}. \quad (4.13)$$

We can also write it in a form

$$\mathbf{K}\mathbf{u} = \mathbf{f}. \quad (4.14)$$

The system has n equations and m unknowns. It may have a unique solution, an infinite number of solutions or no solution at all. If the number of equations is less than the number of unknowns $n < m$, i.e., the system is under-determined. Such a system has an infinite number of solutions or no solution. If the number of equations is equal to the number of unknowns $n = m$, then the system has an unique solution (if $\det \mathbf{K} \neq 0$). In the case, where the number of equations is greater than the number of unknowns $n > m$ we have an overdetermined system. The overdetermined system has, generally, no solution.

Now we use a least-squares method to solve a system of linear algebraic equations (4.13). At first we formulate the solution of equations (4.13) in the least-squares sense, where we are summing squared residuals

$$\begin{aligned} I(\mathbf{u}) = & W_1 (k_{11}u_1 + k_{12}u_1 + \dots + k_{1m}u_m)^2 \\ & + W_2 (k_{21}u_1 + k_{22}u_1 + \dots + k_{2m}u_m)^2 \\ & + \dots \\ & + W_n (k_{n1}u_1 + k_{n2}u_1 + \dots + k_{nm}u_m)^2, \end{aligned} \quad (4.15)$$

where ($W_i > 0$, $i = 1, n$) are the weighting coefficients. Minimizing the functional (4.15) leads to a solution of normal equations

$$\mathbf{K}^T \mathbf{W} \mathbf{K} \mathbf{u} = \mathbf{K}^T \mathbf{W} \mathbf{f}, \quad (4.16)$$

where \mathbf{W} is an $n \times n$ diagonal matrix whose diagonal elements consist of W_i . If the number of equations is less than the number of unknowns $n < m$, i.e., the system is under-determined, then the system has an infinite number of solutions or no solution. In this case the matrix $\mathbf{K}^T \mathbf{W} \mathbf{K}$ is singular (i.e. $\det \mathbf{K}^T \mathbf{W} \mathbf{K} = 0$).

When $n = m$ the solution of least-squares approach (4.16) is identical to the solution of system (4.13). All residuals are equal to zero.

If the number of equations is greater than the number of unknowns $n > m$ and the system is overdetermined then the least-squares solution exist uniquely. For the overdetermined system we always can find a unique solution in the least-squares sense. We can also use various weighting matrices to get various unique solutions. The equation with a greater weighted coefficient has a smaller residuum. We choose higher weighting coefficient for a more 'important' equation where we require a smaller error, i.e., more sensitive to errors. In general, the residuals for the least-square method are not equal to zero. At the end of this section we present a simple example, let us consider a following system

$$\begin{pmatrix} 1 & 1 \\ 1 & 2 \\ 2 & 3 \end{pmatrix} \begin{pmatrix} u_1 \\ u_2 \end{pmatrix} = \begin{pmatrix} 3 \\ 5 \\ 8 \end{pmatrix}. \quad (4.17)$$

This system has three equations and only two unknowns. It is clearly visible that the system is overdetermined and has no solution. Now we choose a weighting matrix as ($W_i = 1$, $i = 1, 2, 3$), the least-squares equation is

$$\begin{pmatrix} 1 & 1 & 2 \\ 1 & 2 & 3 \end{pmatrix} \begin{pmatrix} 1 & 0 & 0 \\ 0 & 1 & 0 \\ 0 & 0 & 1 \end{pmatrix} \begin{pmatrix} 1 & 1 \\ 1 & 2 \\ 2 & 3 \end{pmatrix} \begin{pmatrix} u_1 \\ u_2 \end{pmatrix} = \begin{pmatrix} 1 & 1 & 2 \\ 1 & 2 & 3 \end{pmatrix} \begin{pmatrix} 1 & 0 & 0 \\ 0 & 1 & 0 \\ 0 & 0 & 1 \end{pmatrix} \begin{pmatrix} 3 \\ 5 \\ 8 \end{pmatrix} \quad (4.18)$$

or

$$\begin{pmatrix} 6 & 9 \\ 9 & 14 \end{pmatrix} \begin{pmatrix} u_1 \\ u_2 \end{pmatrix} = \begin{pmatrix} 22 \\ 37 \end{pmatrix}. \quad (4.19)$$

The least-squares solution of system (4.17) is $(-8\frac{1}{3}, 8)$.

In the LSFEM we can involve boundary condition equations into the operator for boundary elements and make the system overdetermined. This is one of possible ways of implementation of boundary conditions into the LSFEM, which keeps the advantages of the LSFEM.

4.5 Natural coordinate of triangular element

In the FEM, the physical quantities are described by shape (element) functions on the mesh elements. The shape functions can be easily defined in the frame of natural coordinates of

element. Therefore, we use a natural coordinates on the elements, where the basis functions can be simple constructed for an arbitrary order. Unfortunately, the physics is usually defined in the Cartesian coordinates, therefore we need a transformation procedure (see section 4.7). In this section we introduce triangular coordinates (see, e.g., Chung in Chung (2002)).

Natural coordinates l_i are defined in the triangle element as shown in the figure 4.3. As we can see, the coordinates l_i are equal to one on the vertices and zero along the sides with a linear variation in between.

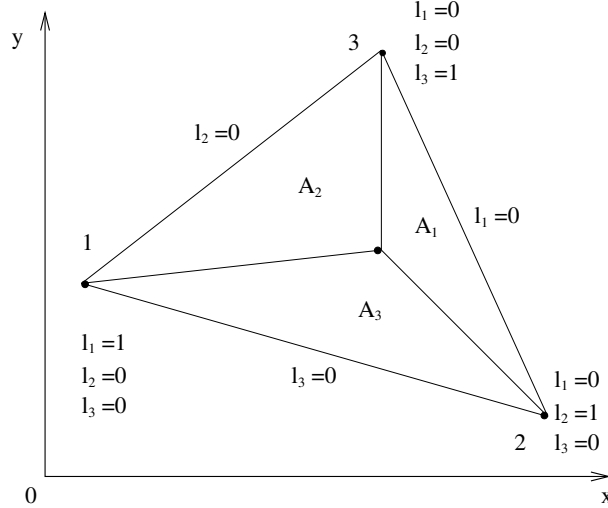


Figure 4.3: The natural coordinate triangular element.

The simple definition of natural coordinates is given by

$$l_i = \frac{A_i}{A}, \quad (4.20)$$

where A is the total area of triangle and A_i are areas obtained by connecting three vertices with any point within the triangle. The total area is given by

$$A = \sum_{i=1}^3 A_i, \quad (4.21)$$

$$1 = \sum_{i=1}^3 l_i. \quad (4.22)$$

We can express the relationship between the Cartesian coordinates x, y and the natural coordinates l_i as

$$x = \sum_{i=1}^3 l_i x_i, \quad (4.23)$$

$$y = \sum_{i=1}^3 l_i y_i. \quad (4.24)$$

The set of equations can be written as

$$\begin{pmatrix} 1 \\ x \\ y \end{pmatrix} = \begin{pmatrix} 1 & 1 & 1 \\ x_1 & x_2 & x_3 \\ y_1 & y_2 & y_3 \end{pmatrix} \begin{pmatrix} l_1 \\ l_2 \\ l_3 \end{pmatrix}. \quad (4.25)$$

We use Cramer's rule for solving set of equations (4.25)

$$l_i = \frac{D_i}{D}, \quad (4.26)$$

where D is the determinant of the equation set

$$D = \det \begin{pmatrix} 1 & 1 & 1 \\ x_1 & x_2 & x_3 \\ y_1 & y_2 & y_3 \end{pmatrix} = 2A \quad (4.27)$$

and D_i are the determinants which are created from D by replacing i -th column of D by the right hand side vector. The solution of equations set (4.25) is

$$l_i = a_i + b_i x + c_i y \quad (4.28)$$

where the constants are

$$\begin{aligned} a_1 &= \frac{1}{D} (x_2 y_3 - x_3 y_2); & a_2 &= \frac{1}{D} (x_3 y_1 - x_1 y_3); & a_3 &= \frac{1}{D} (x_1 y_2 - x_2 y_1); \\ b_1 &= \frac{1}{D} (y_2 - y_3); & b_2 &= \frac{1}{D} (y_3 - y_1); & b_3 &= \frac{1}{D} (y_1 - y_2); \\ c_1 &= \frac{1}{D} (x_3 - x_2); & c_2 &= \frac{1}{D} (x_1 - x_3); & c_3 &= \frac{1}{D} (x_2 - x_1). \end{aligned} \quad (4.29)$$

The cofactor C_{ij} of a matrix (4.25) is

$$a_i = \frac{C_{1i}}{D}, \quad b_i = \frac{C_{2i}}{D}, \quad c_i = \frac{C_{3i}}{D}. \quad (4.30)$$

The cofactor is given by

$$C_{ij} = (-1)^{i+j} M_{ij}, \quad (4.31)$$

where M_{ij} is a minor of matrix (4.25). The minor i, j is a determinant of matrix where i -th row and j -th column are removed. The basis function is in the form

$$u = \sum_{i=1}^3 u_i l_i. \quad (4.32)$$

4.6 Natural coordinate of tetrahedral element

When the 1- or 2-D simplified description is not enough to study phenomena in the physics then we need to extend to 3D elements. The natural tetrahedral coordinates are three dimensional analogy to the natural triangle coordinates. The point, determined by coordinates l_i in the tetrahedron, split it into four smaller parts (also tetrahedrons, see Fig. 4.4) with volumes V_i then the total volume is given by

$$V = \sum_{i=1}^4 V_i, \quad (4.33)$$

$$1 = \sum_{i=1}^4 l_i. \quad (4.34)$$

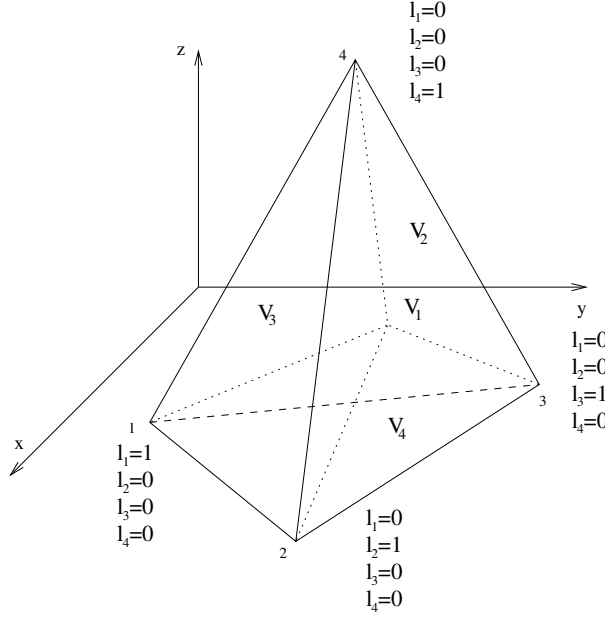


Figure 4.4: Natural coordinates of a tetrahedral element.

The relationship between the Cartesian coordinates and natural tetrahedral coordinates is given by

$$x = \sum_{i=1}^4 l_i x_i, \quad (4.35)$$

$$y = \sum_{i=1}^4 l_i y_i, \quad (4.36)$$

$$z = \sum_{i=1}^4 l_i z_i. \quad (4.37)$$

We can write equations above in the matrix form

$$\begin{pmatrix} 1 \\ x \\ y \\ z \end{pmatrix} = \begin{pmatrix} 1 & 1 & 1 & 1 \\ x_1 & x_2 & x_3 & x_4 \\ y_1 & y_2 & y_3 & y_4 \\ z_1 & z_2 & z_3 & z_4 \end{pmatrix} \begin{pmatrix} l_1 \\ l_2 \\ l_3 \\ l_4 \end{pmatrix}. \quad (4.38)$$

The backward transformation is given by

$$l_i = a_i + b_i x + c_i y + d_i z, \quad (4.39)$$

where the coefficients a_i , b_i , c_i and d_i are again given by

$$a_i = \frac{C_{1i}}{D}, \quad b_i = \frac{C_{2i}}{D}, \quad c_i = \frac{C_{3i}}{D}, \quad d_i = \frac{C_{4i}}{D}. \quad (4.40)$$

4.7 Coordinate transformation

The partial differential equations, which we often solve, are usually in the Cartesian coordinates, but the shape functions are integrated over the elements domain with triangular/tetrahedral coordinates. Therefore, we need a simple way to integrate the least-squares functional. The

integration becomes rather simpler when we transform the Cartesian coordinates to the natural triangular (2D cases) or tetrahedral (3D cases) coordinates. Then, we need to know how to transform the Cartesian operator of partial differential equations to the natural coordinates of the element. The element functions are given in the following form

$$u(x, y, z) = \bar{u}(l_1, \dots, l_n) \quad (4.41)$$

where n is a number of element vertices. The x , y and z are considered to be functions of l_i and between Cartesian and natural coordinates exist a simple linear transformation

$$x = \sum_{i=1}^4 l_i x_i, \quad (4.42)$$

$$y = \sum_{i=1}^4 l_i y_i, \quad (4.43)$$

$$z = \sum_{i=1}^4 l_i z_i. \quad (4.44)$$

Then we determine the transformation of derivatives. The differentiation of basis function is

$$\frac{\partial}{\partial x} u = \frac{\partial}{\partial x} u(x(l_1, \dots, l_n), y(l_1, \dots, l_n), z(l_1, \dots, l_n)) = \frac{\partial}{\partial x} \bar{u} = \sum_{i=1}^n \frac{\partial \bar{u}}{\partial l_i} \frac{\partial l_i}{\partial x}. \quad (4.45)$$

The l_i is given by

$$l_i = a_i + b_i x + c_i y + d_i z, \quad (4.46)$$

Then the differentiation of basis function is simply given by

$$\sum_{i=1}^n \frac{\partial \bar{u}}{\partial l_i} \frac{\partial l_i}{\partial x} = \sum_{i=1}^n u_i b_i. \quad (4.47)$$

Other derivatives we can derived similarly. All derivatives are

$$\begin{aligned} \frac{\partial u}{\partial x} &= \sum_{i=1}^n u_i b_i, \\ \frac{\partial u}{\partial y} &= \sum_{i=1}^n u_i c_i, \\ \frac{\partial u}{\partial z} &= \sum_{i=1}^n u_i d_i. \end{aligned} \quad (4.48)$$

Now any partial differential operator can be expressed in the natural coordinates of an element. It simplify integrating over the element surface/volume by the Gaussian quadrature. The modification of Gaussian quadrature for the natural coordinates is presented in section 4.11.

4.8 Basis functions

The advantage of FEM is the approximation of solution by a shape function on each element thus we know the solution on each point in the entire domain.

The one widely used approach to construct basis shape functions is based on the Lagrange

polynomials. The basis function of the order m is construct by following product

$$\phi_r = \prod_{i=1, i \neq j}^{m+1} \frac{x - x_i}{x_j - x_i} \quad (4.49)$$

where x_j are nodal points where basis functions fulfill condition $\phi_j(x_k) = \delta_{jk}$. The question, how to choose the nodal points x_j , appears. The simplest answer might be to distribute the nodal points equidistantly. However, the equidistant points have bad influence to conditioning of stiffness matrix and interpolation. There exist infinite number of non-equidistant nodal points but we are looking only for points with good properties. Chebyshev introduced a non-equidistant point distribution based on the trigonometric functions

$$x_j = \cos\left(\frac{\pi(j-1)}{m}\right), \quad j = 1, 2, \dots, m+1 \quad (4.50)$$

where we get $m+1$ nodal points for m order basis function. Another option are Gauss-Lobatto points. Unfortunately, there is no explicit formula. The nodal points are roots of the following polynomials

$$(1 - x^2) L'_m(x) \quad (4.51)$$

where $L_m(x)$ is the m -th Legendre polynomial. Chebyshev and Gauss-Lobatto point are very similar and as simulations show the corresponding shape functions are analogous (see Solin (2005)). In the Fig. 4.5 we can see that Chebyshev and equidistant points are equidistant up to the second order.

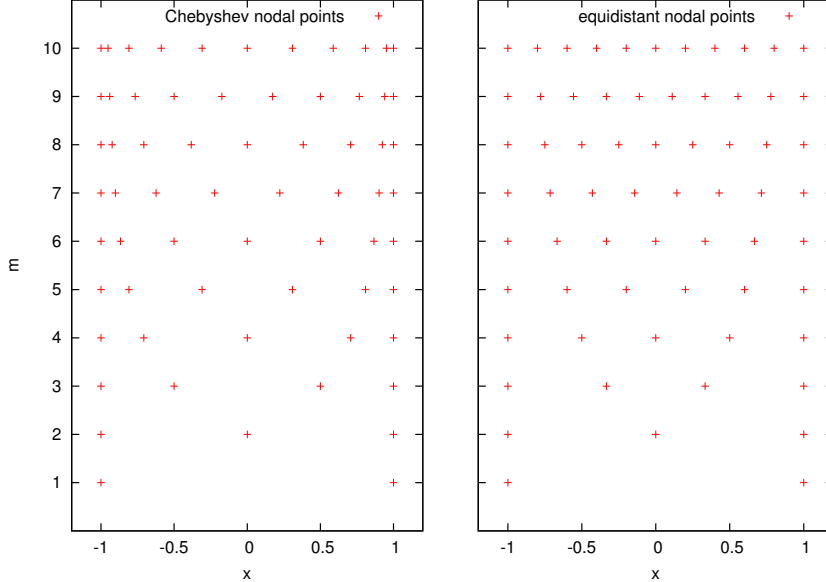


Figure 4.5: Chebyshev nodal points (right) and equidistant nodal points for order $m = 1, 2, \dots, 10$. Chebyshev points have same position as equidistant points up to the second order.

Hierachic shape functions are another way to obtain suitable basis of the polynomial space. The idea of the hierachic approach is based on the extending given basis by a new function.

As an example we introduce Lobatto hierachic shape functions

$$\begin{aligned} l_0(\xi) &= \frac{1-\xi}{2}, \quad l_1(\xi) = \frac{1+\xi}{2} \\ l_k(\xi) &= \int_{-1}^{\xi} L_{k-1}(\rho) d\rho \end{aligned} \quad (4.52)$$

where L_k are the normalized Legendre polynomials.

We use Lagrange polynomial functions as the interpolation functions because functions can be constructed directly for natural coordinates and for the low order (up to second order) shape functions there is no difference at position of the nodal points. Any polynomial function of order m can be assembled by the following procedure

$$B^r(l_N) = \begin{cases} \prod_{s=1}^{s=d} \frac{1}{s}(ml_N - s + 1) & \text{for } d \geq 1 \\ 1 & \text{for } d = 0 \end{cases} \quad (4.53)$$

where $d = ml_N$, $N = 1, 2, \dots, n$; $r = 1, 2, \dots, n$ and n is a total number of nodes. Here l_N^r represents values of area coordinates at each node. The interpolation (basis, vertex) functions are given by

$$\phi_r = B^r(l_1)B^r(l_2)B^r(l_3) \quad (4.54)$$

The shape (element) function u^e is given by

$$u^e = \sum_i^n u_i \phi_i \quad (4.55)$$

where u_i are nodal values. Fig. 4.6 shows an example of coordinates of nodes in triangle elements for high order shape functions. In order to demonstrate how to assemble a shape function we

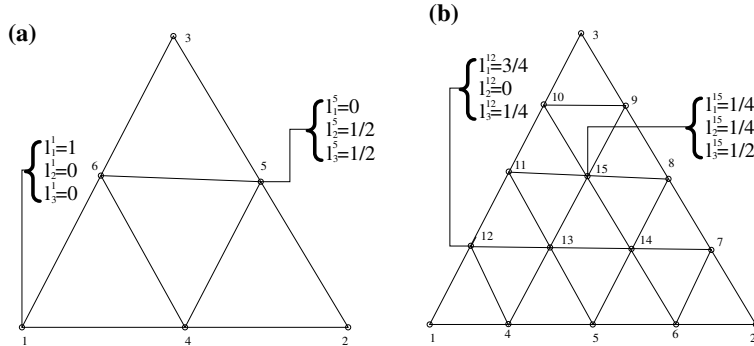


Figure 4.6: Coordinates of a high order shape functions. (a) quadratic ($m = 2$); (b) quartic ($m = 4$).

derive a second order shape function. The second order shape function ($m = 2$) consist of six basis functions ϕ_r . The first vertex function is given by equation (4.53) for coordinates $(l_1^1, l_2^1, l_3^1) = (1, 0, 0)$. We get

$$\begin{aligned} B^1(l_1) &= \frac{1}{1}(2l_1 - 1 + 1) \frac{1}{2}(2l_1 - 2 + 1) = l_1(2l_1 - 1), \\ B^1(l_2) &= 1, \\ B^1(l_3) &= 1, \end{aligned}$$

Now we put these equations together and obtain the first vertex function

$$\phi_1 = B^1(l_1)B^1(l_2)B^1(l_3) = l_1(2l_1 - 1).$$

The second and third basis functions are similar to the first one. A coordinates of a four-th basis function are $(l_1^4, l_2^4, l_3^4) = (\frac{1}{2}, \frac{1}{2}, 0)$ and derivation of vertex functions is following

$$\begin{aligned} B^4(l_1) &= \frac{1}{1}(2l_1 - 1 + 1) = 2l_1, \\ B^4(l_2) &= \frac{1}{1}(2l_2 - 1 + 1) = 2l_2, \\ B^4(l_3) &= 1 \end{aligned}$$

and the corresponding element function reads

$$\phi_4 = B^4(l_1)B^4(l_2)B^4(l_3) = 4l_1l_2.$$

The five-th and six-th basis functions are again similar to the fourth basis function.

The figures 4.7, 4.8 and 4.9 show basis functions for triangle element for first, second and third order of polynomial interpolation based on the Lagrange polynomials with equidistant nodal points.

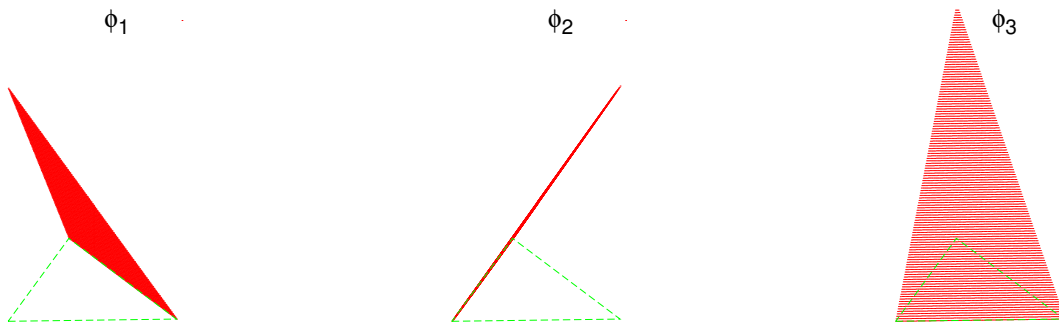


Figure 4.7: Nodal basis of the first order triangle element. Vertex functions ϕ_1 , ϕ_2 and ϕ_3 .

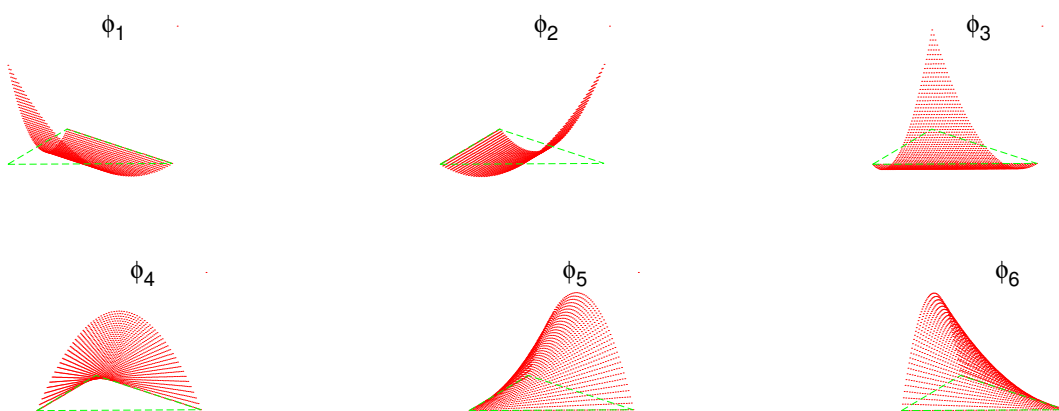


Figure 4.8: Nodal basis of the second order triangle element. Vertex functions ϕ_1 , ϕ_2 and ϕ_3 . Edge functions ϕ_4 , ϕ_5 and ϕ_6 .

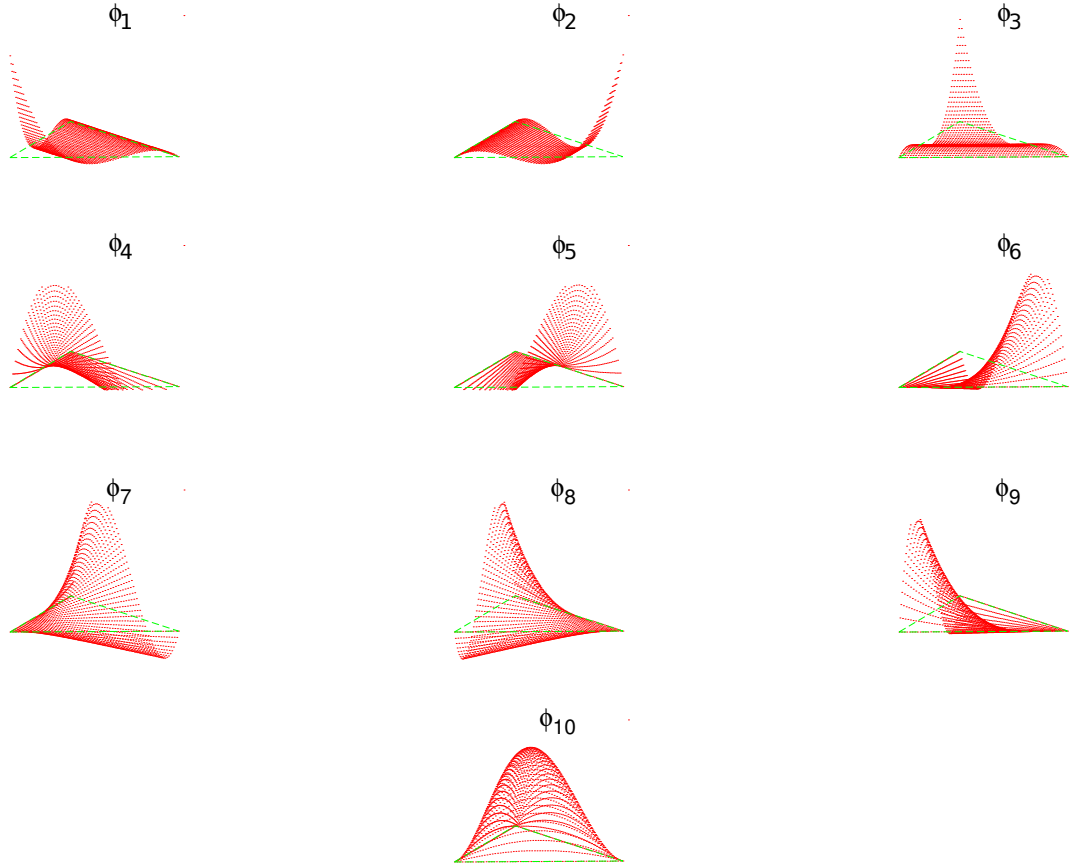


Figure 4.9: Nodal basis of the third order triangle element. Vertex functions ϕ_1 , ϕ_2 and ϕ_3 . Edge functions ϕ_4 , ϕ_5 , ϕ_6 , ϕ_7 , ϕ_8 and ϕ_9 . Bubble function ϕ_{10} .

4.9 Time discretization and linearization

Generally, the operators of formal LSFEM problem (4.3) can be in the nonlinear form. We need to transform these operators into the linear and time discretized form for computational purposes. The linearization of the operator can be achieved by lagging the nonlinear term straightforwardly. This simple iteration method (also called successive substitution method) has slow convergence rate and large radius of convergence. To improve rate of convergence, we can apply the attractive Newton-Raphson linearization method due to its quadratic convergence rate (see Dennis and Schmabel (1996)). The Newton-Raphson method is a powerful and widely used technique for solving nonlinear equations numerically but has a small radius of convergence.

Let start with a system of partial differential equations in the conservative form

$$\frac{\partial \Psi_1}{\partial t} + \Psi_2 + \frac{\partial \mathbf{F}_i}{\partial x_i} = 0, \quad (4.56)$$

where \mathbf{F}_i is a flux in the direction of coordinate x_i and $\Psi = \Psi_1 + \Psi_2$ is a state vector. The fluxes \mathbf{F}_i are generally nonlinear and they need to be linearized. The time derivation of state vector in the previous equation needs to be discretized. Firstly, we use the θ -time discretization scheme in order to remove time derivation

$$\frac{\Psi_1 - \bar{\Psi}_1}{\Delta t} + \Psi_2 + \theta \frac{\partial \mathbf{F}_i}{\partial x_i} + (1 - \theta) \frac{\partial \bar{\mathbf{F}}_i}{\partial x_i} = 0. \quad (4.57)$$

In the case where $\Psi_1 = 0$ the equation (4.57) is simply given by

$$\Psi_2 + \frac{\partial \mathbf{F}_i}{\partial x_i} = 0. \quad (4.58)$$

The terms denoted by over-line are values from the last time step. For the Newton-Raphson linearization we expand term \mathbf{F}_i into the Taylor series

$$\mathbf{F}_i(\Psi^{k+1}) = \mathbf{F}_i(\Psi^k) + \left. \frac{\partial \mathbf{F}_i}{\partial \Psi} \right|_k (\Psi^{k+1} - \Psi^k), \quad (4.59)$$

inserting this equation into the equation (4.57) we get

$$\Psi + \theta \Delta t \frac{\partial}{\partial x_i} \left(\mathbf{F}_i(\Psi^k) + \left. \frac{\partial \mathbf{F}_i}{\partial \Psi} \right|_k (\Psi^{k+1} - \Psi^k) \right) = \bar{\Psi}_1 - (1 - \theta) \Delta t \frac{\partial \bar{\mathbf{F}}_i}{\partial x_i}. \quad (4.60)$$

we denote the Jacobian matrix $\mathbf{A}_i^k = \frac{\partial \mathbf{F}_i}{\partial \Psi}|_k$ and using the relationship $\frac{\partial \mathbf{F}_i(\Psi^k)}{\partial x_i} = \frac{\partial \mathbf{F}_i(\Psi^k)}{\partial \Psi} \frac{\partial \Psi}{\partial x_i} = \mathbf{A}_i^k \frac{\partial \Psi^k}{\partial x_i}$ we obtain

$$\Psi^{k+1} + \theta \Delta t \left(\mathbf{A}_i^k \frac{\partial \Psi^k}{\partial x_i} + \mathbf{A}_i^k \Psi^{k+1} + \mathbf{A}_i^k \frac{\partial \Psi^{k+1}}{\partial x_i} - \frac{\partial \mathbf{A}_i^k}{\partial x_i} \Psi^k - \mathbf{A}_i^k \frac{\partial \Psi^k}{\partial x_i} \right) = \bar{\Psi}_1 - (1 - \theta) \Delta t \frac{\partial \bar{\mathbf{F}}_i}{\partial x_i}. \quad (4.61)$$

After few algebraic operations we finally receive a system of linear differential equations

$$\Psi^{k+1} + \theta \Delta t \left(\frac{\partial \mathbf{A}_i^k}{\partial x_i} \Psi^{k+1} + \mathbf{A}_i^k \frac{\partial \Psi^{k+1}}{\partial x_i} \right) = \bar{\Psi}_1 - \Delta t \left((1 - \theta) \frac{\partial \bar{\mathbf{F}}_i}{\partial x_i} - \theta \frac{\partial \mathbf{A}_i^k}{\partial x_i} \Psi^k \right). \quad (4.62)$$

In the case when $\Psi_1 = 0$

$$\Psi^{k+1} + \frac{\partial \mathbf{A}_i^k}{\partial x_i} \Psi^{k+1} + \mathbf{A}_i^k \frac{\partial \Psi^{k+1}}{\partial x_i} = \frac{\partial \mathbf{A}_i^k}{\partial x_i} \Psi^k. \quad (4.63)$$

Then the operator \mathcal{A} from equation (4.9) reads

$$\mathcal{A} = 1 + \theta \Delta t \left(\frac{\partial \mathbf{A}_i^k}{\partial x_i} + \mathbf{A}_i^k \frac{\partial}{\partial x_i} \right) \quad (4.64)$$

and corresponding right hand side has following form

$$\mathbf{f} = \bar{\Psi}_1 - \frac{\Delta t}{2} \left(\frac{\partial \bar{\mathbf{F}}_i}{\partial x_i} - \frac{\partial \mathbf{A}_i^k}{\partial x_i} \Psi^k \right). \quad (4.65)$$

When we deal with second order partial differential equations we can also use linearization directly to the second order operator (when we do not turn second order equation into a set of first order equations). The analytic derivation of linearized operator is more complicated than in the case of a first order operator and it requires to use the second or higher order of basis functions – if we use only a first order functions then terms with second derivatives in the operator become zero and the FEM loose second order accuracy.

The system of second order partial differential equations has following conservative form

$$\frac{\partial \Psi}{\partial t} + \frac{\partial \mathbf{F}(\Psi)_i}{\partial x_i} + \frac{\partial \mathbf{G}(\Psi, \Psi'_{,j})_i}{\partial x_i} = \mathbf{S}, \quad (4.66)$$

where $\Psi'_{,j}$ is a derivative of Ψ with respect to j -th coordinate. Similarly as in previous derivation of the operator \mathcal{A} , we use the Crank-Nicolson discretization scheme as a special case of θ -scheme

$$(\theta = \frac{1}{2})$$

$$\boldsymbol{\Psi} + \frac{\Delta t}{2} \left(\frac{\partial \mathbf{F}_i(\bar{\boldsymbol{\Psi}})}{\partial x_i} + \frac{\partial \mathbf{F}_i(\boldsymbol{\Psi})}{\partial x_i} + \frac{\partial \mathbf{G}_i(\bar{\boldsymbol{\Psi}}, \bar{\boldsymbol{\Psi}}'_{ij})}{\partial x_i} + \frac{\partial \mathbf{G}_i(\boldsymbol{\Psi}, \boldsymbol{\Psi}'_{ij})}{\partial x_i} \right) = \bar{\boldsymbol{\Psi}} + \bar{\mathbf{S}}^{\frac{1}{2}}, \quad (4.67)$$

the $\bar{\mathbf{S}}^{\frac{1}{2}}$ is a source vector at the half time step. We define

$$\mathbf{R} \equiv \bar{\boldsymbol{\Psi}} + \Delta t \bar{\mathbf{S}}^{\frac{1}{2}} - \frac{\Delta t}{2} \left(\frac{\partial \mathbf{F}_i(\bar{\boldsymbol{\Psi}})}{\partial x_i} + \frac{\partial \mathbf{G}_i(\bar{\boldsymbol{\Psi}}, \bar{\boldsymbol{\Psi}}'_{ij})}{\partial x_i} \right), \quad (4.68)$$

for a shorter notation. The equation (4.68) is nonlinear then we transform it to the linear form with using the Newton-Raphson iterative method

$$\mathbf{F}_i(\boldsymbol{\Psi}^{k+1}) = \mathbf{F}_i(\boldsymbol{\Psi}^k) + \frac{\partial \mathbf{F}_i}{\partial \boldsymbol{\Psi}} \Big|_k (\boldsymbol{\Psi}^{k+1} - \boldsymbol{\Psi}^k) \quad (4.69)$$

and the second order (e.g. diffusion) term expands as

$$\mathbf{G}_i(\boldsymbol{\Psi}^{k+1}, \boldsymbol{\Psi}'_{ij}^{k+1}) = \mathbf{G}_i(\boldsymbol{\Psi}^k, \boldsymbol{\Psi}'_{ij}^k) + \frac{\partial \mathbf{G}_i}{\partial \boldsymbol{\Psi}} \Big|_k (\boldsymbol{\Psi}^{k+1} - \boldsymbol{\Psi}^k) + \frac{\partial \mathbf{G}_i}{\partial \boldsymbol{\Psi}'_{ij}} \Big|_k \left(\frac{\partial \boldsymbol{\Psi}^{k+1}}{\partial x_j} - \frac{\partial \boldsymbol{\Psi}^k}{\partial x_j} \right). \quad (4.70)$$

We denote $\mathbf{A}_i^k = \frac{\partial \mathbf{F}_i}{\partial \boldsymbol{\Psi}} \Big|_k$, $\mathbf{B}_i^k = \frac{\partial \mathbf{G}_i}{\partial \boldsymbol{\Psi}} \Big|_k$ and $\mathbf{C}_{ij}^k = \frac{\partial \mathbf{G}_i}{\partial \boldsymbol{\Psi}'_{ij}} \Big|_k$. Now we insert linearized terms (4.69) and (4.70) into the nonlinear equation (4.67) and then we obtain a linearized equation

$$\begin{aligned} \boldsymbol{\Psi}^{k+1} + \frac{\Delta t}{2} \left(\frac{\partial(\mathbf{A}_i + \mathbf{B}_i)}{\partial x_i} \boldsymbol{\Psi}^{k+1} + (\mathbf{A}_i + \mathbf{B}_i) \frac{\partial \boldsymbol{\Psi}^{k+1}}{\partial x_i} + \frac{\partial \mathbf{C}_{ij}}{\partial x_i} \frac{\partial \boldsymbol{\Psi}^{k+1}}{\partial x_j} + \mathbf{C}_{ij} \frac{\partial^2 \boldsymbol{\Psi}^{k+1}}{\partial x_i \partial x_j} \right) &= \\ &= \mathbf{R} + \frac{\Delta t}{2} \left(\frac{\partial(\mathbf{A}_i + \mathbf{B}_i)}{\partial x_i} \boldsymbol{\Psi}^k + \frac{\partial \mathbf{C}_{ij}}{\partial x_i} \frac{\partial \boldsymbol{\Psi}^k}{\partial x_j} \right). \end{aligned} \quad (4.71)$$

In the derivation of former equation we used the relationship $\frac{\partial \mathbf{G}_i}{\partial x_i} = \frac{\partial \mathbf{G}_i}{\partial \boldsymbol{\Psi}} \frac{\partial \boldsymbol{\Psi}}{\partial x_i} + \frac{\partial \mathbf{G}_i}{\partial \boldsymbol{\Psi}'_{ij}} \frac{\partial \boldsymbol{\Psi}'_{ij}}{\partial x_i}$. The final form of linearized equation is given by

$$\begin{aligned} \left[\mathbf{I} + \frac{\Delta t}{2} \left(\frac{\partial(\mathbf{A}_i + \mathbf{B}_i)}{\partial x_i} + (\mathbf{A}_i + \mathbf{B}_i) \frac{\partial}{\partial x_i} + \frac{\partial \mathbf{C}_{ij}}{\partial x_i} \frac{\partial}{\partial x_j} + \mathbf{C}_{ij} \frac{\partial^2}{\partial x_i \partial x_j} \right) \right] \boldsymbol{\Psi}^{k+1} &= \\ &= \bar{\boldsymbol{\Psi}} + \Delta t \bar{\mathbf{S}}^{\frac{1}{2}} - \frac{\Delta t}{2} \left(\frac{\partial \bar{\mathbf{F}}_i}{\partial x_i} + \frac{\partial \bar{\mathbf{G}}_i}{\partial x_i} \right) + \frac{\Delta t}{2} \left(\frac{\partial(\mathbf{A}_i + \mathbf{B}_i)}{\partial x_i} \boldsymbol{\Psi}^k + \frac{\partial \mathbf{C}_{ij}}{\partial x_i} \frac{\partial \boldsymbol{\Psi}^k}{\partial x_j} \right). \end{aligned} \quad (4.72)$$

4.10 Element-by-Element

When we are solving a large system of equations then problem with assembling matrix arise. This process can be very time expensive and also memory demanding. The Element-By-Element method (see, e.g., Chung (2002) and Jiang (1998)) allows us to bypass assembling of a large sparse matrix. We investigate this iterative method in following text. A set of linear algebraic equations arise from LSFEM reads

$$\mathbf{K}\mathbf{u} = \mathbf{f}. \quad (4.73)$$

The matrix can be split \mathbf{K} into the diagonal components \mathbf{D} and the off-diagonal matrix \mathbf{N} as follows

$$(\mathbf{D} + \mathbf{N})\mathbf{u} = \mathbf{f}. \quad (4.74)$$

We introduce a following iterative scheme

$$\mathbf{D}\mathbf{u}^{r+1} \cong \mathbf{f} - \mathbf{N}\mathbf{u}^r. \quad (4.75)$$

where r denote the iterative step of \mathbf{u} . Subtracting $\mathbf{D}\mathbf{u}^r$ from both sides of (4.75), we obtain

$$\mathbf{D}(\mathbf{u}^{r+1} - \mathbf{u}^r) \cong \mathbf{f} - (\mathbf{N} + \mathbf{D})\mathbf{u}^r. \quad (4.76)$$

Terms with \mathbf{u} we move to the right hand side

$$\mathbf{u}^{r+1} \cong \mathbf{u}^r - \mathbf{D}^{-1}(\mathbf{K}\mathbf{u}^r - \mathbf{f}). \quad (4.77)$$

All terms can by expressed as column vectors. The term $\mathbf{K}\mathbf{u}^r$ is calculated for each element and for all its nodal values. As a result we get new nodal value \mathbf{u}^{r+1} depending only on the vectors from last iterative step r

$$\begin{pmatrix} u_1 \\ u_2 \\ \vdots \end{pmatrix}^{r+1} = \begin{pmatrix} u_1 \\ u_2 \\ \vdots \end{pmatrix}^r - \begin{pmatrix} (\mathbf{K}\mathbf{u}^r - f_1)/D_{11} \\ (\mathbf{K}\mathbf{u}^r - f_2)/D_{22} \\ \vdots \end{pmatrix}^r \quad (4.78)$$

In order to increase the convergence rate and accuracy we implement also a standard relaxation process in the form

$$\mathbf{u}^{r+1} = \xi \mathbf{u}^{r+1} + (1 - \xi) \mathbf{u}^r, \quad (4.79)$$

where $0 < \xi < 1$.

As this method save the time and memory on the construction of the sparse matrix it has, at the same time, slower convergence rate then CGM or JCGM which solves system with stiffness matrix. Therefore, the Element-By-Element method is suitable for computers systems with lower performance and memory as well as simpler physical problems.

4.11 Gaussian quadrature

In order to evaluate integrals in the LSFEM (see Eq. 4.9) we need a fast and accurate numeric method. The best choice is the Gaussian quadrature where with n integration points it exactly solves polynomials of degree $2n - 1$ or less. The Gaussian quadrature is a sum of weighted integrate function in the suitable choose points:

$$\int_{-1}^1 f(x)dx \approx \sum_{i=1}^n w_i f(x_i) \quad (4.80)$$

The weights w_i and integrated points x_i can be derived when we assume the integrated function as a polynomial of degree $2n - 1$ for n -points quadrature. It leads into $2n$ equations for n integrated points x_i and n weights w_i . The values of points x_i and their weights are shown in the table 4.1.

Unfortunately, the FEM integrates shape functions over a triangular (in two dimensions) or tetrahedral (in three dimensions) sub-domain. The Gaussian quadrature is still applicable in the double sum (2D) or triple sum (3D) form. As the basis functions are defined in natural triangle or tetrahedron coordinates, we need to transform the integral to be able to use the Gaussian quadrature. The limits of integration for a basis function are from 0 to 1, the Gaussian quadrature requires integration limits from -1 to 1. The transformation for triangle is, in detail, described in the work of Rathod et al. (2004). The Gaussian quadrature over triangle has following form

n	x_i	w_i
2	$+\frac{\sqrt{3}}{3}$	1
	$-\frac{\sqrt{3}}{3}$	1
3	0	$\frac{8}{9}$
	$+\sqrt{\frac{3}{5}}$	$\frac{8}{9}$
	$-\sqrt{\frac{3}{5}}$	$\frac{8}{9}$
4	$+\sqrt{\frac{15-2\sqrt{30}}{35}}$	$\frac{18+\sqrt{30}}{36}$
	$-\sqrt{\frac{15-2\sqrt{30}}{35}}$	$\frac{18+\sqrt{30}}{36}$
	$+\sqrt{\frac{15+2\sqrt{30}}{35}}$	$\frac{18-\sqrt{30}}{36}$
	$+\sqrt{\frac{15+2\sqrt{30}}{35}}$	$\frac{18-\sqrt{30}}{36}$
5	0	$\frac{128}{225}$
	$+\sqrt{\frac{35-2\sqrt{70}}{63}}$	$\frac{322+13\sqrt{70}}{900}$
	$-\sqrt{\frac{35-2\sqrt{70}}{63}}$	$\frac{322+13\sqrt{70}}{900}$
	$+\sqrt{\frac{35+2\sqrt{70}}{63}}$	$\frac{322-13\sqrt{70}}{900}$
	$-\sqrt{\frac{35+2\sqrt{70}}{63}}$	$\frac{322-13\sqrt{70}}{900}$
\vdots	\vdots	\vdots

Table 4.1: The integrated points and weights of Gaussian quadrature.

$$\int_{-1}^1 \int_{-1}^1 f(l_1(x, y), l_2(x, y), l_3(x, y)) \frac{1-x}{8} dx \approx \sum_{i=1}^n \sum_{j=1}^n \frac{1-x_i}{8} w_i w_j f\left(\frac{1+x_i}{2}, \frac{(1-x_i)(1+y_j)}{4}\right). \quad (4.81)$$

The derivation for a tetrahedron domain is similar to the triangle domain. We generally integrate an arbitrary function f over a volume of tetrahedron

$$I = \int_0^1 dl_1 \int_0^{1-l_1} dl_2 \int_0^{1-l_1-l_2} f(l_1, l_2, l_3, l_4) dl_3, \quad (4.82)$$

where $l_4 = 1 - l_1 - l_2 - l_3$. The integral (4.82) can be transformed into the integral over a cube domain $(u, v, w); 0 \leq (u, v, w) \leq 1$ by the substitution:

$$l_1 = u; \quad l_2 = (1-u)v; \quad l_3 = (1-u-v+uv)w. \quad (4.83)$$

Then the determinant of Jacobian and differential volume are

$$\frac{\partial(l_1, l_2, l_3)}{\partial(u, v, w)} = (1-u)(1-u-v+uv) \quad (4.84)$$

and

$$dl_1 dl_2 dl_3 = (1-u)(1-u-v+uv) du dv dw. \quad (4.85)$$

The transformed integral is following

$$\int_0^1 dl_1 \int_0^{1-l_1} dl_2 \int_0^{1-l_1-l_2} f(l_1, l_2, l_3, l_4) dl_3 = \\ \int_0^1 \int_0^1 \int_0^1 f(u, (1-u)v, (1-u-v+uv)w) (1-u)(1-u-v+uv) du dv dw, \quad (4.86)$$

The integral (4.82) can be transformed further into the integral over a cube domain $(x, y, z); -1 \leq (x, y, z) \leq 1$ by the substitution:

$$u = \frac{1+x}{2}; u = \frac{1+y}{2}; u = \frac{1+z}{2}. \quad (4.87)$$

The determinant of Jacobian and differential volume are

$$\frac{\partial(u, v, w)}{\partial(x, y, z)} = \frac{1}{8} \quad (4.88)$$

and

$$dudvdw = \frac{1}{8} dx dy dz. \quad (4.89)$$

Finally, using equations (4.88) and (4.89) in (4.86), we have

$$I = \int_0^1 \int_0^1 \int_0^1 f\left(\frac{1+x}{2}, \frac{(1-x)(1+y)}{4}, \left(\frac{(1+x)(1+y)}{4} - \frac{x+y}{2}\right) \frac{1+z}{2}\right) \\ w_i w_j w_k \frac{x-1}{16} \left(\frac{x+y}{2} + \frac{(1+x)(1+y)}{2}\right) dx dy dz. \quad (4.90)$$

The integration by the Gaussian quadrature over tetrahedron is

$$I = \sum_{i=1}^n \sum_{j=1}^n \sum_{k=1}^n f\left(\frac{1+x_i}{2}, \frac{(1-x_i)(1+y_j)}{4}, \left(\frac{(1+x_i)(1+y_j)}{4} - \frac{x_i+y_j}{2}\right) \frac{1+z_k}{2}\right) \\ w_i w_j w_k \frac{x_i-1}{16} \left(\frac{x_i+y_j}{2} + \frac{(1+x_i)(1+y_j)}{2}\right), \quad (4.91)$$

where x_i , y_j and z_k are values of Gaussian points.

4.12 Iteratively re-weighted LSFEM

Since hyperbolic equations may produce shocks the L_2 norm causes spreading of oscillations near the shocks. This trouble comes from fact that discretized equations can not hold infinity derivatives in the shock elements. The LSFEM force discretized equations on the shock elements to be satisfied everywhere, and this leads to an oscillatory solution around the shock front. This problem is rigorously solved by using L_1 norm, but this solution leads to a linear programming which is expensive. Another way is to use an different indirect method – if we can identify the shock element and allow the equations in the shock elements not to be (fully) satisfied then the equations in the remaining elements can be satisfied exactly – the solution will have no oscillations. The shock elements can be found iteratively. The iteratively re-weighted LSFEM is proposed in Jiang (1993), Jiang (1998) and Bochev and Gunzburger (2009). The functional

of iteratively re-weighted method is following

$$I(\mathbf{u}) = w_l \int_{\Omega} (\mathbf{A}\mathbf{u} - \mathbf{f})^2 d\Omega, \quad (4.92)$$

where weight w_l is set for each element by a formula

$$w_l = \frac{1}{|R_l|^6 + \epsilon}, \quad (4.93)$$

where R_l is a residual of element l , ϵ is a small positive number, for example like a $\epsilon = 10^{-20}$, to prevent an overflow in computation. The initial value of weights w_l are set to 1.0. In the second (and greater) iteration, the residual $|R_l|$ is larger in the shock elements, for this reason the weight w_l is smaller for shock elements and their influence to surrounding elements is reduced. The iterations are stopped when the difference between old and new solution $|\mathbf{u}_{new} - \mathbf{u}_{old}|$ is sufficiently small. We can also use another simple shock element indicator. We can check how much values in the elements is varying. In the shock elements is this varying of values greater than in the smooth elements. The variation is defined as

$$V = \sum_{m=1}^N |u_m - u_{m-1}| \quad u_0 = u_N. \quad (4.94)$$

Further, the corresponding weight is

$$w_l = \begin{cases} 10^{15} & \text{if } |V|^6 < 10^{-7} \\ \frac{1}{|V|^6} & \text{if } |V|^6 \geq 10^{-7}. \end{cases} \quad (4.95)$$

The iteratively re-weighted LSFEM successfully reduce the smearing of discontinuities. The implementation of this method is relatively easy.

4.13 LSFEM implementation of MHD

At the first we divide the global domain into elements. We use triangle elements in whole domain. The method of mesh generation has been described by Chung (2002). The second step is mapping a shape functions on the given mesh – creating a function space.

Next part of initialization is to set initial condition. The state vector of each node is set to values according to its global spatial coordinates as it is prescribed by given analytic initial conditions.

When we have initial mesh and function space we can continue into the main loop of the code. The top loop is counting a time and it contains control of the time step size Δt , linearization loop, Gaussian integration, assembling sparse stiffness matrix and load vector and solving a system of linear equations. The time step is set according to the Courant-Friedrichs-Lowy condition. At first we determine the maximum speed in the whole domain

$$c_s = \sqrt{\frac{\gamma(\gamma-1)}{\rho} (U - \rho\mathbf{v}^2 - U_B)}, \quad (4.96)$$

$$v_A = \sqrt{\frac{\mathbf{B}^2}{\rho}}, \quad (4.97)$$

$$v = \frac{\sqrt{\boldsymbol{\pi}^2}}{\rho}, \quad (4.98)$$

$$v_{max} = c_s + v_A + v, \quad (4.99)$$

where c_s is the sound speed, v_A is the Alfvén speed and v is the plasma macroscopic speed. We use a simple sum of speed terms in order to count with a greater speed and smaller time step. The time step is also dependent on the minimum mesh size Δx . It is found during an initialization of mesh or during mesh refinement. The time step is also affected by the resistivity term. We commutate both time steps and choose less one

$$\Delta t = \min \begin{cases} c_{\Delta t} \frac{\Delta x_{min}}{v_{max}} \\ c_{\Delta t} \frac{\Delta x_{min}}{2\eta_{max}} \end{cases} \quad (4.100)$$

The next loop is over linearization (see section 4.9). It finds a solution of sparse stiffness matrix and checks difference between a solution of the last linearization. If it is under the required accuracy $\frac{|\mathbf{u}^k - \mathbf{u}^{k+1}|}{|\mathbf{u}^{k+1}|} < \varepsilon$ the program continues to the next time step. The linearization loop usually finishes in 2-3 steps when the accuracy 10^{-8} is reached. The stiffness matrix assembling and solving in the linearization loop is following. The stiffness matrix is assembled element by element. In the element loop we integrate terms in equation (4.9). The Gaussian quadrature Chung (2002) is used for an integration where the transformation into natural triangle coordinates is used, Rathod et al. (2004). For a faster evaluation of integrals we calculate and store operators applied on each interpolation (basis) function for given Gaussian point $\mathcal{A}\Phi_i$. We add the multiplied operators $\mathcal{A}^T \Phi_i \mathbf{W} \mathcal{A}\Phi_j$ into the stiffness matrix in positions according to the global nodal indexes and also we add multiplied operator with right hand side $\mathcal{A}^T \Phi_i \mathbf{W} \mathbf{f}$ into the load vector. When we sum sub-matrices and sub-vectors for all Gaussian points then we continue to the next element until the entire stiffness matrix and Load vector are assembled. The system of equations given by stiffness matrix and Load vector is solved by the Jacobi preconditioned Conjugate Gradient Method (JCGM) Press et al. (2007). The JCGM usually takes few tens of iteration to reach required precision (10^{-10}), where the speed of convergence (almost) do not depend on the size of the matrix. If the divergence equation is involved in the MHD equations (i.e. we solve overdetermined system) then the condition number of stiffness matrix significantly increase (i.e. from $\sim 10^0$ to $\sim 10^4$) and the JCGM takes 10 – 50 times more iterations. When we obtain solution from JCGM, then the program continues to the linearization loop. The entire algorithm can be summarized as follows:

- time loop – adapt time step size according to CFL condition, check final desired time
- linearization loop – if $\frac{|\mathbf{u}^k - \mathbf{u}^{k+1}|}{|\mathbf{u}^{k+1}|} < \varepsilon$ or maximum iteration count is reached continue to next time step
 - assembling stiffness matrix \mathbf{K} element by element
 - integration by Gaussian quadrature
 1. compute the operator matrices for each basis function
 2. multiply the operator matrices then add the result into stiffness matrix
 3. multiply the operator matrix by the RHS then add result into the load vector
 - next Gaussian point
 - next element
 - find new solution \mathbf{u}^{k+1} of stiffness system (4.10) by the JCGM
 - next linearization
 - next time step

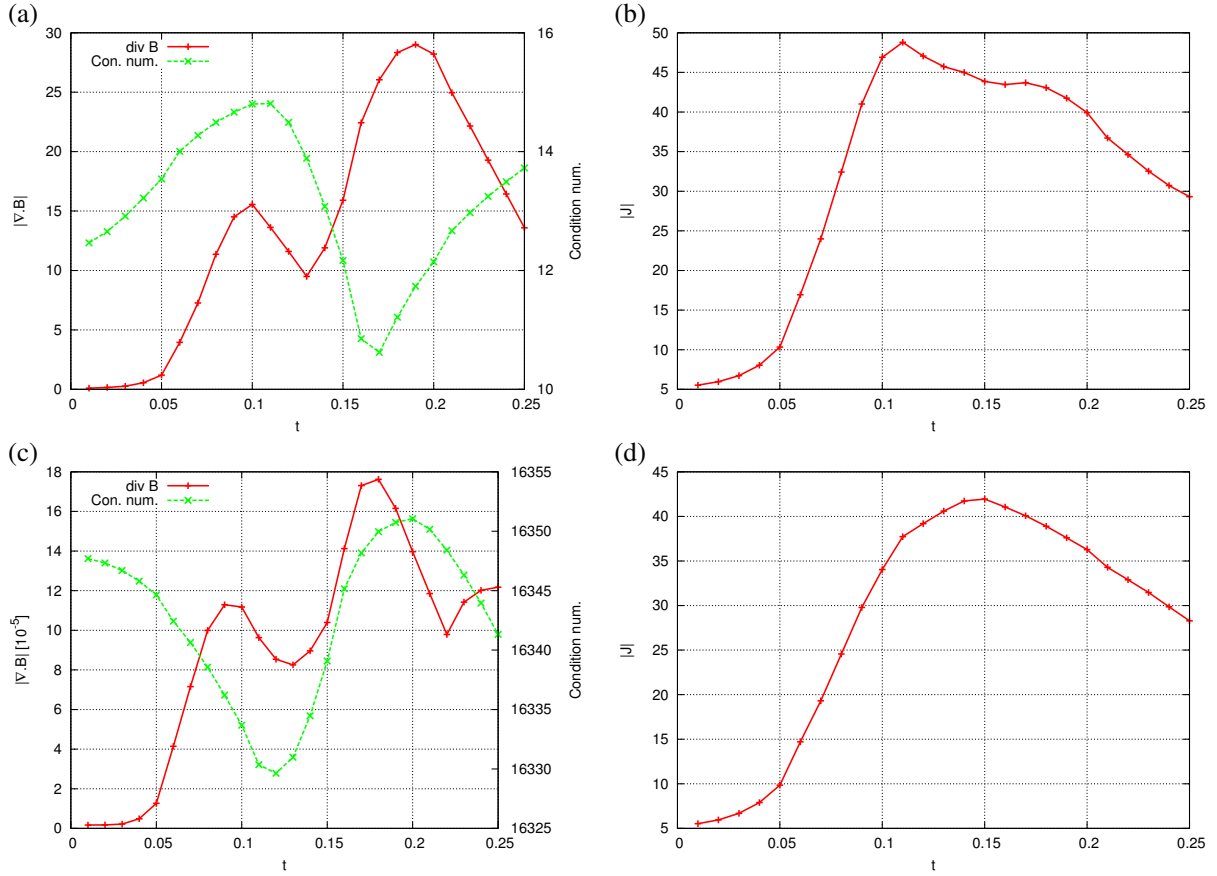


Figure 4.10: Plots (a), (c) show a time evolution of $\nabla \cdot \mathbf{B}$ and condition number of stiffness matrix and plots (b), (d) show the maximum current density. Plots (a), (b) represent solution with divergence equation and plots (a), (b) are without divergence equation. The simulation was performed using a homogeneous mesh consisting of $2 \times 64 \times 64$ triangles.

4.14 Influence of overdetermined system

The advantage of LSFEM is possibility to solve overdetermined system. During solving this system, a new question arise: what is an influence of more equations then the number of variables to the resulting system of linear algebraic equations? We investigate this question by a numeric simulation in this section.

In order to address this question we performed a numeric simulation based on the Orszag-Tang vortex problem (see section 5.2). This ideal (non-resistive) MHD test develops vortices, shocks and a high current density over the time, therefore it is an suitable test for studying influence of additional $\nabla \cdot \mathbf{B} = 0$ equation.

The inclusion of solenoidal condition $\nabla \cdot \mathbf{B} = 0$ into MHD equations leads to minimize a magnetic charge as we expected. Unfortunately, the solenoidal condition also significantly increases a condition number of the stiffness matrix. The numerical test reveals, that the condition number of stiffness matrix is related to the current density – current density and magnetic divergence are given by the derivatives of magnetic field. In the case of small current density the condition number almost remains unchanged. When the current density is increasing then the derivatives of magnetic field in the solenoidal condition steeply grows and the condition number of stiffness matrix increases as well.

The figures 4.10, 4.11, 4.12 present a time evolution of divergence \mathbf{B} , condition number of stiffness matrix and maximum current density for a different resolution of a mesh. These results

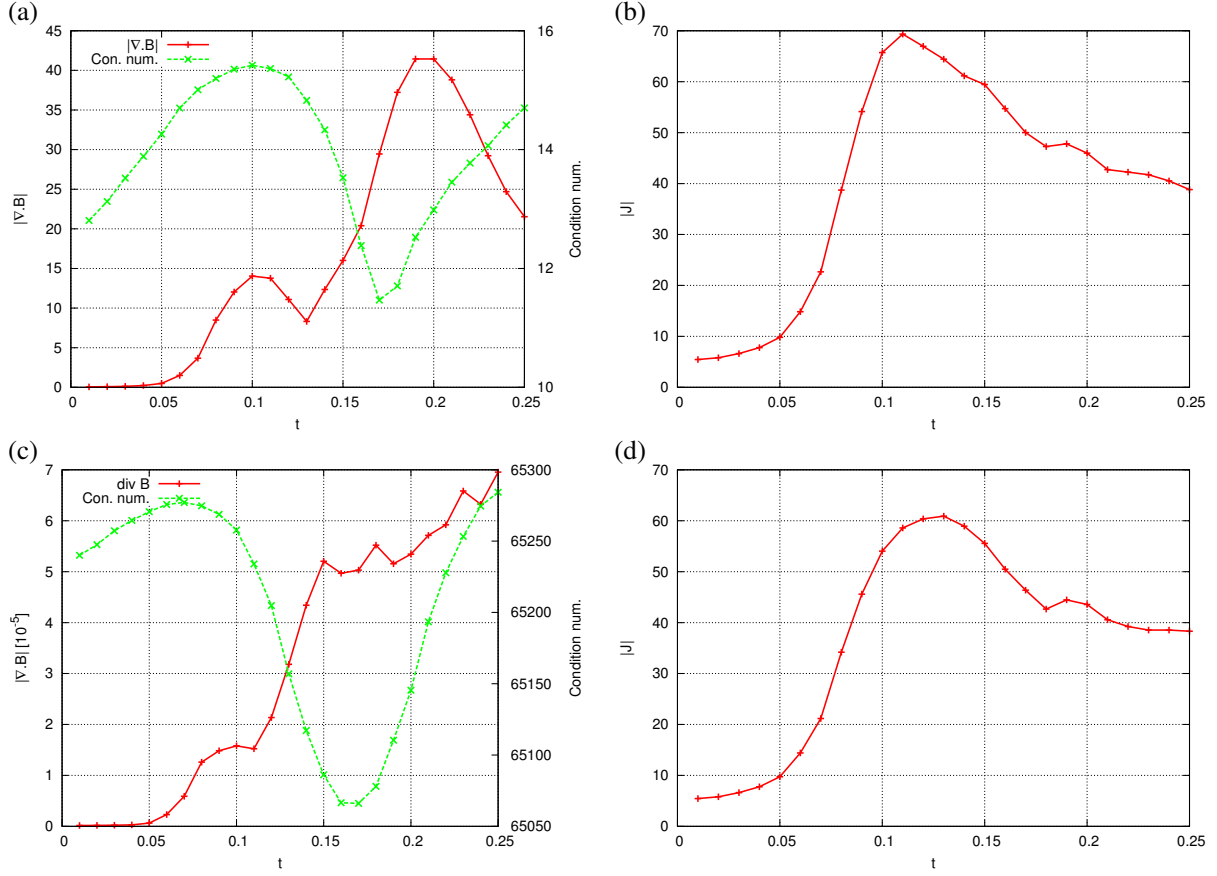


Figure 4.11: Plots (a), (c) show a time evolution of $\nabla \cdot \mathbf{B}$ and condition number of stiffness matrix and plots (b), (d) show the maximum current density. Plots (a), (b) represent solution with divergence equation and plots (a), (b) are without divergence equation. The simulation was performed using a homogeneous mesh consisting of $2 \times 128 \times 128$ triangles.

show a weak dependence of condition number on the current density. The condition number is slightly increasing with the current density. It is caused by higher contribution of magnetic field derivatives into operator. If the current density is high then the derivatives of magnetic fields are also high and, consequently, the terms of divergence equation increase the condition number of stiffness matrix.

The maximum value of the current density, what system reached, was affected by including the solenoidal condition to the system of MHD equations. When the divergence \mathbf{B} condition is involved, then the maximum current density is less about $\sim 10\%$.

The influence of solenoidal condition to the condition number of the stiffness matrix is significant. The condition number increases by three orders of a magnitude when LSSEM includes the additional equation $\nabla \cdot \mathbf{B} = 0$ with the weight $W = 1.0$. Moreover, in this case the condition number depends on the size of the stiffness matrix. The condition numbers are 16×10^3 , 65×10^3 and 262×10^3 for meshes $2 \times 64 \times 64$, $2 \times 128 \times 128$ and $2 \times 256 \times 256$, respectively. The size of matrices is four-times greater when the resolution is doubled. As we can clearly see, the condition number is a linearly dependent on the matrix size. On the other hand, in the case when the solenoidal condition is not involved, the condition number does not increase with a matrix size (stays around 14) i.e. the condition number does not depend on the matrix size.

The iterative solver JCGM takes around 60 iterations when solenoidal condition is not applied. In the opposite case with the divergence \mathbf{B} condition, JCGM takes around 300 iterations

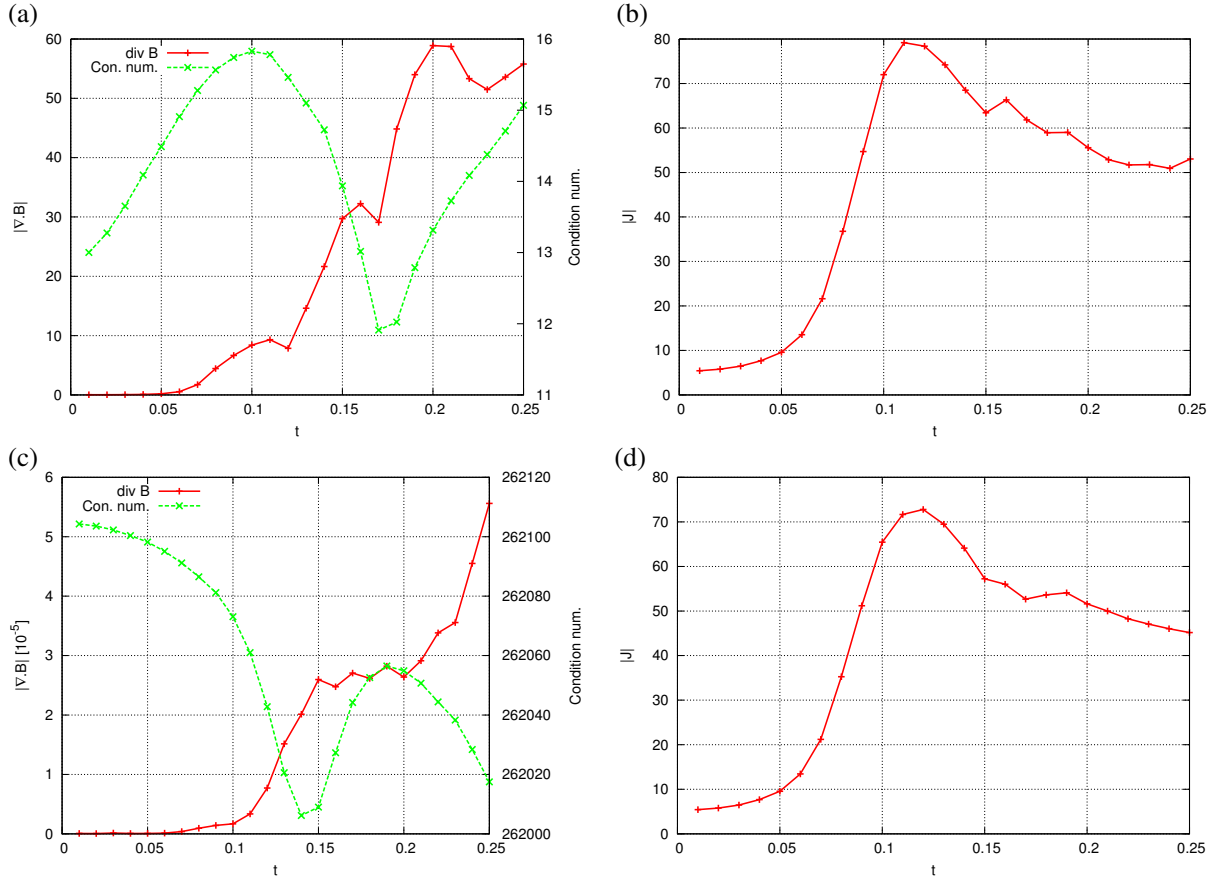


Figure 4.12: Plots (a), (c) show a time evolution of $\nabla \cdot \mathbf{B}$ and condition number of stiffness matrix and plots (b), (d) show the maximum current density. Plots (a), (b) represent solution with divergence equation and plots (a), (b) are without divergence equation. The simulation was performed using a homogeneous mesh consisting of $2 \times 256 \times 256$ triangles.

for $2 \times 64 \times 64$ mesh. For $2 \times 128 \times 128$ mesh is difference even greater: from 60 increases to 430 iterations, approximately.

The figure 4.13 shows dependency of divergence \mathbf{B} and condition number of stiffness matrix on the weight of the solenoidal condition in the MHD equations. The graph shows an inverse relationship between weight and absolute value of divergence of magnetic field (integrated over whole domain). As we expect according to the minimization of residual error of the divergence \mathbf{B} equation, the increasing weight reduces the magnetic charge in the domain. On the other hand, the raising weight significantly increases the condition number of the stiffness matrix and makes it difficult to solve.

The condition number is constant for the weight smaller than 10^{-4} . It is caused by a small contribution of divergence equation to the stiffness matrix. Unfortunately, the condition number steeply grows with the increasing weight, when the weight is greater than 10^{-4} . In these cases, the contribution to the operator matrix of $\nabla \cdot \mathbf{B}$ is significant and it may even override other terms in the operator which leads to the increase of the condition number of the matrix.

4.15 Parallelization

The parallelization is needed when the problem complexity increases and a computational time of a single process is too long. Using Message Passing Interface (MPI) we can run our code on

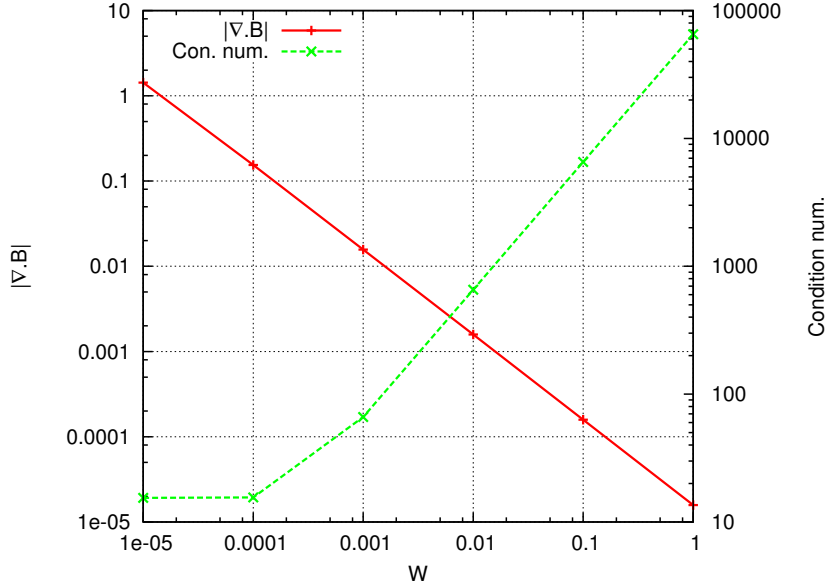


Figure 4.13: The value of $\nabla \cdot \mathbf{B}$ and the condition number of stiffness matrix for various weights W for the solenoidal condition at the time $t = 0.1$. The simulation was performed using a homogeneous mesh consisting of $2 \times 128 \times 128$ triangle elements.

the system with the distributed memory which allows us to run LSFEM on modern machines. The LSFEM requires parallelization of two parts of the code. First is a mesh generation and second is solving of resulting stiffness matrix. The generation of the mesh is quite straightforward. Each process creates its own mesh, only neighboring processes have to construct the same structure of boundary elements and store all boundary nodal indexes into *boundary vector* p_i^k . In other words, the number and positions of boundary nodes must be identical in both neighboring processes. The parallel code synchronizes a time step size and a number of linearization iterations over all MPI processes. The stiffness matrix assembling process is same as for the single processor code. The problem arise when the code reaches the CGM (or JCGM). This method uses matrix-vector and vector-vector operations. At first, let consider that all values corresponding to the boundary nodes of all vectors used in the CGM are *synchronized* (i.e., they have same values in both neighboring processes). The CG (JCG) method consist of a summation vector, a vector multiplication by scalar value and a dot product. The first two operations need no parallelization - the vectors stay synchronized after these operations. Parallelization of dot product vector operation is a quite simple. The each process computes its part of dot product, only boundary values are summed with weight 0.5, then all results are summed over all MPI processes.

The parallelization of matrix-vector multiplication is more complicated. The matrix row corresponding to boundary node is incomplete – it missing contribution from elements from the neighboring MPI domain. The global matrix can be constructed by a summing boundary row over neighboring processes, but it is redundant for computational point of view. The matrix row send through the MPI interface is time expensive operation (because of big volume of data) and, moreover, after matrix-vector multiplication we still need to synchronize resulting vector.

The smarter way to make matrix-vector multiplication parallel is to perform multiplication on each process separately (with local matrix and vector) and then we synchronize resulting vector. The global stiffness matrix can be assembled by

$$\mathbf{S}_{ij} = \sum_k \mathbf{S}_{ij}^k, \quad (4.101)$$

where $k = 1, \dots, N_{proc} - 1$ is a process index and N_{proc} is a total number of processes. The matrix-vector multiplication on each MPI process becomes

$$\mathbf{r}_i^k = \sum_i \sum_j \mathbf{S}_{ij}^k \mathbf{v}_j^k, \quad (4.102)$$

this is a standard matrix product. The vector \mathbf{r}_i^k is not synchronized, i.e. the boundary values are not same on the k -th and $k+1$ -th process. Its boundary values do not contain contribution from matrix of neighboring process $k+1$. The synchronization can be done by following process (coding notation)

$$\mathbf{v}_{p_i^k}^k = \mathbf{v}_{p_i^k}^k + \mathbf{v}_{p_i^{k+1}}^{k+1}, \quad (4.103)$$

then

$$\mathbf{v}_{p_i^{k+1}}^{k+1} = \mathbf{v}_{p_i^k}^k. \quad (4.104)$$

The boundary values are summed over neighboring processes and boundary values are same in both neighboring processes.

4.16 2D Burgers' equation

In this section we derive LSFEM operator for simple Burgers' equation. We chose Burgers' equation because it contain nonlinearity and it is still simple. Burgers' equation is usually used like a standard nonlinear test equation. In this case we use an analytic integration instead of numeric integration by Gaussian quadrature. It is possible because we use only first order of basis functions and the Burgers' equation has only simple nonlinearity. Using a higher order of basis functions and/or higher nonlinearity is, in principle, possible for the analytical integration, but it is more complicated. The Burgers' equations reads

$$\frac{\partial \mathbf{v}}{\partial t} + \mathbf{v} \cdot \nabla \mathbf{v} = 0. \quad (4.105)$$

The partial differential equations in the matrix form are following

$$\begin{pmatrix} \frac{\partial}{\partial t} + v_x \frac{\partial}{\partial x} + v_y \frac{\partial}{\partial y} & 0 \\ 0 & \frac{\partial}{\partial t} + v_x \frac{\partial}{\partial x} + v_y \frac{\partial}{\partial y} \end{pmatrix} \begin{pmatrix} v_x \\ v_y \end{pmatrix} = \begin{pmatrix} 0 \\ 0 \end{pmatrix}. \quad (4.106)$$

Now we transform first equation of (4.106) "step by step" into form suitable for LSFEM as an example. The derivation of second equation is analogical and we will not explicitly show it here. At the first, we discretize time derivative by Crang-Nicolson scheme (also we can use general θ -scheme as in the section 4.9)

$$\frac{v_x - \bar{v}_x}{\Delta t} + \frac{1}{2} \left(v_x \frac{\partial v_x}{\partial x} + \bar{v}_x \frac{\partial \bar{v}_x}{\partial x} + v_y \frac{\partial v_x}{\partial y} + \bar{v}_y \frac{\partial \bar{v}_x}{\partial y} \right) = 0, \quad (4.107)$$

where variables at an old time step are denoted by over-line. We move the terms at the old time step to right hand side and obtain

$$v_x + \frac{\Delta t}{2} \left(v_x \frac{\partial v_x}{\partial x} + v_y \frac{\partial v_x}{\partial y} \right) = \bar{v}_x - \frac{\Delta t}{2} \left(\bar{v}_x \frac{\partial \bar{v}_x}{\partial x} + \bar{v}_y \frac{\partial \bar{v}_x}{\partial y} \right). \quad (4.108)$$

The terms in the parentheses in equations (4.108) are nonlinear. The terms on the RHS can stay in the non-linear form because they are known and they can be evaluated from the old time step or previous Newton's iteration. The Newton iterative method is used to transform

operator to a linear form:

$$\begin{aligned} v_x^{k+1} + \frac{\Delta t}{2} \left(v_x^k \frac{\partial v_x^{k+1}}{\partial x} + v_x^{k+1} \frac{\partial v_x^k}{\partial x} + v_y^k \frac{\partial v_x^{k+1}}{\partial y} + v_y^{k+1} \frac{\partial v_x^k}{\partial y} \right) \\ = \bar{v}_x + \frac{\Delta t}{2} \left(v_x^k \frac{\partial v_x^k}{\partial x} + v_y^k \frac{\partial v_x^k}{\partial y} - \bar{v}_x \frac{\partial \bar{v}_x}{\partial x} - \bar{v}_y \frac{\partial \bar{v}_x}{\partial y} \right). \end{aligned} \quad (4.109)$$

The first row of the left hand side operator is

$$\left(1 + \frac{\Delta t}{2} \left(v_x^k \frac{\partial}{\partial x} + \frac{\partial v_x^k}{\partial x} + v_y^k \frac{\partial}{\partial y} \right), \frac{\Delta t}{2} \frac{\partial v_x^k}{\partial y} \right). \quad (4.110)$$

This operator (4.110) is a linearized matrix operator of partial differential equations (4.106). We can derive a second equation of (4.106) by the same way as equation (4.110) and obtain the complete operator:

$$\begin{pmatrix} 1 + \frac{\Delta t}{2} \left(v_x^k \frac{\partial}{\partial x} + \frac{\partial v_x^k}{\partial x} + v_y^k \frac{\partial}{\partial y} \right) & \frac{\Delta t}{2} \frac{\partial v_x^k}{\partial y} \\ \frac{\Delta t}{2} \frac{\partial v_y^k}{\partial x} & 1 + \frac{\Delta t}{2} \left(v_x^k \frac{\partial}{\partial x} + \frac{\partial v_y^k}{\partial y} + v_y^k \frac{\partial}{\partial y} \right) \end{pmatrix}. \quad (4.111)$$

The corresponding RHS vector is

$$\begin{pmatrix} \bar{v}_x + \frac{\Delta t}{2} \left(v_x^k \frac{\partial v_x^k}{\partial x} + v_y^k \frac{\partial v_x^k}{\partial y} - \bar{v}_x \frac{\partial \bar{v}_x}{\partial x} - \bar{v}_y \frac{\partial \bar{v}_x}{\partial y} \right) \\ \bar{v}_y + \frac{\Delta t}{2} \left(v_x^k \frac{\partial v_y^k}{\partial x} + v_y^k \frac{\partial v_y^k}{\partial y} - \bar{v}_x \frac{\partial \bar{v}_y}{\partial x} - \bar{v}_y \frac{\partial \bar{v}_y}{\partial y} \right) \end{pmatrix}. \quad (4.112)$$

According to the equation (4.9) we apply the operator (4.111) on first order basis functions $\phi_m = l_m$ (where $m = 1, 2, 3$) then resulting matrix yields

$$\begin{pmatrix} \sum_{i=1}^3 q_{1,i} l_i & \sum_{i=1}^3 q_{2,i} l_i \\ \sum_{i=1}^3 q_{3,i} l_i & \sum_{i=1}^3 q_{4,i} l_i \end{pmatrix}, \quad (4.113)$$

where each element of the matrix is exactly described by a general first order shape function. First order shape functions have three coefficients and it gives us $3 \times 4 = 12$ a total number of coefficients for the operator. The coefficients in the second matrix (obtained by applying operator on $\phi_n = l_n$) we denote $r_{j,i}$. The RHS vector \mathbf{R} we can write in the following notation

$$\begin{pmatrix} \sum_{i=1}^3 s_{1,i} l_i \\ \sum_{i=1}^3 s_{2,i} l_i \end{pmatrix}. \quad (4.114)$$

According to the least-squares principle (4.9) we multiple matrices $q_{j,i}$ and $r_{j,i}$ (where matrices $q_{j,i}$ and $r_{j,i}$ correspond to terms $\mathcal{A}\Phi_i$ and $\mathcal{A}\Phi_j$ in Eq. (4.9), respectively) and integrate them over an element domain $\Omega_e = [(0, 1) \times (0, 1)]$ i.e. over l_1, l_2 with substitution $l_3 = 1 - l_1 - l_2$. The first row of sub-matrix is

$$\frac{1}{24} \begin{pmatrix} (\sum (q_{1,i} r_{1,i} + q_{3,i} r_{3,i}) + \sum q_{1,i} \sum r_{1,i} + \sum q_{3,i} \sum r_{3,i}), \\ (\sum (q_{2,i} r_{1,i} + q_{4,i} r_{3,i}) + \sum q_{2,i} \sum r_{1,i} + \sum q_{4,i} \sum r_{3,i}) \end{pmatrix} \quad (4.115)$$

and then the second row of sub-matrix is

$$\frac{1}{24} \begin{pmatrix} (\sum q_{1,i} r_{2,i} + \sum q_{1,i} \sum r_{2,i} + \sum q_{3,i} r_{4,i} + \sum q_{3,i} \sum r_{4,i}), \\ (\sum q_{2,i} r_{4,i} + \sum q_{2,i} \sum r_{4,i} + \sum q_{4,i} r_{4,i} + \sum q_{4,i} \sum r_{4,i}) \end{pmatrix}. \quad (4.116)$$

The load sub-vector reads

$$\frac{1}{24} \begin{pmatrix} \sum (s_{1,i}q_{2,i} + s_{2,i}q_{4,i}) + \sum s_{1,i} \sum q_{2,i} + \sum s_{2,i} \sum q_{4,i} \\ \sum (s_{1,i}q_{1,i} + s_{2,i}q_{3,i}) + \sum s_{1,i} \sum q_{1,i} + \sum s_{2,i} \sum q_{3,i} \end{pmatrix}. \quad (4.117)$$

The last task is to determine coefficients $q_{j,i}$, $r_{j,i}$ and $s_{j,i}$. Values of these coefficients can be extracted from the operator matrix (4.111). Let consider velocities v_x and v_y in the form

$$\begin{aligned} v_x &= \sum v_{x,i} l_i, \\ v_y &= \sum v_{y,i} l_i, \end{aligned} \quad (4.118)$$

velocities are approximated by the linear shape functions on the element domain. Inserting relation (4.118) into the operator (4.111) we get (again, only first row of the matrix is presented here as an example)

$$\left(1 + \frac{\Delta t}{2} \left(\sum v_{x,i}^k l_i \frac{\partial}{\partial x} + \sum \frac{\partial v_{x,i}^k l_i}{\partial x} + \sum v_{y,i}^k l_i \frac{\partial}{\partial y} \right), \frac{\Delta t}{2} \sum \frac{\partial v_{x,i}^k l_i}{\partial y} \right). \quad (4.119)$$

Applying this operator to l_m and using rule for derivation (4.48) we get

$$\left(l_m + \frac{\Delta t}{2} \left(b_m \sum v_{x,i}^k l_i + l_m \sum b_i v_{x,i}^k + c_m \sum v_{y,i}^k l_i \right), \frac{\Delta t}{2} l_m \sum c_i v_{x,i}^k \right). \quad (4.120)$$

Extracting parts which contains l_i then we obtain coefficients

$$\begin{aligned} q_{1,i} &= \delta_{im} \left(1 + \frac{\Delta t}{2} \sum b_i v_{x,i}^k \right) + \frac{\Delta t}{2} \left(b_m v_{x,i}^k + c_m v_{y,i}^k \right), \\ q_{2,i} &= \delta_{im} \frac{\Delta t}{2} \sum c_i v_{x,i}^k. \end{aligned} \quad (4.121)$$

For the second operator row we similarly write

$$\begin{aligned} q_{3,i} &= \delta_{im} \frac{\Delta t}{2} \sum b_i v_{y,i}^k, \\ q_{4,i} &= \delta_{im} \left(1 + \frac{\Delta t}{2} \sum c_i v_{y,i}^k \right) + \frac{\Delta t}{2} \left(b_m v_{x,i}^k + c_m v_{y,i}^k \right). \end{aligned} \quad (4.122)$$

Coefficients $r_{j,i}$ are same as $q_{j,i}$ but instead index m the index n is used – operator was applied to l_n . The last remaining thing what we need to do is to determine coefficients $s_{1,i}$ and $s_{2,i}$ of RHS

$$\begin{aligned} s_{1,i} &= \bar{v}_x + \frac{\Delta t}{2} \left(v_{x,i}^k \sum b_i v_{x,i}^k - \bar{v}_{x,i} \sum b_i \bar{v}_{x,i} + v_{y,i}^k \sum c_i v_{x,i}^k - \bar{v}_{y,i} \sum c_i \bar{v}_{x,i} \right), \\ s_{2,i} &= \bar{v}_y + \frac{\Delta t}{2} \left(v_{y,i}^k \sum c_i v_{y,i}^k - \bar{v}_{y,i} \sum c_i \bar{v}_{y,i} + v_{x,i}^k \sum b_i v_{y,i}^k - \bar{v}_{x,i} \sum b_i \bar{v}_{y,i} \right). \end{aligned}$$

This method with analytic integration can be easily used only in the case of low order shape functions and when the operator has only low order of nonlinearity. In the case of more complex problem the number of required coefficients steeply grows. For example, consider the second order of shape functions in the case of Burgers' equations. The second order shape function is described by six coefficients. Then we need $6 \times 4 = 24$ coefficients for matrix operator. In the case of a higher nonlinearity of operator is the situation even worse. When equations contain term v_x^3 we generally need $3 \times 3 \times 4 = 27$ coefficients for first order shape functions.

The method with analytic integration is several times faster than method with the numeri-

cal integration but this method also has limitations in the usability due to coefficient description of operators which becomes very complicated, when we require the higher order of shape function and/or we have a higher nonlinearity in PDE.

Here, we present the numeric solution of Burgers' problem by LSFEM with analytical integration described above. The simulation box is set to $< -0.5, 0.5 > \times < -0.5, 0.5 >$. The domain is divided into homogeneous mesh with $2 \times 256 \times 256 = 131072$ elements. The first order shape functions are mapped on the element. Courant constant is set to 0.5 and $\theta = 0.75$ for smoothing shock edges and prevent oscillations. Initial conditions are set by following radial symmetric velocity field

$$\begin{aligned} r &= \sqrt{x^2 + y^2} \\ \text{if } (r < 0.2 \text{ and } r \neq 0) \text{ then} \\ v_x &= x/r \\ v_y &= y/r \\ \text{else} \\ \mathbf{v} &= 0 \end{aligned}$$

The results of simulations are presented in figures 4.14 and 4.15. The figures display velocity magnitude at three times $t = 0.1$, $t = 0.2$ and $t = 0.4$. Also graphs of velocity profiles are plotted in the figure 4.14b.

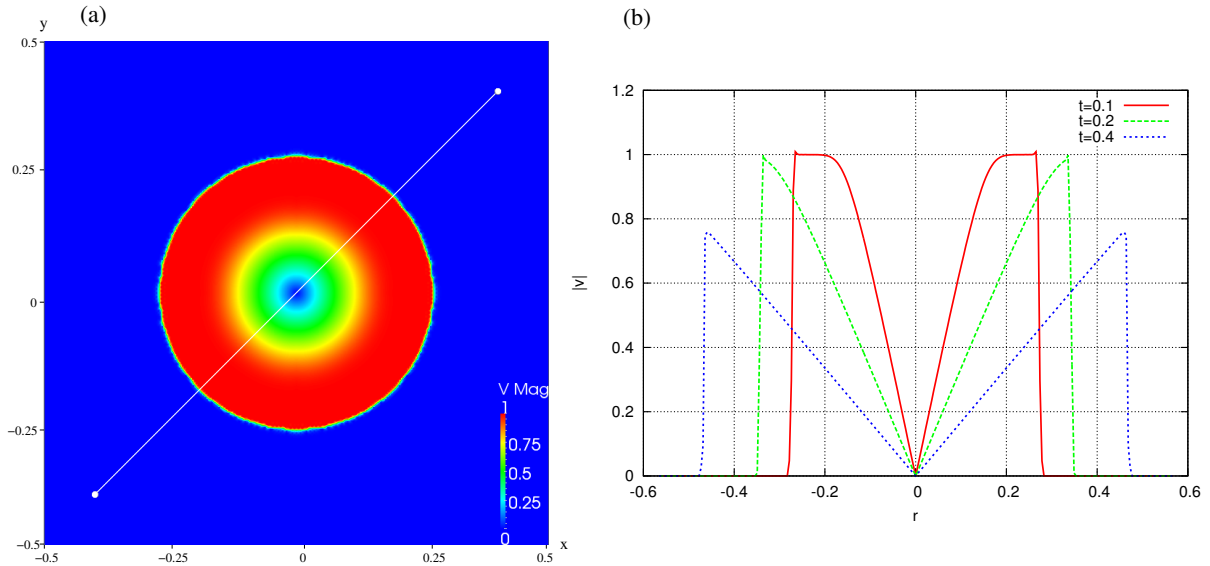


Figure 4.14: The solution of Burgers' equation by the LSFEM. The left panel (a): the magnitude of velocity is displayed in the color scale for the time $t = 0.10$, where the white line denotes the measuring profile of panel (b). The right panel (b): the velocity profiles are plotted for times $t = 0.10$, $t = 0.20$ and $t = 0.40$.

4.17 3D Burgers' equation

In this section we present derivation of LSFEM with analytical integration for 3D Burger's equation. The 3D equation of Burgers' problem has following form

$$\frac{\partial \mathbf{v}}{\partial t} + \mathbf{v} \cdot \nabla \mathbf{v} = 0. \quad (4.123)$$

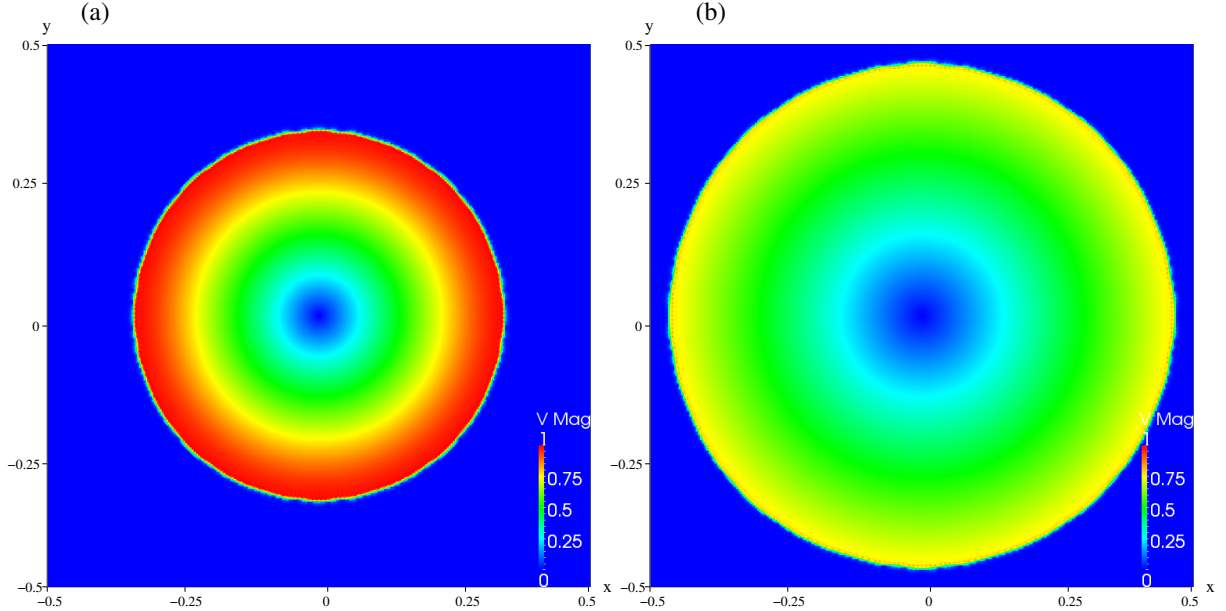


Figure 4.15: Solution of Burgers' equation by the LSFEM. (a) the velocity magnitude at time $t = 0.2$ and (b) the velocity magnitude at time $t = 0.4$.

The derivation of time discretized and linearized form is analogical to 2D case. The first row of operator matrix reads

$$\left(1 + \theta \Delta t \left(v_x^k \frac{\partial}{\partial x} + \frac{\partial v_x^k}{\partial x} + v_y^k \frac{\partial}{\partial y} + v_z^k \frac{\partial}{\partial z} \right), \theta \Delta t \frac{\partial v_x^k}{\partial y}, \theta \Delta t \frac{\partial v_x^k}{\partial z} \right), \quad (4.124)$$

second row is

$$\left(\theta \Delta t \frac{\partial v_x^k}{\partial x}, 1 + \theta \Delta t \left(v_x^k \frac{\partial}{\partial x} + v_y^k \frac{\partial}{\partial y} + \frac{\partial v_y^k}{\partial y} + v_z^k \frac{\partial}{\partial z} \right), \theta \Delta t \frac{\partial v_x^k}{\partial z} \right) \quad (4.125)$$

and third row

$$\left(\theta \Delta t \frac{\partial v_x^k}{\partial y}, \theta \Delta t \frac{\partial v_x^k}{\partial z}, 1 + \theta \Delta t \left(v_x^k \frac{\partial}{\partial x} + v_y^k \frac{\partial}{\partial y} + v_z^k \frac{\partial}{\partial z} + \frac{\partial v_z^k}{\partial z} \right) \right). \quad (4.126)$$

The RHS vector has following form

$$\begin{pmatrix} \bar{v}_x + \theta \Delta t \left(v_x^k \frac{\partial v_x^k}{\partial x} + v_y^k \frac{\partial v_x^k}{\partial y} + v_z^k \frac{\partial v_x^k}{\partial z} \right) - (1 - \theta) \Delta t \left(\bar{v}_x \frac{\partial \bar{v}_x}{\partial x} + \bar{v}_y \frac{\partial \bar{v}_x}{\partial y} + \bar{v}_z \frac{\partial \bar{v}_x}{\partial z} \right) \\ \bar{v}_y + \theta \Delta t \left(v_x^k \frac{\partial v_y^k}{\partial x} + v_y^k \frac{\partial v_y^k}{\partial y} + v_z^k \frac{\partial v_y^k}{\partial z} \right) - (1 - \theta) \Delta t \left(\bar{v}_x \frac{\partial \bar{v}_y}{\partial x} + \bar{v}_y \frac{\partial \bar{v}_y}{\partial y} + \bar{v}_z \frac{\partial \bar{v}_y}{\partial z} \right) \\ \bar{v}_z + \theta \Delta t \left(v_x^k \frac{\partial v_z^k}{\partial x} + v_y^k \frac{\partial v_z^k}{\partial y} + v_z^k \frac{\partial v_z^k}{\partial z} \right) - (1 - \theta) \Delta t \left(\bar{v}_x \frac{\partial \bar{v}_z}{\partial x} + \bar{v}_y \frac{\partial \bar{v}_z}{\partial y} + \bar{v}_z \frac{\partial \bar{v}_z}{\partial z} \right) \end{pmatrix}, \quad (4.127)$$

where θ -scheme for the time discretization is used. The derivation of coefficients $q_{j,i}$ and $r_{j,i}$ is similar to derivation in the 2D Burger's equation. The operator matrix is considered in the form

$$\begin{pmatrix} \sum_{i=1}^4 q_{1,i} l_i & \sum_{i=1}^4 q_{2,i} l_i & \sum_{i=1}^4 q_{3,i} l_i \\ \sum_{i=1}^4 q_{4,i} l_i & \sum_{i=1}^4 q_{5,i} l_i & \sum_{i=1}^4 q_{6,i} l_i \\ \sum_{i=1}^4 q_{7,i} l_i & \sum_{i=1}^4 q_{8,i} l_i & \sum_{i=1}^4 q_{9,i} l_i \end{pmatrix} \quad (4.128)$$

and RHS vector

$$\begin{pmatrix} \sum_{i=1}^4 s_{1,i} l_i \\ \sum_{i=1}^4 s_{2,i} l_i \\ \sum_{i=1}^4 s_{3,i} l_i \end{pmatrix}. \quad (4.129)$$

From the operator matrix (4.124),(4.125),(4.126) and RHS vector (4.127) we get coefficients $q_{j,i}$

$$\begin{aligned} q_{1,i} &= \delta_{im} \left(1 + \theta \Delta t \sum b_i v_{x,i}^k \right) + \theta \Delta t \left(b_m v_{x,i}^k + c_m v_{y,i}^k + c_m v_{z,i}^k \right), \\ q_{2,i} &= \delta_{im} \theta \Delta t \sum c_i v_{x,i}^k, \\ q_{3,i} &= \delta_{im} \theta \Delta t \sum d_i v_{x,i}^k, \\ q_{4,i} &= \delta_{im} \theta \Delta t \sum b_i v_{y,i}^k, \\ q_{5,i} &= \delta_{im} \left(1 + \theta \Delta t \sum c_i v_{y,i}^k \right) + \theta \Delta t \left(b_m v_{x,i}^k + c_m v_{y,i}^k + c_m v_{z,i}^k \right), \\ q_{6,i} &= \delta_{im} \theta \Delta t \sum d_i v_{y,i}^k, \\ q_{7,i} &= \delta_{im} \theta \Delta t \sum b_i v_{z,i}^k, \\ q_{8,i} &= \delta_{im} \theta \Delta t \sum c_i v_{z,i}^k, \\ q_{9,i} &= \delta_{im} \left(1 + \theta \Delta t \sum d_i v_{z,i}^k \right) + \theta \Delta t \left(b_m v_{x,i}^k + c_m v_{y,i}^k + c_m v_{z,i}^k \right) \end{aligned} \quad (4.130)$$

and RHS vector coefficients $s_{j,i}$

$$\begin{aligned} s_{1,i} &= \bar{v}_x + \theta \Delta t \left(v_{x,i}^k \sum b_i v_{x,i}^k + v_{y,i}^k \sum c_i v_{x,i}^k + v_{z,i}^k \sum d_i v_{x,i}^k \right) - \\ &\quad - (1 - \theta) \Delta t \left(\bar{v}_{x,i} \sum b_i \bar{v}_{x,i} + \bar{v}_{y,i} \sum c_i \bar{v}_{x,i} + \bar{v}_{z,i} \sum d_i \bar{v}_{x,i} \right), \\ s_{2,i} &= \bar{v}_y + \theta \Delta t \left(v_{x,i}^k \sum b_i v_{y,i}^k + v_{y,i}^k \sum c_i v_{y,i}^k + v_{z,i}^k \sum d_i v_{y,i}^k \right) - \\ &\quad - (1 - \theta) \Delta t \left(\bar{v}_{x,i} \sum b_i \bar{v}_{y,i} + \bar{v}_{y,i} \sum c_i \bar{v}_{y,i} + \bar{v}_{z,i} \sum d_i \bar{v}_{y,i} \right), \\ s_{3,i} &= \bar{v}_z + \theta \Delta t \left(v_{x,i}^k \sum b_i v_{z,i}^k + v_{y,i}^k \sum c_i v_{z,i}^k + v_{z,i}^k \sum d_i v_{z,i}^k \right) - \\ &\quad - (1 - \theta) \Delta t \left(\bar{v}_{x,i} \sum b_i \bar{v}_{z,i} + \bar{v}_{y,i} \sum c_i \bar{v}_{z,i} + \bar{v}_{z,i} \sum d_i \bar{v}_{z,i} \right). \end{aligned} \quad (4.131)$$

According to the equation (4.9) we integrate multiplied matrices $q_{j,i}$ and $r_{j,i}$ (by the same way like $q_{j,i}$, but we applied it to different basis function ϕ). The resulting first row of sub-matrix is

$$\frac{1}{120} \begin{pmatrix} (\sum (q_{1,i} r_{1,i} + q_{4,i} r_{4,i} + q_{7,i} r_{7,i}) + \sum q_{1,i} \sum r_{1,i} + \sum q_{4,i} \sum r_{4,i} + \sum q_{7,i} \sum r_{7,i}), \\ (\sum (q_{2,i} r_{1,i} + q_{5,i} r_{4,i} + q_{8,i} r_{7,i}) + \sum q_{2,i} \sum r_{1,i} + \sum q_{5,i} \sum r_{4,i} + \sum q_{8,i} \sum r_{7,i}), \\ (\sum (q_{3,i} r_{1,i} + q_{6,i} r_{4,i} + q_{9,i} r_{7,i}) + \sum q_{3,i} \sum r_{1,i} + \sum q_{6,i} \sum r_{4,i} + \sum q_{9,i} \sum r_{7,i}) \end{pmatrix}, \quad (4.132)$$

second row is

$$\frac{1}{120} \begin{pmatrix} (\sum (q_{1,i} r_{2,i} + q_{4,i} r_{5,i} + q_{7,i} r_{8,i}) + \sum q_{1,i} \sum r_{2,i} + \sum q_{4,i} \sum r_{5,i} + \sum q_{7,i} \sum r_{8,i}), \\ (\sum (q_{2,i} r_{2,i} + q_{5,i} r_{5,i} + q_{8,i} r_{8,i}) + \sum q_{2,i} \sum r_{2,i} + \sum q_{5,i} \sum r_{5,i} + \sum q_{8,i} \sum r_{8,i}), \\ (\sum (q_{3,i} r_{2,i} + q_{6,i} r_{5,i} + q_{9,i} r_{8,i}) + \sum q_{3,i} \sum r_{2,i} + \sum q_{6,i} \sum r_{5,i} + \sum q_{9,i} \sum r_{8,i}) \end{pmatrix} \quad (4.133)$$

and finally third row is

$$\frac{1}{120} \begin{pmatrix} (\sum (q_{1,i}r_{3,i} + q_{4,i}r_{6,i} + q_{7,i}r_{9,i}) + \sum q_{1,i} \sum r_{3,i} + \sum q_{4,i} \sum r_{6,i} + \sum q_{7,i} \sum r_{9,i}), \\ (\sum (q_{2,i}r_{3,i} + q_{5,i}r_{6,i} + q_{8,i}r_{9,i}) + \sum q_{2,i} \sum r_{3,i} + \sum q_{5,i} \sum r_{6,i} + \sum q_{8,i} \sum r_{9,i}), \\ (\sum (q_{3,i}r_{3,i} + q_{6,i}r_{6,i} + q_{9,i}r_{9,i}) + \sum q_{3,i} \sum r_{3,i} + \sum q_{6,i} \sum r_{6,i} + \sum q_{9,i} \sum r_{9,i}) \end{pmatrix}. \quad (4.134)$$

The integrated RHS sub-vector is

$$\frac{1}{120} \begin{pmatrix} \sum (s_{1,i}q_{1,i} + s_{2,i}q_{4,i} + s_{3,i}q_{7,i}) + \sum s_{1,i} \sum q_{1,i} + \sum s_{2,i} \sum q_{4,i} + \sum s_{3,i} \sum q_{7,i}, \\ \sum (s_{1,i}q_{2,i} + s_{2,i}q_{5,i} + s_{3,i}q_{8,i}) + \sum s_{1,i} \sum q_{2,i} + \sum s_{2,i} \sum q_{5,i} + \sum s_{3,i} \sum q_{8,i}, \\ \sum (s_{1,i}q_{3,i} + s_{2,i}q_{6,i} + s_{3,i}q_{9,i}) + \sum s_{1,i} \sum q_{3,i} + \sum s_{2,i} \sum q_{6,i} + \sum s_{3,i} \sum q_{9,i} \end{pmatrix}. \quad (4.135)$$

in following part, the 3D Burgers' problem is numerically solved by LSFEM with analytical integration described above and the results are presented. The simulation box is set to $< -0.5, 0.5 > \times < -0.5, 0.5 > \times < -0.5, 0.5 >$. The domain is divided into homogeneous mesh with $6 \times 64 \times 64 \times 64 = 1572864$ tetrahedral elements. The relatively small resolution of simulation is used because the 3D LSFEM code is not parallel. The first order shape functions are mapped on the elements. Courant constant is set to 0.5 and $\theta = 0.6$ for smoothing shock edges and prevent oscillations. Initial conditions are set by following radial symmetric velocity field

$$\begin{aligned} r &= \sqrt{x^2 + y^2 + z^2} \\ \text{if } (r < 0.2 \text{ and } r \neq 0) \text{ then} \\ v_x &= x/r \\ v_y &= y/r \\ v_z &= z/r \\ \text{else} \\ \mathbf{v} &= 0 \end{aligned}$$

The results of simulations are presented in the figures 4.16 and 4.17. The figures display velocity magnitude at four times $t = 0.0$, $t = 0.1$, $t = 0.2$ and $t = 0.4$. Also graphs of velocity profiles are plotted in the figure 4.14b. The solution contains strong numeric oscillations because the mesh resolution is very coarse. The LSFEM solution with sufficiently high resolution has small or no oscillations (it also depends on the parameter θ) as we can see in the former section 4.16. Unfortunately, it is not possible to use same high resolution as in 2D case because 3D LSFEM code requires more computer resources.

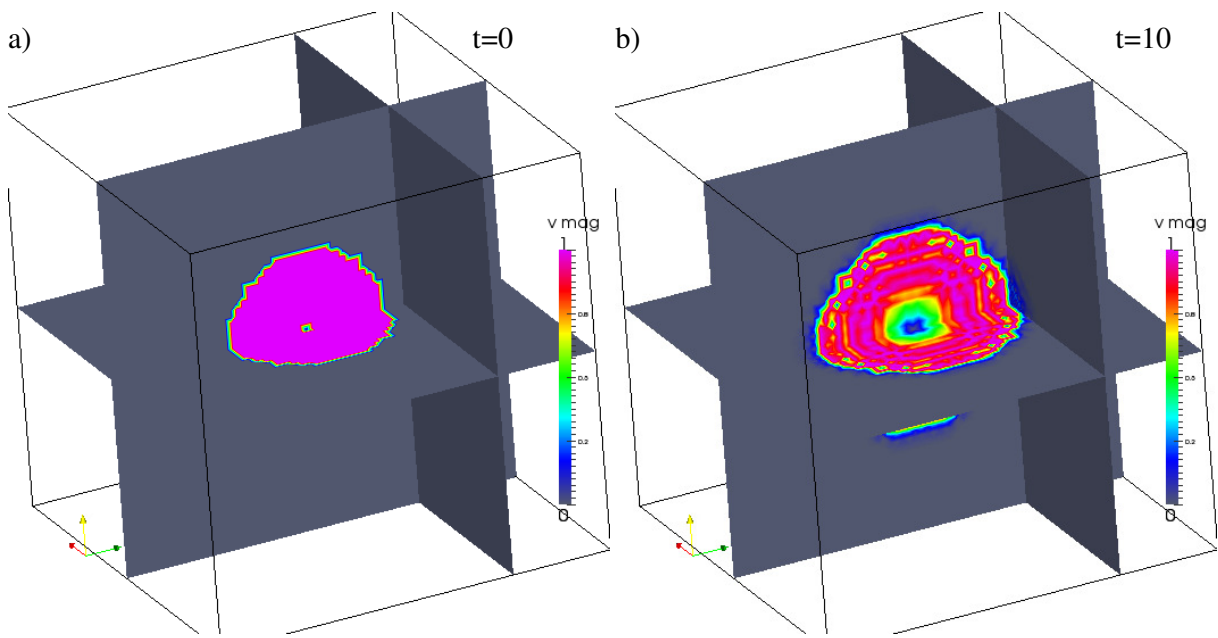


Figure 4.16: The solution of Burgers' equation by the LSFEM. (a) the magnitude of velocity is displayed in the color scale for the time $t = 0.0$ and (b) the velocity magnitude at time $t = 0.1$.

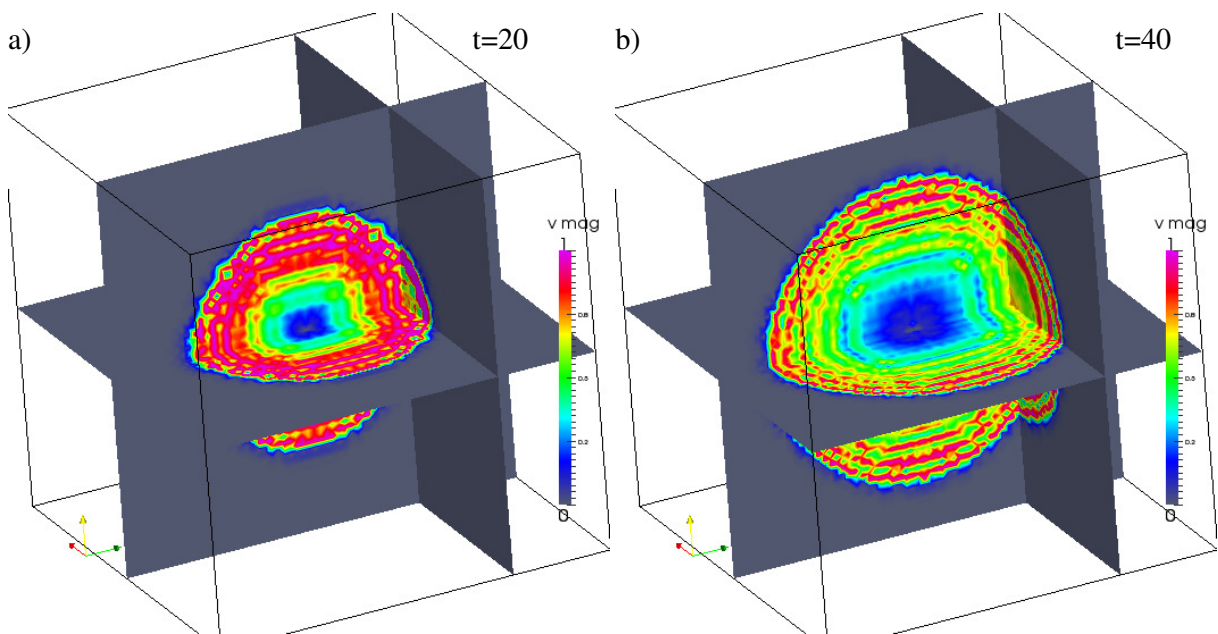


Figure 4.17: Solution of Burgers' equation by the LSFEM. (a) the velocity magnitude at time $t = 0.2$ and (b) the velocity magnitude at time $t = 0.4$.

Chapter 5

Results

In order to asses usability and properties of LSFEM MHD solver we perform several tests on standardized ideal (non-resistive) and resistive MHD problems. In all test we use adiabatic index $\gamma = 5/3$, implicitness parameter $\theta = 0.5$ (Crank-Nicholson time discretization), and the Courant constant 0.6.

5.1 Ryu-Jones ideal MHD test

First, we have applied our code onto the standard Ryu-Jones ideal MHD 1D shock/discontinuity problem (Ryu and Jones, 1995). They used ideal MHD equations and second order explicit finite difference scheme (Total Variation Diminishing) and the nonlinear Riemann solver.

The initial state is given by prescriptions $(\rho, v_x, v_y, v_z, B_x, B_y, B_z, E) = (1, -1, 0, 0, 0, 1, 5, 1)$ in the left half, and $(\rho, v_x, v_y, v_z, B_x, B_y, B_z, E) = (1, 1, 0, 0, 0, 1, 5, 0)$ in the right half of computational box, respectively. Domain $(-0.5, 0.5)$ was divided into 512 elements. We use first order basis functions for approximate FEM solution. Boundary conditions on both ends are of von Neumann type. The Fig. 5.1 shows density ρ and magnetic field B_y profile in the panel a) and velocity profile v_x in the panel b) at time $t = 0.1$. The profiles closely correspond to the profiles presented in Ryu and Jones (1995). The only difference is located in the middle of the domain where LSFEM generate small spurious oscillation.

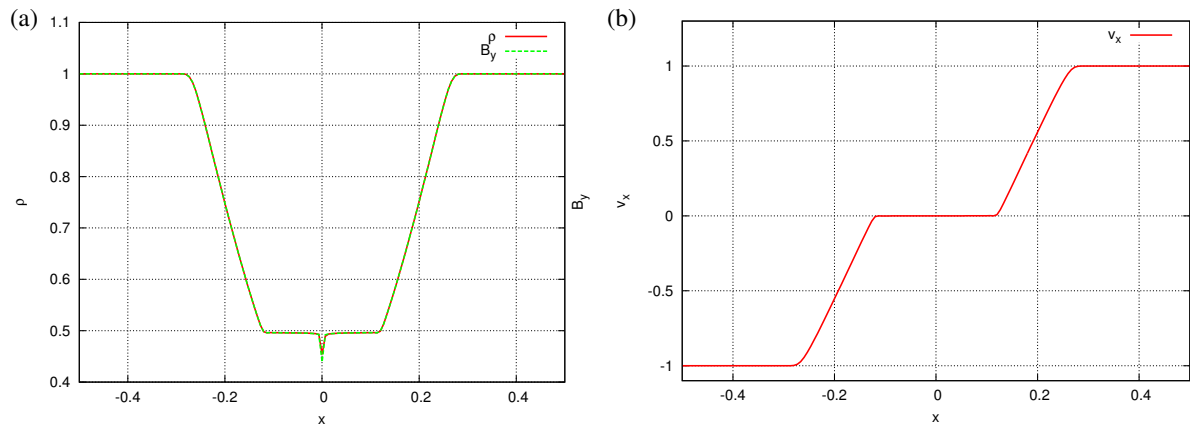


Figure 5.1: The LSFEM solution of MHD shock tube test at time $t = 0.1$. The first order basis functions were used for approximation of solution. The left graph (a) contains density profile (red dashed line) and B_y profile along x axis. The right graph (b) visualizes velocity v_x profile along x axis.

In order to study influence of basis-function order on the approximate solution we calculate the same test problem, now with the second-order Lagrange polynomials. All other parameters are the same as in the previous case displayed in Fig. 5.1. The profiles of ρ , B_y and v_x are shown in Fig. 5.2. As we can see the middle oscillation is even greater when the second order polynomials are used.

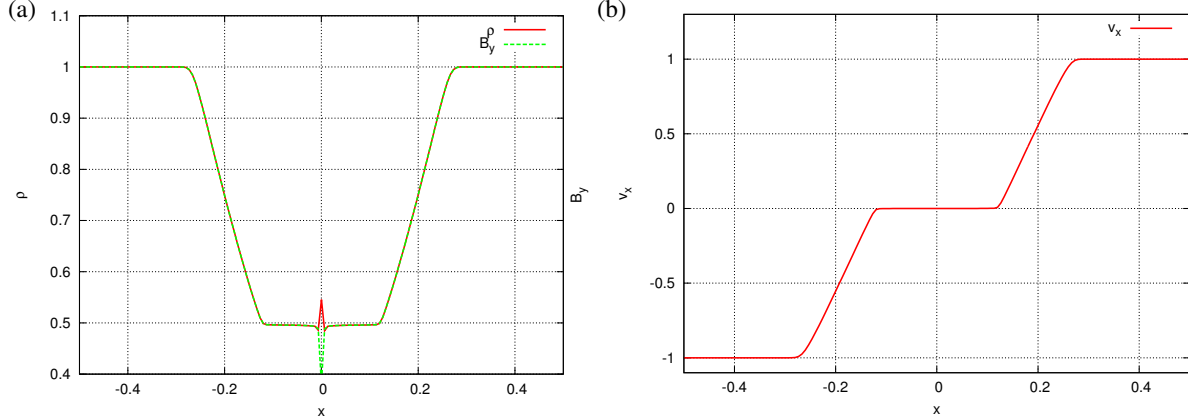


Figure 5.2: The LSFEM solution of MHD shock tube test at time $t = 0.1$. The second order basis functions were used for approximation of solution. The left graph (a) contains density profile (red dashed line) and B_y profile along x axis. The right graph (b) visualizes velocity v_x profile along x axis.

The LSFEM solution is overall in good agreement with the reference solution of Ryu and Jones (1995). Only small oscillations are located at the points where the first derivative of an analytical solution does not exist.

5.2 Tang-Orszag ideal MHD test

As a next test, we have performed standard Orszag-Tang 2D ideal-MHD vortex problem (Orszag and Tang, 1979). The test starts with an initially periodic velocity and magnetic fields, a constant mass density, and a pressure distribution given by

$$\begin{aligned} \rho &= \gamma p, \\ \pi_x &= -\sin(2\pi y), \quad \pi_y = \sin(2\pi x), \\ B_x &= -\frac{1}{\sqrt{4\pi}} \sin(2\pi y), \quad B_y = \frac{1}{\sqrt{4\pi}} \sin(4\pi x), \\ p &= \gamma \frac{1}{4\pi}. \end{aligned}$$

The computational domain 1.0×1.0 was discretized by $2 \times 640 \times 640$ triangular elements. We apply periodic boundary conditions at all boundaries. The first-order basis functions were used in this simulation. Results in Figs. 5.3 and 5.4 show plasma density and magnitude of magnetic field, respectively, at times $t = 0.25$ (a), and $t = 0.50$ (b).

LSFEM revealed the same results for vortices of Orszag and Tang (1979) as obtained by Ryu et al. (1995) and by Dai and Woodward (1998). Gradients are well resolved by one element. Small numerical oscillations are located around formed shocks due to fact that discretized equations can not hold infinity derivatives in the shock elements.

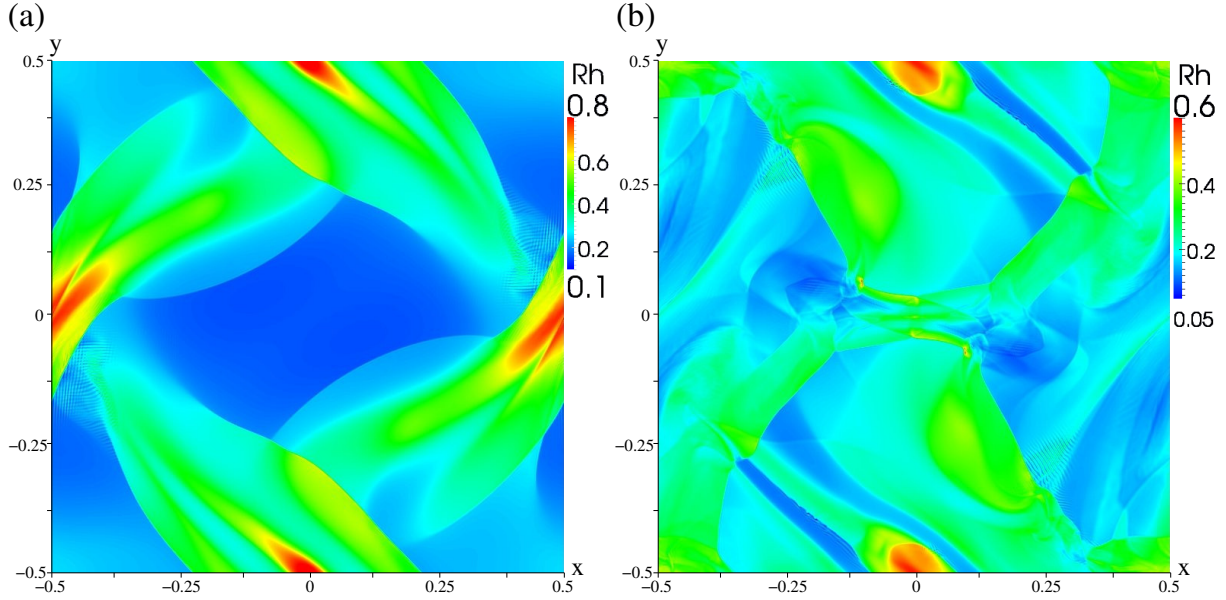


Figure 5.3: Orzsag-Tang vortex. The plasma density is displayed in color scale at time $t = 0.25$ (a) and $t = 0.50$ (b).

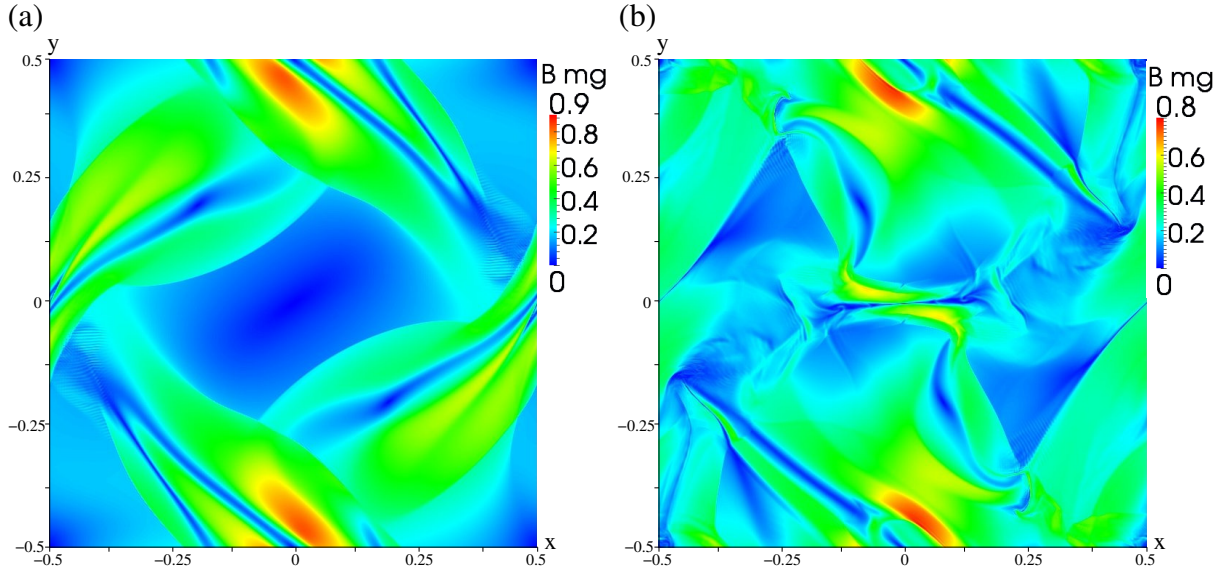


Figure 5.4: Orzsag-Tang vortex. The magnitude of magnetic field is displayed in color scale at times $t = 0.25$ (a) and $t = 0.50$ (b).

5.3 Resistive decay of cylindric current

In order to asses applicability of our code to solutions of non-ideal (resistive) MHD problems and to estimate its numerical resistivity we performed the following test: At the initial state $t = 0$ cylindrical current $\mathbf{j}(r) = (0, 0, j_z(r))$ with

$$j_z(r) = \begin{cases} j_0 J_0(x_N \frac{r}{r_0}) & : r \leq 1 \\ 0 & : r > 1 \end{cases}$$

flows through the plasma of uniform density ρ_0 . Here, $j_0 = 1$ is the amplitude of current density on the cylinder axis, $r_0 = 1$ is the cylinder radius, and $x_N \approx 2.40$ is the first null of Bessel function of 0th order $J_0(x)$. The resistivity inside the cylinder ($r \leq 1$) is uniform $\eta = \eta_0 = 0.1$, outside $\eta = 0$. In order to be able to compare numerical results with analytical solution and to split advective and resistive properties of code we set all velocities to zero at $t = 0$ and the density to a very high value $\rho_0 = 10^7$ to keep the plasma in rest. In the limit $\rho \rightarrow \infty$ the MHD system (3.66) effectively reduces into the diffusion equation

$$\frac{\partial \mathbf{B}}{\partial t} + \nabla \times (\eta \mathbf{j}) = \mathbf{0},$$

whose analytical solution for our initial state keeps the form $\mathbf{j}(r, t) = (0, 0, j_z(r, t))$ with

$$j_z(r, t) = j_0 J_0(x_N \frac{r}{r_0}) \exp(-\gamma t) + \frac{j_0}{2\pi x_N} J_1(x_N) [1 - \exp(-\gamma t)] \delta(r - r_o), \quad (5.1)$$

where $J_1(x)$ is the Bessel function of 1st order and $\delta(x)$ is the Dirac delta function. The decrement γ reads

$$\gamma = \eta \left(\frac{x_N}{r_0} \right)^2. \quad (5.2)$$

The second term in Eq. (5.1) represents induced surface current that compensates resistive decrease of current density inside the column to keep the magnetic field in the outer superconducting domain constant. The corresponding magnetic field is of form $\mathbf{B} = (0, B_\phi, 0)$ where

$$B_\phi(r, t) = j_0 \frac{r_0}{x_N} J_1(x_N \frac{r}{r_0}) \exp(-\gamma t)$$

for an internal ($r \leq r_0$) region and

$$B_\phi(r, t) = j_0 \frac{r_0}{x_N} J_1(x_N)$$

for an outer space.

The computing domain is divided into the homogeneous mesh of $2 \times 512 \times 512$ triangles in our numerical test. We use the first order basis functions for approximation of numerical solution. Free boundary conditions were applied on all boundaries. Results of this test are shown in Fig. 5.5. Fig. 5.5(a) shows the time evolution of current density profile along $y = 0$ for five subsequent time instants. The resistive decrease of j_z inside the column accompanied by a formation of induced surface current are well visible. Fig. 5.5(b) demonstrates comparison of numerical and analytical solutions for time evolution of current density $j_z(x, y, t)$ at $x = 0, y = 0$. As we can see, the results agree well with an analytically predicted current decay. Also the induced current density ring is spread only over two elements and does not spread further.

A comparison of LSFEM solution and FDM is presented in the Fig. 5.6. The graph shows current decay simulated by Leap-Frog FDM plotted by green dashed line, MacCormack FDM (blue dashed line) and LSFEM (black dashed line). The mesh resolution 512×512 for both FD methods was used. We can see a sharp drop to zero of current in the case of both FD methods. This artifact is caused by a numerical instability which is spreading away from the limb of the resistive disk and is propagating to the center. The growth rate and speed of propagation increases with the grid resolution which is a strong hint for a numerical origin of the instability. We attribute this numerical instability to the anisotropic nature of the discretization scheme whose diffusion operator does not take into account diagonal grid-points.

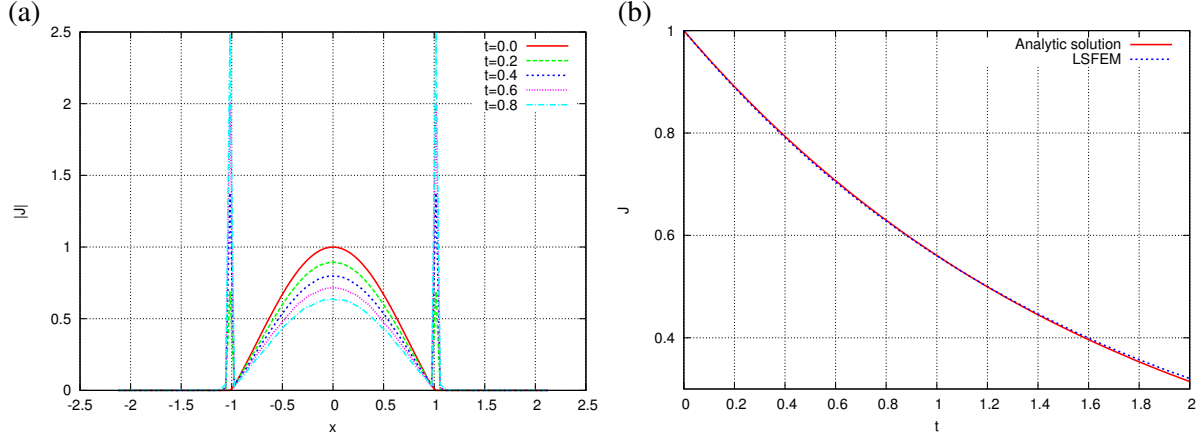


Figure 5.5: The resistive decay of cylindrical current density with time. (a) profiles of $j_z(x, 0, t)$ at five subsequent times. (b) Time profile of $j_z(0, 0, t)$ - comparison between numerical and analytical [Eq. (5.1)] solutions.

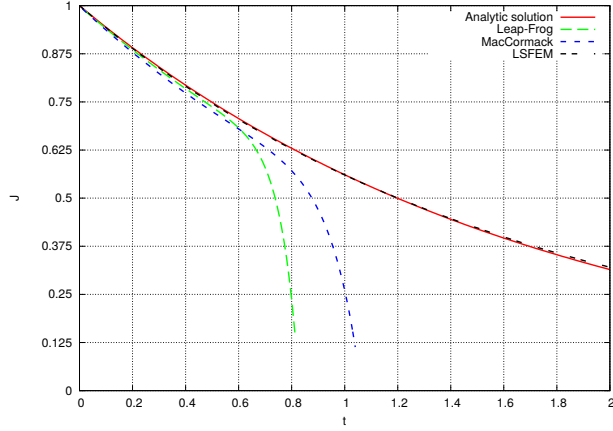


Figure 5.6: The resistive decay of cylindrical current density with time produced by FDM – Leap-Frog (green dashed line) and MacCormack (blue dashed line), LSFEM (black dashed line) and analytical solution (red full line).

5.4 Mesh refinement

In this section we present ability of FEM generate natural refine meshes for better sampling steep gradients. The mesh refinement is used on MHD simulation of magnetic field reconnection. The initial state is set according to Harris-like current sheet (see next section 5.5 for detail settings). The magnetic field reconnection is triggered by a momentum impulse, see Fig. 5.7, where the unstructured mesh of the computational domain is also visible. The outflow is set in y direction and 10 \times smaller inflow is set in x direction as a initial state. The mesh consist of ~ 10000 elements.

In Fig. 5.8 we can see the magnetoacoustic waves propagating from the place of the initial momentum impulse. We can recognize the fast and slow mode waves. The self adaptive FEM has small numeric viscosity. Hence, the propagating waves and their interactions are clearly visible.

The first results shows availability FEM for solving MHD equations and studying magnetic reconnection. Namely self-adaptive mesh of finite elements follow well the structure of

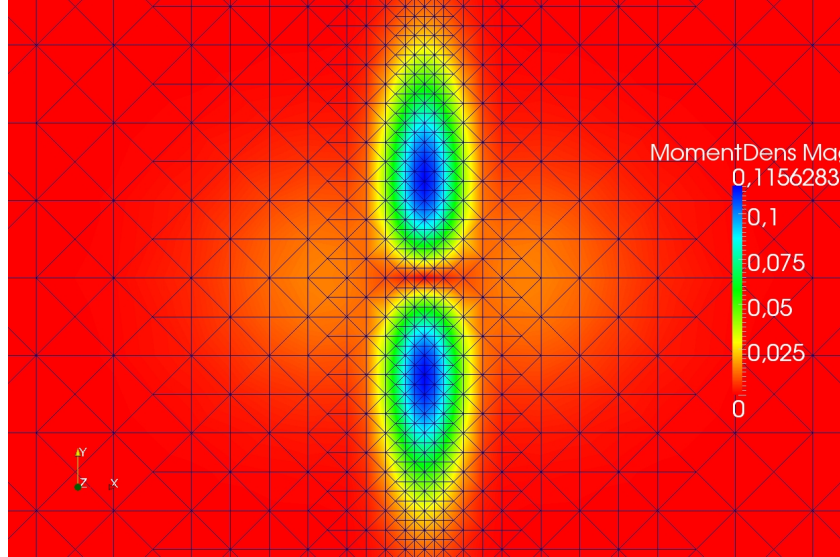


Figure 5.7: The initial momentum density. Zoomed mesh is also visible.

filamenting current sheet. This feature is important for investigation of the energy cascades in reconnection which is truly multi-scale process.

The proper implementation of mesh refinement is very challenging. Our code contains only h-adaptivity with simple rule for element splitting – if the gradient on the element is greater than given threshold then the element is divided into two elements. The implementation of more sophisticated refinement bring several problems: 1) The p-adaptivity produce hanging nodes (they have no partner in neighboring element) and they have to be taken into account (see Solin and Cerveny (2008)). 2) When we consider hp-adaptivity then one element can be refined by in many different ways (see Solin et al. (2010)). The proper implementation of hp-adaptivity is beyond our capabilities but there is a possibility to use open source library for the hp-refinement (e.g. Solin (2012)). The hp-library will be implemented into our code in a near future.

5.5 Magnetic field reconnection

We used LSFEM described in section 4 for a numerical simulation of magnetic reconnection in a flare-like current sheet. The reference frame was chosen to have the y -axis in the vertical direction, the z -axis is in the invariant direction along the current sheet and the x -axis is perpendicular to the current sheet. The free Neumann boundary conditions $\frac{\partial}{\partial n} = 0$ are applied at the top, right and left sides except the normal component of magnetic field B_n . The component B_n is given by equation $\nabla \cdot \mathbf{B} = 0$. The mixed Neumann and Dirichlet boundary conditions are applied on the bottom side. The Dirichlet boundary condition is applied to momentum density $\pi = 0$ and tangential component of magnetic field $B_t = 0$ the other quantities are given by free Neumann boundary conditions. The Dirichlet conditions ensures that the principal magnetic field component is vertical at the bottom boundary and the total flux passing through the boundary does not change, as enforce by the presence of a dense solar photosphere (see Bárta et al. (2008)). The simulation box is set to $< -24, 24 > \times < -80, 80 >$. The domain is divided into homogeneous mesh with $2 \times 640 \times 2200 = 2.816 \cdot 10^6$ elements. The first order shape functions are mapped on the elements. The plasma beta parameter used in simulations is set to $\beta = 0.15$ and the ratio of specific heats is $\gamma = 5/3$. The initial condition is set according

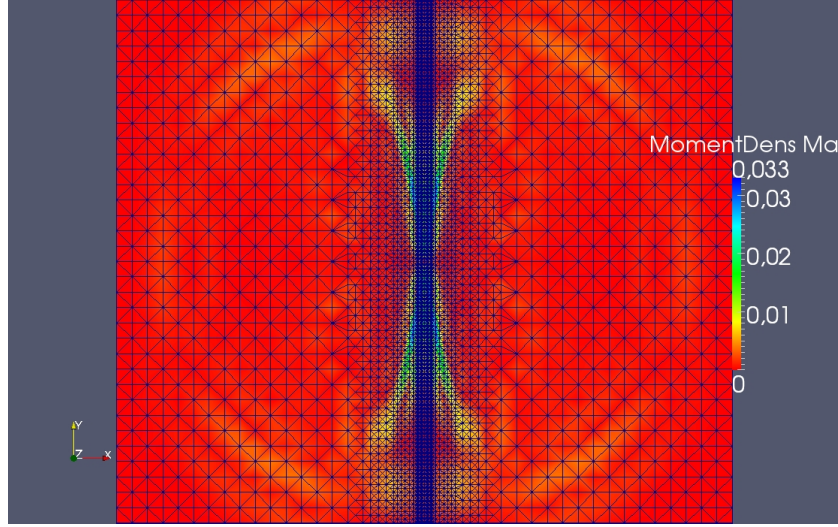


Figure 5.8: Magnetoacoustic waves propagating across computational domain from the center. The waves were created by initial momentum impulse.

to Harris-type current sheet (see Kliem et al. (2000))

$$\begin{aligned} \rho &= 1, & \pi &= 0, \\ B_x &= 0, & B_y &= -\tanh(x), \\ p &= 1 + \beta - U_m, & U &= \frac{p}{\gamma-1} + U_m, \\ J_z &= -(\cosh(x))^{-2}. \end{aligned} \quad (5.3)$$

The Harris-type current sheet is stable state due to we apply the initial perturbation to initialize spontaneous magnetic reconnection (see Magara et al. (1996)). The current sheet is perturbed by a small localized resistivity according to Kliem et al. (2000)

$$\eta(x, y, t) = 0.02 \exp\left(-\left(\frac{x^2 + y^2}{0.8^2}\right)\right). \quad (5.4)$$

The resistivity is applied for short time $0\tau_A \leq t \leq 10\tau_A$. Thereafter the resistivity is determined on each element in the each time step. Generalized resistivity is modelled by term (see Kliem et al. (2000))

$$\eta(x, y, t) = \begin{cases} 0 & : |v_D| \leq v_{cr} \\ C \frac{(|v_D(r,t)| - v_{cr})}{v_0} & : |v_D| > v_{cr} \end{cases}. \quad (5.5)$$

The term express general accepted fact if velocity difference between electrons and ions

$$v_D(\mathbf{r}, t) = \frac{\mathbf{j}(\mathbf{r}, t)}{en_e} \quad (5.6)$$

expressed in electric current, exceed critical velocity v_{cr} the fluctuated electric field is formed due to kinetic instabilities (Buneman's instability). The electrons are scattered on this field (similarly as collisions with ions). This mechanism is called anomalous resistivity. In the simulation we used $v_{cr} = 3.0$.

The dynamical time evolution of described system is shown in figure 5.9. The evolution was triggered by a small resistivity perturbation at the domain center and then it leads to a small burst of reconnection at the location of the initial perturbation. This leads to acceleration of a plasma along the current sheet (y axis) by Lorentz force, see Fig. 5.9 - time $t = 10$. According to mass

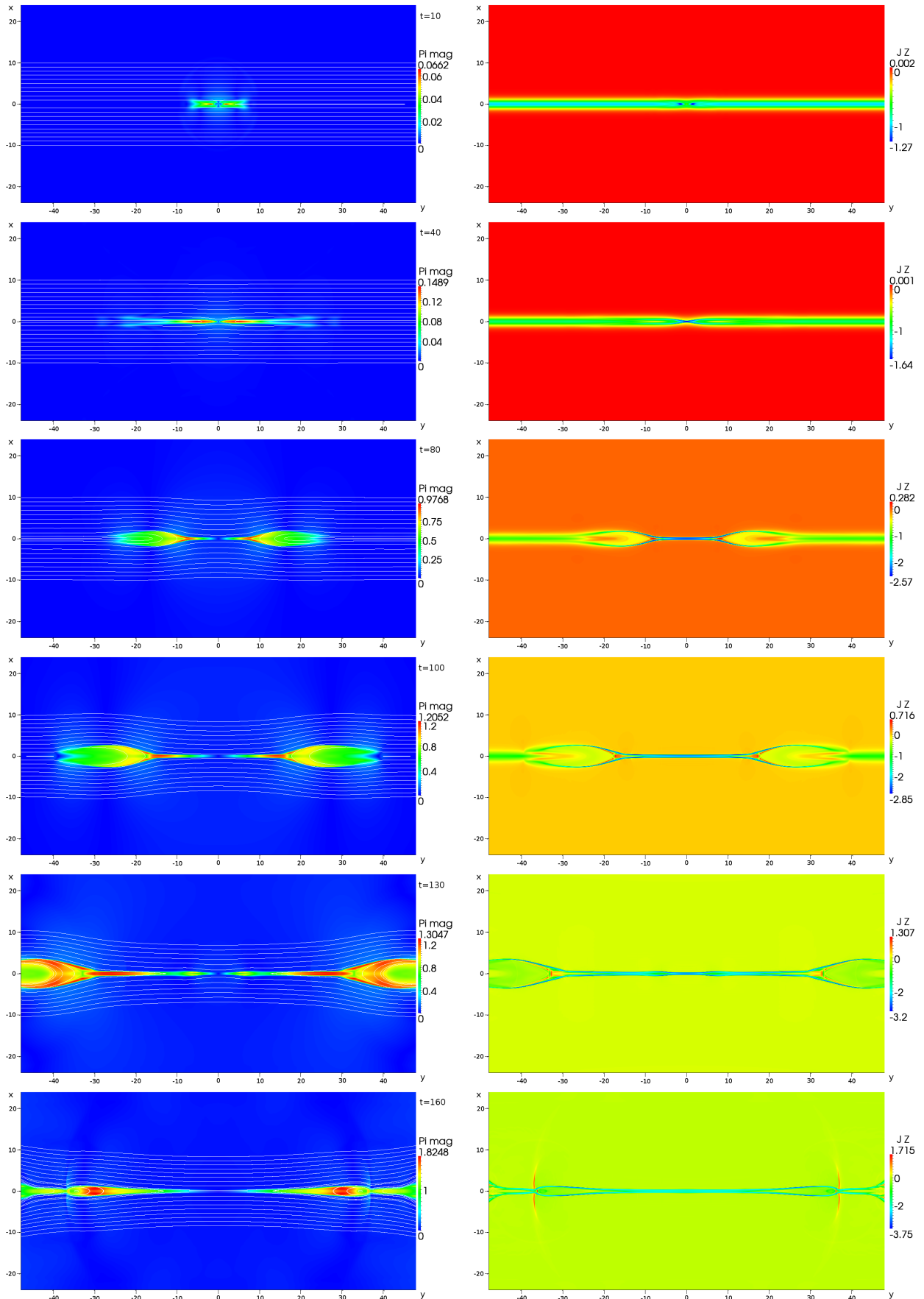


Figure 5.9: The momentum density with the magnetic field lines (left panels) and the current density (right panels) at characteristic times of evolution.

conservation law the plasma inflow is enforced into the region of initial resistivity perturbation. This brings a new magnetic flux toward the current sheet, which leads to increase of the current density. The current sheet is further stretched and compressed, since it reaches threshold v_{cr} for the anomalous resistivity and the localized resistivity is switch on at origin around time $t \sim 60$. Small resistivity region forms a Petschek-like reconnection, which reconnect even more magnetic field lines rapidly. A new reconnected field lines are accelerated by the Lorentz force from the center and forms the outflows of heated plasma. This plasma outflows reach the Alfvén velocity about $t \sim 80$. Then the current sheet is continuously stretched by the fast outflows ($t = 100$). The long and thin current sheet forms the Sweet-Parker reconnection configuration and the anomalous resistivity is switched on the few location simultaneously. A several new X-points are formed – the so-called secondary tearing. Around time $t \sim 130$, the plasmoids are formed and they are pulled to boundaries with the outflows. The plasmoids are further accelerated then the fast shocks are formed in front of magnetic islands around time $t = 160$.

5.6 Parallel scaling

The test of parallel scaling is presented in this section. In order to investigate the performance of the parallelization of LSFEM code we ran a several tests. The initial condition are set according to the Harris current sheet. The dimension of a domain is 10×32 and it is divided into 64000 triangular elements with the first order of basis functions. The JCGM is set to the fix number 100 iterations and number of Newton-Raphson linearization is fixed to three. We perform two sets of tests for two different maximum evolution times $t_{max} = 5\tau_A$ and $t_{max} = 50\tau_A$. The computation times are showed in the table 5.6. In the figure 5.10 we can see comparison between measured computational times and ideal scaling times. The plot shows overall good strong scaling (the reduction of the computing time for fixed grid size with an increasing number of CPU cores). The deviations from the ideal scaling curves that become more apparent at higher core counts due to the relatively longer fraction of time spent in the MPI communication (halo exchange) between the domains.

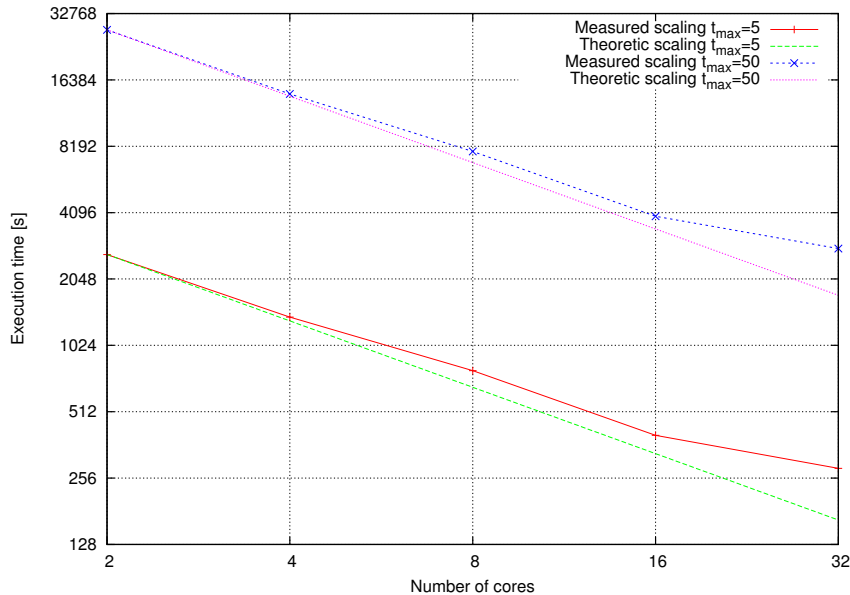


Figure 5.10: Graph of parallel scaling of LSFEM MHD code. Computation times for 2, 4, 8, 16 and 32 cores are presented. Measured values are presented by red and blue lines with points. The theoretic scaling is denoted by green and purple lines.

N_{cores}	$t_{max} = 5$		$t_{max} = 50$	
	Time [s]	Time [min]	Time [s]	Time [min]
2	2644.1	44.07	27635.2	460.59
4	1375.9	22.93	14139.2	235.65
8	786.2	13.10	7756.4	129.27
16	400.0	6.69	3941.2	65.69
32	283.5	4.73	2814.5	46.91

Table 5.1: Computation times for 2, 4, 8, 16 and 32 cores is presented and two sets of maximum MHD evolution times $t_{max} = 5\tau_A$ and $t_{max} = 50\tau_A$ are compared.

Chapter 6

Discussion and conclusions

The FEM represent an alternative to Finite-Difference/Finite-Volume method that are traditionally used for solution of MHD problems in astrophysics. Its attractivity implies from its unstructured mesh that allows for appropriate local refinement without formation of any qualitative internal boundaries between the fine and coarse meshes. This property makes it very useful for handling the multi-scale problems, for example the problem of magnetic reconnection in solar flares Bárta et al. (2011b) (and other large-scale systems) or MHD turbulence.

With this intention in mind we have developed the LSFEM implementation of a MHD solver whose descriptions and results from its application to the standardized test problems are presented in this work.

To sum up the main points of our implementation: Transformation of MHD equations (3.66) to the standard FEM problem (4.3) involves several steps: (i) Standard θ -time discretization, (ii) Decrease of order of system of equations by introduction of a new variable – a current density, and (iii) Newton-Raphson linearization. The possibility to include the solenoidal condition $\nabla \cdot \mathbf{B} = 0$ directly into the system of equations certainly belongs to advantages of LSFEM formulation, as well as a natural involvement of boundary conditions. The element-by-element assembling of global stiffness matrix and the iterative nature of JCGM solver allow for rather easy and efficient MPI parallelization. Integrals over elements are efficiently performed via Gauss quadrature.

The LSFEM implementation has been successfully tested by solving 2D and 3D the Burgers' equation. The relative simple form of the Burgers' equation allows us to introduced the analytical integration and avoid using Gaussian quadrature. Unfortunately, the analytical integration is limited to rather simple PDE equations with low order of nonlinearity and low order of element functions.

The study of the overdetermined system of MHD equations with additional solenoidal condition shows that the divergence \mathbf{B} can be successfully suppressed. On the other hand, we found that the additional equation also increases the condition number of the stiffness matrix and makes it more difficult to solve by JCGM.

We performed several standardized tests focused on an ideal and resistive MHD. The LSFEM MHD solver quite closely reproduces results published for the Ryu-Jones shock tube problem (Ryu and Jones, 1995). Small spurious oscillations appear around the points where the first derivative of an analytical solution does not exist. Choice of higher-order basis functions makes the situation even slightly worse.

Similar feature can be seen in the results from the Orszag-Tang vortex test problem. While the large-scale dynamics agree well with those obtained from the 'gauge' codes, small oscillations accompanying the shocks are visible again. These effects are caused by the least squares curve fitting approach (Bochev and Gunzburger, 2009). We believe that it can be cured by an introduction of a small background resistivity and local refinement of mesh around the discontinuities, with the element size corresponding to the resistivity-controlled (magnetic) Reynolds

number. Such approach is fully in line with the intended usage of code for detailed studies of current sheet filamentation and fragmentation in a large-scale magnetic reconnection in solar flares. Indeed, in the solar corona we have a very small background resistivity due to a high temperature of coronal plasma. Hence, having mesh around the filamenting current sheet locally refined as much as possible we can set the background (physical) resistivity accordingly and approach thus the realistic Lundquist number in the solar corona.

In the last test – with the intended usage of code in mind – we have tested the properties of our implementation for solution of resistive problems. In order to get a comparison with an analytical solution we have ‘frozen’ the plasma dynamics by setting high matter density and we concentrated on a purely diffusive problem. The results show a rather good agreement with the analytical solution. Namely, the induced surface current density is located only at a few elements and did not diffuse further with time. This is an important result for intended studies of current-sheet filamentation in the flare reconnection.

The simulation of the Harris-like current sheet with the mesh refinement reproduces expected formation of the current sheet tearing with formation of plasmoids. Moreover this simulations reveals that there is no negative influence of the locally refined mesh on the numeric solution as partially reflected waves on the interface between coarse and finer mesh. As the numeric tests show, LSFEM has very small numeric diffusivity which leads to the very fast magnetic field reconnection. The anomalous resistivity is localized to the very small region (corresponding to the concentrated current density according to the used resistivity model) which leads to the fast Petschek-like reconnection. The acceleration of the outflow and reconnected field lines by Lorenz force is not disturbed by numeric viscosity and the stretching of the current sheet is very fast. The long and stretched current sheet is prone to secondary tearing and then plasmoid formation.

The tests show basic applicability of our LSFEM implementation of MHD solver for a solution of selected problems. At the same moment they reveal the necessity to involve both the adaptive spatial refinement (it has already been implemented) and adaptive change of order of basis functions over selected elements (h-p refinement). The proper implementation of hp-adaptivity is beyond our capabilities but there is a possibility to use open source library for the hp-refinement (e.g. Solin (2012)). The hp-library will be implemented into our code in a near future.

Acknowledgments

This research was supported by the grants P209/12/0103 (GA ČR), P209/10/1680 (GA ČR), IGA UJEP 5322215000801, GACR 13-24782S, the research projects RVO:67985815 (CZ), DFG Collaborative Research Center 963, Project A02 (DE) and support of the European Commission via the PCIG-GA-2011-304265 project financed in frame of the FP7-PEOPLE-2011-CIG programme. Our further gratitudes go the Max Planck Institute for Solar System Research and Max Planck Computing and Data Facility (formerly known as Rechenzentrum Garching) for proving an infrastructure. Data supplied courtesy of the SDO/HMI and SOHO/AIA consortia. SDO is the first mission to be launched for NASA’s Living With a Star (LWS) Program.

Chapter 7

Appendix

7.1 MHD equations in conservative form

The dimensionless MHD equations in the conservation form are

$$\frac{\partial \Psi_1}{\partial t} + \Psi_2 + \frac{\partial \mathbf{F}_i}{\partial x_i} = 0, \quad (7.1)$$

where vectors of unknown variables are $\Psi_1 = (\rho, \pi_1, \pi_2, \pi_3, B_1, B_2, B_3, U, 0, 0, 0, 0)$, $\Psi_2 = (0, 0, 0, 0, 0, 0, 0, J_1, J_2, J_3)$ and \mathbf{F}_i is flux in the direction of x_i

$$\mathbf{F}_i = \begin{pmatrix} \pi_i \\ \frac{\pi_1 \pi_i}{\rho} - B_1 B_i + \frac{1}{2} \delta_{1i} (p + U_m) \\ \frac{\pi_2 \pi_i}{\rho} - B_2 B_i + \frac{1}{2} \delta_{2i} (p + U_m) \\ \frac{\pi_3 \pi_i}{\rho} - B_3 B_i + \frac{1}{2} \delta_{3i} (p + U_m) \\ \frac{\pi_i B_1 - \pi_1 B_i}{\rho} + \eta \varepsilon_{1ij} J_j \\ \frac{\pi_i B_2 - \pi_2 B_i}{\rho} + \eta \varepsilon_{2ij} J_j \\ \frac{\pi_i B_3 - \pi_3 B_i}{\rho} + \eta \varepsilon_{3ij} J_j \\ \frac{\pi_i}{\rho} \left(\frac{\gamma}{\gamma-1} p + U_k \right) + 2 \eta \varepsilon_{ijk} J_j B_k + \frac{2}{\rho} \varepsilon_{ijk} (\pi_k B_i - \pi_i B_k) B_k \\ -\varepsilon_{1ik} B_k \\ -\varepsilon_{2ik} B_k \\ -\varepsilon_{3ik} B_k \end{pmatrix} \quad (7.2)$$

where $U_k = \frac{\pi_i \pi_i}{\rho}$ is the kinetic energy, $U_m = B_i B_i$ is the magnetic energy and $p = (\gamma - 1)(U - U_k - U_m)$ is the pressure. We have to mention that the last three terms in the flux \mathbf{F}_i are definition of current density. We want to use time discretization and linearization described in the section 4.9 for this we define $\Psi = \Psi_1 + \Psi_2$.

7.2 Dimensionless 3D MHD equations

$$\begin{aligned}
\frac{\partial \rho}{\partial t} + \frac{\partial}{\partial x} [\pi_1] + \frac{\partial}{\partial y} [\pi_2] + \frac{\partial}{\partial z} [\pi_3] &= 0 \\
\frac{\partial \pi_1}{\partial t} + \frac{\partial}{\partial x} \left[\frac{\pi_1^2}{\rho} + \frac{B_2^2 + B_3^2 - B_1^2 + p}{2} \right] + \frac{\partial}{\partial y} \left[\frac{\pi_1 \pi_2}{\rho} - B_1 B_2 \right] + \frac{\partial}{\partial z} \left[\frac{\pi_1 \pi_3}{\rho} - B_1 B_3 \right] &= 0 \\
\frac{\partial \pi_2}{\partial t} + \frac{\partial}{\partial x} \left[\frac{\pi_1 \pi_2}{\rho} - B_1 B_2 \right] + \frac{\partial}{\partial y} \left[\frac{\pi_2^2}{\rho} + \frac{B_1^2 + B_3^2 - B_2^2 + p}{2} \right] + \frac{\partial}{\partial z} \left[\frac{\pi_2 \pi_3}{\rho} - B_2 B_3 \right] &= 0 \\
\frac{\partial \pi_3}{\partial t} + \frac{\partial}{\partial x} \left[\frac{\pi_1 \pi_3}{\rho} - B_1 B_3 \right] + \frac{\partial}{\partial y} \left[\frac{\pi_2 \pi_3}{\rho} - B_2 B_3 \right] + \frac{\partial}{\partial z} \left[\frac{\pi_3^2}{\rho} + \frac{B_1^2 + B_2^2 - B_3^2 + p}{2} \right] &= 0 \\
\frac{\partial B_1}{\partial t} + \frac{\partial}{\partial x} [0] + \frac{\partial}{\partial y} \left[\frac{\pi_2 B_1 - \pi_1 B_2}{\rho} + \eta J_3 \right] + \frac{\partial}{\partial z} \left[-\frac{\pi_1 B_3 - \pi_3 B_1}{\rho} - \eta J_2 \right] &= 0 \\
\frac{\partial B_2}{\partial t} + \frac{\partial}{\partial x} \left[-\frac{\pi_2 B_1 - \pi_1 B_2}{\rho} - \eta J_3 \right] + \frac{\partial}{\partial y} [0] + \frac{\partial}{\partial z} \left[\frac{\pi_3 B_2 - \pi_2 B_3}{\rho} + \eta J_1 \right] &= 0 \\
\frac{\partial B_3}{\partial t} + \frac{\partial}{\partial x} \left[\frac{\pi_1 B_3 - \pi_3 B_1}{\rho} + \eta J_2 \right] + \frac{\partial}{\partial y} \left[-\frac{\pi_3 B_2 - \pi_2 B_3}{\rho} - \eta J_1 \right] + \frac{\partial}{\partial z} [0] &= 0 \\
\frac{\partial U}{\partial t} + \frac{\partial}{\partial x} \left[\left(\gamma U - \gamma (B_1^2 + B_2^2 + B_3^2) + (1 - \gamma) \frac{\pi_1^2 + \pi_2^2 + \pi_3^2}{\rho} \right) \frac{\pi_1}{\rho} + 2(E_2 B_3 - E_3 B_2) \right] \\
+ \frac{\partial}{\partial y} \left[\left(\gamma U - \gamma (B_1^2 + B_2^2 + B_3^2) + (1 - \gamma) \frac{\pi_1^2 + \pi_2^2 + \pi_3^2}{\rho} \right) \frac{\pi_2}{\rho} + 2(E_3 B_1 - E_1 B_3) \right] \\
+ \frac{\partial}{\partial z} \left[\left(\gamma U - \gamma (B_1^2 + B_2^2 + B_3^2) + (1 - \gamma) \frac{\pi_1^2 + \pi_2^2 + \pi_3^2}{\rho} \right) \frac{\pi_3}{\rho} + 2(E_1 B_2 - E_2 B_1) \right] &= 0
\end{aligned}$$

where \mathbf{E} is electric field intensity defined as

$$\begin{aligned}
E_1 &= \frac{\pi_3 B_2 - \pi_2 B_3}{\rho} + \eta J_1 \\
E_2 &= \frac{\pi_1 B_3 - \pi_3 B_1}{\rho} + \eta J_2 \\
E_3 &= \frac{\pi_2 B_1 - \pi_1 B_2}{\rho} + \eta J_3
\end{aligned}$$

Plasma pressure p is

$$p = (\gamma - 1) \left[U - \frac{\pi_1^2 + \pi_2^2 + \pi_3^2}{\rho} - (B_1^2 + B_2^2 + B_3^2) \right]$$

The \mathbf{J} is current density

$$\begin{aligned}
J_1 &= \frac{\partial B_3}{\partial y} - \frac{\partial B_2}{\partial z} \\
J_2 &= \frac{\partial B_1}{\partial z} - \frac{\partial B_3}{\partial x} \\
J_3 &= \frac{\partial B_2}{\partial x} - \frac{\partial B_1}{\partial y}
\end{aligned}$$

7.3 Conjugate Gradient Method

The conjugate gradient method (CGM) is an algorithm for the numerical solution of a system of linear algebraic equations $\mathbf{A}\mathbf{x} = \mathbf{f}$. This method was first proposed by Hestenes and Stiefel (see Hestenes and Stiefel (1952)) in 1952. The CGM is applicable on systems whose matrix A is symmetric and positive-definite. The CGM is an iterative method, so it can be applied, with advance, to sparse systems that are too large to be handled by any direct methods. This kind of system arise when numerically solving partial differential equations and also from LSSEM. The CGM algorithm is following:

1. Set initial values \mathbf{x}^k
2. Determine residual $\mathbf{r}^k = \mathbf{f} - \mathbf{A}\mathbf{x}^k$
3. Set first direction of convergence $\mathbf{v}^k = \mathbf{r}^k$
4. Compute a coefficient $a^k = \frac{\mathbf{v}^k \cdot \mathbf{r}^k}{\mathbf{v}^k \cdot \mathbf{A}\mathbf{v}^k}$
5. Compute a solution $\mathbf{x}^{k+1} = \mathbf{x}^k + a^k \mathbf{v}^k$
6. Compute a residual $\mathbf{r}^{k+1} = \mathbf{r}^k - a^k \mathbf{A}\mathbf{v}^k$
7. If residuum \mathbf{r}^{k+1} is sufficiently small then stop computing
8. Compute a coefficient $b^k = \frac{\mathbf{v}^{k+1} \cdot \mathbf{A}\mathbf{r}^{k+1}}{\mathbf{v}^k \cdot \mathbf{A}\mathbf{v}^k}$
9. Compute a new direction of convergence $\mathbf{v}^{k+1} = \mathbf{r}^{k+1} - b^k \mathbf{v}^k$
10. Return to step 4

7.4 Preconditioned Conjugate Gradient Method

In order to construct preconditioned version of CGM we multiply both sides of system of linear equations by a matrix \mathbf{Q}^{-1} and obtain

$$\mathbf{Q}^{-1}\mathbf{A}\mathbf{x} = \mathbf{Q}^{-1}\mathbf{f}, \quad (7.3)$$

where Q is called preconditioner and it is a symmetric and positive definite matrix with same sparsity like a matrix A. The preconditioner decrease a condition number of original system and thus increase convergence rate of CGM. The algorithm of JCGM is following

1. Set initial values \mathbf{x}^k
2. Determine residual $\mathbf{r}^k = \mathbf{f} - \mathbf{A}\mathbf{x}^k$
3. Apply preconditioner $\mathbf{s}^k = \mathbf{Q}^{-1}\mathbf{r}^k$
4. Set first direction of convergence $\mathbf{v}^k = \mathbf{s}^k$
5. Compute a coefficient $a^k = \frac{\mathbf{v}^k \cdot \mathbf{r}^k}{\mathbf{v}^k \cdot \mathbf{A}\mathbf{v}^k}$
6. Compute a solution $\mathbf{x}^{k+1} = \mathbf{x}^k + a^k \mathbf{v}^k$
7. Compute a residual $\mathbf{r}^{k+1} = \mathbf{r}^k - a^k \mathbf{A}\mathbf{v}^k$
8. Apply preconditioner $\mathbf{s}^{k+1} = \mathbf{Q}^{-1}\mathbf{r}^{k+1}$
9. If residuum $\mathbf{r}^{k+1} \cdot \mathbf{s}^{k+1}$ is sufficiently small then stop computing

10. Compute a coefficient $b^k = \frac{\mathbf{r}^{k+1} \cdot \mathbf{s}^{k+1}}{\mathbf{r}^k \cdot \mathbf{s}^k}$
11. Compute a new direction of convergence $\mathbf{v}^{k+1} = \mathbf{r}^{k+1} - b^k \mathbf{v}^k$
12. Return to step 5

7.5 MHD operator

In this section we present a whole linearized and time discretized MHD operator. From computational point of view is convenient separate operator (4.64) into several part

$$\mathcal{A}\phi_i = \theta\Delta t \left(\mathcal{O}\phi_i + \mathcal{P}\frac{\partial\phi_i}{\partial x} + \mathcal{Q}\frac{\partial\phi_i}{\partial y} + \mathcal{R}\frac{\partial\phi_i}{\partial z} \right). \quad (7.4)$$

In the following text we use nonstandard denotations for derivatives due to shorter notation. The derivatives are denoted by upper script i.e. $\frac{\partial}{\partial x} \rightarrow {}^x, \frac{\partial}{\partial y} \rightarrow {}^y$ and $\frac{\partial}{\partial z} \rightarrow {}^z$.

$$\mathcal{O}_{11} = \frac{1}{\theta\Delta t}, \quad \mathcal{O}_{12} \dots \mathcal{O}_{111} = 0$$

$$\begin{aligned} \mathcal{O}_{21} &= \frac{1}{\rho^3}((\rho^x - \rho^x\gamma)\pi_2^2 + (\rho^x - \rho^x\gamma)\pi_3^2 + \pi_1((3\rho^x - \rho^x\gamma)\pi_1 + 2\rho^y\pi_2 + 2\rho^z\pi_3) + +\rho(\pi_2(-\pi_2^x + \gamma\pi_2^y - \pi_1^y) + \pi_3(-\pi_3^x + \gamma\pi_3^y - \pi_1^z) + \pi_1(-3\pi_1^x + \gamma\pi_1^y - \pi_2^y - \pi_3^z))) \\ \mathcal{O}_{22} &= \frac{1}{\theta\Delta t} + \frac{1}{\rho^2}((-3\rho^x + \rho^x\gamma)\pi_1 - \rho^y\pi_2 - \rho^z\pi_3 + \rho(3\pi_1^x - \gamma\pi_1^y + \pi_2^y + \pi_3^z)) \\ \mathcal{O}_{23} &= \frac{1}{\rho^2}(-\rho^y\pi_1 + (-\rho^x + \rho^x\gamma)\pi_2 + \rho(\pi_2^x - \gamma\pi_2^y + \pi_1^y)) \\ \mathcal{O}_{24} &= \frac{1}{\rho^2}(-\rho^z\pi_1 + (-\rho^x + \rho^x\gamma)\pi_3 + \rho(\pi_3^x - \gamma\pi_3^y + \pi_1^z)) \\ \mathcal{O}_{25} &= -\gamma B_1^x - B_2^y - B_3^z \\ \mathcal{O}_{26} &= 2B_2^x - \gamma B_2^y - B_1^y \\ \mathcal{O}_{27} &= 2B_3^x - \gamma B_3^y - B_1^z \\ \mathcal{O}_{28} \dots \mathcal{O}_{211} &= 0 \end{aligned}$$

$$\begin{aligned} \mathcal{O}_{31} &= \frac{1}{\rho^3}(\pi_1((\rho^y - \rho^y\gamma)\pi_1 + 2\rho^x\pi_2) + (\rho^y - \rho^y\gamma)\pi_3^2 + \pi_2((3\rho^y - \rho^y\gamma)\pi_2 + 2\rho^z\pi_3) + +\rho(\pi_1(-\pi_2^x - \pi_1^y + \gamma\pi_1^y) + \pi_3(-\pi_3^y + \gamma\pi_3^y - \pi_2^z) + \pi_2(-\pi_1^x - 3\pi_2^y + \gamma\pi_2^y - \pi_3^z))) \\ \mathcal{O}_{32} &= \frac{1}{\rho^2}((- \rho^y + \rho^y\gamma)\pi_1 - \rho^x\pi_2 + \rho(\pi_2^x + \pi_1^y - \gamma\pi_1^y)) \\ \mathcal{O}_{33} &= \frac{1}{\theta\Delta t} + \frac{1}{\rho^2}(-\rho^x\pi_1 + (-3\rho^y + \rho^y\gamma)\pi_2 - \rho^z\pi_3 + \rho(\pi_1^x + 3\pi_2^y - \gamma\pi_2^y + \pi_3^z)) \\ \mathcal{O}_{34} &= \frac{1}{\rho^2}(-\rho^z\pi_2 + (-\rho^y + \rho^y\gamma)\pi_3 + \rho(\pi_3^y - \gamma\pi_3^y + \pi_2^z)) \\ \mathcal{O}_{35} &= -B_2^x + 2B_1^y - \gamma B_1^y \\ \mathcal{O}_{36} &= -B_1^x - \gamma B_2^y - B_3^z \\ \mathcal{O}_{37} &= 2B_3^y - \gamma B_3^z - B_2^z \\ \mathcal{O}_{38} \dots \mathcal{O}_{311} &= 0 \end{aligned}$$

$$\begin{aligned} \mathcal{O}_{31} &= \frac{1}{\rho^3}((3\rho^z - \rho^z\gamma)\pi_3^2 + \pi_1((\rho^z - \rho^z\gamma)\pi_1 + 2\rho^x\pi_3) + \pi_2((\rho^z - \rho^z\gamma)\pi_2 + 2\rho^y\pi_3) + +\rho(\pi_1(-\pi_3^x - \pi_1^z + \gamma\pi_1^z) + \pi_2(-\pi_3^y - \pi_2^z + \gamma\pi_2^z) + \pi_3(-\pi_1^x - \pi_2^y - 3\pi_3^z + \gamma\pi_3^z))) \\ \mathcal{O}_{42} &= \frac{1}{\rho^2}((- \rho^z + \rho^z\gamma)\pi_1 - \rho^x\pi_3 + \rho(\pi_3^x + \pi_1^z - \gamma\pi_1^z)) \\ \mathcal{O}_{43} &= \frac{1}{\rho^2}((- \rho^z + \rho^z\gamma)\pi_2 - \rho^y\pi_3 + \rho(\pi_3^y + \pi_2^z - \gamma\pi_2^z)) \\ \mathcal{O}_{44} &= \frac{1}{\theta\Delta t} + \frac{1}{\rho^2}(-\rho^x\pi_1 - \rho^y\pi_2 + (-3\rho^z + \rho^z\gamma)\pi_3 + \rho(\pi_1^x + \pi_2^y + 3\pi_3^z - \gamma\pi_3^z)) \\ \mathcal{O}_{45} &= -B_3^x + 2B_1^z - \gamma B_1^z \\ \mathcal{O}_{46} &= -B_3^y + 2B_2^z - \gamma B_2^z \\ \mathcal{O}_{47} &= -B_1^x - B_2^y - \gamma B_3^z \\ \mathcal{O}_{48} \dots \mathcal{O}_{411} &= 0 \end{aligned}$$

$$\begin{aligned} \mathcal{O}_{51} \dots \mathcal{O}_{54} &= 0, \quad \mathcal{O}_{55} = \frac{1}{\theta\Delta t}, \quad \mathcal{O}_{56} \dots \mathcal{O}_{511} = 0 \\ \mathcal{O}_{61} \dots \mathcal{O}_{65} &= 0, \quad \mathcal{O}_{66} = \frac{1}{\theta\Delta t}, \quad \mathcal{O}_{67} \dots \mathcal{O}_{611} = 0 \end{aligned}$$

$$\mathcal{O}_{71} \dots \mathcal{O}_{74} = 0, \quad \mathcal{O}_{77} = \frac{1}{\theta \Delta t}, \quad \mathcal{O}_{78} \dots \mathcal{O}_{711} = 0$$

$$\begin{aligned} \mathcal{O}_{81} &= \frac{1}{\rho^4} ((6\rho^z - 6\rho^z\gamma)\pi_3^3 + \pi_2((6\rho^y - 6\rho^y\gamma)\pi_3^2 + \pi_2((6\rho^y - 6\rho^y\gamma)\pi_2 + (6\rho^z - 6\rho^z\gamma)\pi_3)) + \\ &+ \pi_1((6\rho^x - 6\rho^x\gamma)\pi_2^2 + (6\rho^x - 6\rho^x\gamma)\pi_3^2 + \pi_1((6\rho^x - 6\rho^x\gamma)\pi_1 + (6\rho^y - 6\rho^y\gamma)\pi_2 + (6\rho^z - 6\rho^z\gamma)\pi_3)) + \rho(\rho(\pi_1(2\gamma B_1 B_1^x + 2\gamma B_2 B_2^x + 2\gamma B_3 B_3^x) + \pi_2(2\gamma B_1 B_1^y + 2\gamma B_2 B_2^y + 2\gamma B_3 B_3^y) + \\ &+ \pi_3(2\gamma B_1 B_1^z + 2\gamma B_2 B_2^z + 2\gamma B_3 B_3^z) + U(-\gamma\pi_1^x - \gamma\pi_2^y - \gamma\pi_3^z) + B_1^2(\gamma\pi_1^x + \gamma\pi_2^y + \gamma\pi_3^z) + \\ &+ B_2^2(\gamma\pi_1^x + \gamma\pi_2^y + \gamma\pi_3^z) + B_3^2(\gamma\pi_1^x + \gamma\pi_2^y + \gamma\pi_3^z)) + \pi_1(2U\rho^x\gamma - 2\rho^x\gamma B_1^2 - 2\rho^x\gamma B_2^2 - \\ &- 2\rho^x\gamma B_3^2 + \pi_2(-4\pi_1^x + 4\gamma\pi_1^x - 4\pi_1^y + 4\gamma\pi_1^y) + \pi_3(-4\pi_3^x + 4\gamma\pi_3^x - 4\pi_1^z + 4\gamma\pi_1^z) + \\ &+ \pi_1(-6\pi_1^x + 6\gamma\pi_1^x - 2\pi_2^y + 2\gamma\pi_2^y - 2\pi_3^z + 2\gamma\pi_3^z) + \pi_2(2U\rho^y\gamma - 2\rho^y\gamma B_1^2 - 2\rho^y\gamma B_2^2 - \\ &- 2\rho^y\gamma B_3^2 + \pi_3(-4\pi_3^y + 4\gamma\pi_3^y - 4\pi_2^z + 2\gamma\pi_2^z) + \pi_1(2U\rho^z\gamma - 2\rho^z\gamma B_1^2 - 2\rho^z\gamma B_2^2 - \\ &- 2\rho^z\gamma B_3^2 + \pi_3(-2\pi_1^x + 2\gamma\pi_1^x - 6\pi_2^y + 6\gamma\pi_2^y - 2\pi_3^z + 2\gamma\pi_3^z))) \\ \mathcal{O}_{82} &= \frac{1}{\rho^3} ((-2\rho^x + 2\rho^x\gamma)\pi_2^2 + (-2\rho^x + 2\rho^x\gamma)\pi_3^2 + \pi_1((-6\rho^x + 6\rho^x\gamma)\pi_1 + (-4\rho^y + 4\rho^y\gamma)\pi_2 + \\ &+ (-4\rho^z + 4\rho^z\gamma)\pi_3) + \rho(-U\rho^x\gamma + \rho^x\gamma B_1^2 + \rho^x\gamma B_2^2 + \rho^x\gamma B_3^2 + \rho(-2\gamma B_1 B_1^x - 2\gamma B_2 B_2^x - \\ &- 2\gamma B_3 B_3^x) + \pi_2(2\pi_2^x - 2\gamma\pi_2^x + 2\pi_1^y - 2\gamma\pi_1^y) + \pi_3(2\pi_3^x - 2\gamma\pi_3^x + 2\pi_1^z - 2\gamma\pi_1^z) + \pi_1(6\pi_1^x - \\ &- 6\gamma\pi_1^x + 2\pi_2^y - 2\gamma\pi_2^y + 2\pi_3^z - 2\gamma\pi_3^z))) \\ \mathcal{O}_{83} &= \frac{1}{\rho^3} (\pi_1((2\rho^y\gamma - 2\rho^y)\pi_1 + (-4\rho^x + 4\rho^x\gamma)\pi_2) + (-2\rho^y + 2\rho^y\gamma)\pi_3^2 + \pi_2((-6\rho^y + 6\rho^y\gamma)\pi_2 + \\ &+ (-4\rho^z + 4\rho^z\gamma)\pi_3) + \rho(-U\rho^y\gamma + \rho^y\gamma B_1^2 + \rho^y\gamma B_2^2 + \rho^y\gamma B_3^2 + \rho(-2\gamma B_1 B_1^y - 2\gamma B_2 B_2^y - \\ &- 2\gamma B_3 B_3^y) + \pi_1(2\pi_2^x - 2\gamma\pi_2^x + 2\pi_1^y - 2\gamma\pi_1^y) + \pi_3(2\pi_3^y - 2\gamma\pi_3^y + 2\pi_2^z - 2\gamma\pi_2^z) + \pi_2(2\pi_1^x - \\ &- 2\gamma\pi_1^x + 6\pi_2^y - 6\gamma\pi_2^y + 2\pi_3^z - 2\gamma\pi_3^z))) \\ \mathcal{O}_{84} &= \frac{1}{\rho^3} ((6\rho^z\gamma - 6\rho^z)\pi_3^2 + \pi_1((-2\rho^z + 2\rho^z\gamma)\pi_1 + (-4\rho^x + 4\rho^x\gamma)\pi_3) + \pi_2((-2\rho^z + 2\rho^z\gamma)\pi_2 + \\ &+ (-4\rho^y + 4\rho^y\gamma)\pi_3) + \rho(-U\rho^z\gamma + \rho^z\gamma B_1^2 + \rho^z\gamma B_2^2 + \rho^z\gamma B_3^2 + \rho(-2\gamma B_1 B_1^z - 2\gamma B_2 B_2^z - \\ &- 2\gamma B_3 B_3^z) + \pi_1(2\pi_3^x - 2\gamma\pi_3^x + 2\pi_1^z - 2\gamma\pi_1^z) + \pi_2(2\pi_3^y - 2\gamma\pi_3^y + 2\pi_2^z - 2\gamma\pi_2^z) + \pi_3(2\pi_1^x - \\ &- 2\gamma\pi_1^x + 2\pi_2^y - 2\gamma\pi_2^y + 6\pi_3^z - 6\gamma\pi_3^z))) \\ \mathcal{O}_{85} &= \frac{1}{\rho^2} (2\rho^x\gamma B_1\pi_1 + 2\rho^y\gamma B_1\pi_2 + 2\rho^z\gamma B_1\pi_3 + \rho(-2\gamma\pi_1 B_1^x - 2\gamma\pi_2 B_1^y - 2\gamma\pi_3 B_1^z + \\ &+ \rho(2E_3^y - 2E_2^z) + B_1(-2\gamma\pi_1^x - 2\gamma\pi_2^y - 2\gamma\pi_3^z))) \\ \mathcal{O}_{86} &= \frac{1}{\rho^2} (2\rho^x\gamma B_2\pi_1 + 2\rho^y\gamma B_2\pi_2 + 2\rho^z\gamma B_2\pi_3 + \rho(-2\gamma\pi_1 B_2^x - 2\gamma\pi_2 B_2^y - 2\gamma\pi_3 B_2^z + \\ &+ \rho(-2E_3^x + 2E_1^z) + B_2(-2\gamma\pi_1^x - 2\gamma\pi_2^y - 2\gamma\pi_3^z))) \\ \mathcal{O}_{87} &= \frac{1}{\rho^2} (2\rho^x\gamma B_3\pi_1 + 2\rho^y\gamma B_3\pi_2 + 2\rho^z\gamma B_3\pi_3 + \rho(-2\gamma\pi_1 B_3^x - 2\gamma\pi_2 B_3^y + \rho(2E_2^x - 2E_1^y) - \\ &- 2\gamma\pi_3 B_3^z + B_3(-2\gamma\pi_1^x - 2\gamma\pi_2^y - 2\gamma\pi_3^z))) \\ \mathcal{O}_{88} &= \frac{1}{\theta \Delta t} + \frac{1}{\rho^2} (-\rho^x\gamma\pi_1 - \rho^y\gamma\pi_2 - \rho^z\gamma\pi_3 + \rho(\gamma\pi_1^x + \gamma\pi_2^y + \gamma\pi_3^z)) \\ \mathcal{O}_{89} &= 2B_2^z - 2B_3^y \\ \mathcal{O}_{810} &= 2B_3^x - 2B_1^z \\ \mathcal{O}_{811} &= 2B_1^y - 2B_2^x \end{aligned}$$

$$\mathcal{O}_{91} = \frac{B_3\pi_2 - B_2\pi_3}{\rho^2}$$

$$\mathcal{O}_{92} = 0$$

$$\mathcal{O}_{93} = -\frac{B_3}{\rho}$$

$$\mathcal{O}_{94} = \frac{B_2}{\rho}$$

$$\mathcal{O}_{95} = 0$$

$$\mathcal{O}_{96} = \frac{\pi_3}{\rho}$$

$$\mathcal{O}_{97} = -\frac{\pi_2}{\rho}$$

$$\mathcal{O}_{98} = 0$$

$$\mathcal{O}_{99} = -1$$

$$\mathcal{O}_{910} = 0, \quad \mathcal{O}_{911} = 0$$

$$\mathcal{O}_{101} = \frac{B_3\pi_1 - B_1\pi_3}{\rho^2}$$

$$\mathcal{O}_{102} = -\frac{B_3}{\rho}$$

$$\mathcal{O}_{103} = 0$$

$$\mathcal{O}_{104} = \frac{B_1}{\rho}$$

$$\begin{aligned}\mathcal{O}_{10\,5} &= \frac{\pi_3}{\rho} \\ \mathcal{O}_{10\,6} &= 0 \\ \mathcal{O}_{10\,7} &= -\frac{\pi_1}{\rho} \\ \mathcal{O}_{10\,8} &= 0, \quad \mathcal{O}_{10\,9} = 0 \\ \mathcal{O}_{10\,10} &= -1 \\ \mathcal{O}_{10\,11} &= 0\end{aligned}$$

$$\begin{aligned}\mathcal{O}_{11\,1} &= \frac{B_2\pi_1 - B_1\pi_2}{\rho^2} \\ \mathcal{O}_{11\,2} &= -\frac{B_2}{\rho} \\ \mathcal{O}_{11\,3} &= \frac{B_1}{\rho} \\ \mathcal{O}_{11\,4} &= 0 \\ \mathcal{O}_{11\,5} &= \frac{\pi_2}{\rho} \\ \mathcal{O}_{11\,6} &= -\frac{\pi_1}{\rho} \\ \mathcal{O}_{11\,7} &= 0 \\ \mathcal{O}_{11\,8} \dots \mathcal{O}_{11\,10} &= 0 \\ \mathcal{O}_{11\,11} &= -1\end{aligned}$$

$$\mathcal{P}_{1\,1} = 0, \quad \mathcal{P}_{1\,2} = 1, \quad \mathcal{P}_{1\,2} \dots \mathcal{P}_{1\,11} = 0$$

$$\begin{aligned}\mathcal{P}_{2\,1} &= \frac{1}{2\rho^2}((-3 + \gamma)\pi_1^2 + (-1 + \gamma)\pi_2^2 + (-1 + \gamma)\pi_3^2) \\ \mathcal{P}_{2\,2} &= \frac{(3 - \gamma)\pi_1}{\rho} \\ \mathcal{P}_{2\,3} &= \frac{(1 - \gamma)\pi_2}{\rho} \\ \mathcal{P}_{2\,4} &= \frac{(1 - \gamma)\pi_3}{\rho} \\ \mathcal{P}_{2\,5} &= -\gamma B_1 \\ \mathcal{P}_{2\,6} &= (2 - \gamma)B_2 \\ \mathcal{P}_{2\,7} &= (2 - \gamma)B_3 \\ \mathcal{P}_{2\,8} &= \frac{\gamma - 1}{2} \\ \mathcal{P}_{2\,9} \dots \mathcal{P}_{2\,11} &= 0\end{aligned}$$

$$\begin{aligned}\mathcal{P}_{3\,1} &= -\frac{\pi_1\pi_2}{\rho^2} \\ \mathcal{P}_{3\,2} &= \frac{\pi_2}{\rho} \\ \mathcal{P}_{3\,3} &= \frac{\pi_1}{\rho} \\ \mathcal{P}_{3\,4} &= 0 \\ \mathcal{P}_{3\,5} &= -B_2 \\ \mathcal{P}_{3\,6} &= -B_1 \\ \mathcal{P}_{3\,7} \dots \mathcal{P}_{3\,11} &= 0\end{aligned}$$

$$\begin{aligned}\mathcal{P}_{4\,1} &= -\frac{\pi_1\pi_3}{\rho^2} \\ \mathcal{P}_{4\,2} &= \frac{\pi_3}{\rho} \\ \mathcal{P}_{4\,3} &= 0 \\ \mathcal{P}_{4\,4} &= \frac{\pi_1}{\rho} \\ \mathcal{P}_{4\,5} &= -B_3 \\ \mathcal{P}_{4\,6} &= 0 \\ \mathcal{P}_{4\,7} &= -B_1 \\ \mathcal{P}_{4\,8} \dots \mathcal{P}_{4\,11} &= 0\end{aligned}$$

$$\mathcal{P}_{5\,1} \dots \mathcal{P}_{5\,11} = 0$$

$$\mathcal{P}_{61} \dots \mathcal{P}_{610} = 0, \quad \mathcal{P}_{611} = -1$$

$$\mathcal{P}_{71} \dots \mathcal{P}_{79} = 0, \quad \mathcal{P}_{710} = -1, \quad \mathcal{P}_{711} = 0$$

$$\begin{aligned}\mathcal{P}_{81} &= \frac{1}{\rho^3}(\rho(-U\gamma + \gamma B_1^2 + \gamma B_2^2 + \gamma B_3^2)\pi_1 + \pi_1((-2+2\gamma)\pi_1^2 + (-2+2\gamma)\pi_2^2 + (-2+2\gamma)\pi_3^2)) \\ \mathcal{P}_{82} &= \frac{1}{\rho^2}(\rho(U\gamma - \gamma B_1^2 - \gamma B_2^2 - \gamma B_3^2) + (3-3\gamma)\pi_1^2 + (1-\gamma)\pi_2^2 + (1-\gamma)\pi_3^2) \\ \mathcal{P}_{83} &= \frac{1}{\rho^2}((2-2\gamma)\pi_1\pi_2) \\ \mathcal{P}_{84} &= \frac{1}{\rho^2}((2-2\gamma)\pi_1\pi_3) \\ \mathcal{P}_{85} &= -\frac{1}{\rho^2}(2\gamma B_1\pi_1) \\ \mathcal{P}_{86} &= \frac{1}{\rho^2}(-2\rho E_3 - 2\gamma B_2\pi_1) \\ \mathcal{P}_{87} &= \frac{1}{\rho^2}(2\rho E_2 - 2\gamma B_3\pi_1) \\ \mathcal{P}_{88} &= \frac{\gamma\pi_1}{\rho^2} \\ \mathcal{P}_{89} &= 0 \\ \mathcal{P}_{810} &= 2B_3 \\ \mathcal{P}_{89} &= -2B_2\end{aligned}$$

$$\mathcal{P}_{91} \dots \mathcal{P}_{911} = 0$$

$$\mathcal{P}_{101} \dots \mathcal{P}_{106} = 0, \quad \mathcal{P}_{107} = -\eta, \quad \mathcal{P}_{108} \dots \mathcal{P}_{1011} = 0$$

$$\mathcal{P}_{111} \dots \mathcal{P}_{115} = 0, \quad \mathcal{P}_{116} = \eta, \quad \mathcal{P}_{117} \dots \mathcal{P}_{1111} = 0$$

$$\mathcal{Q}_{11} = 0, \quad \mathcal{Q}_{12} = 0, \quad \mathcal{Q}_{13} = 1, \quad \mathcal{Q}_{14} \dots \mathcal{Q}_{111} = 0$$

$$\begin{aligned}\mathcal{Q}_{21} &= -\frac{\pi_1\pi_2}{\rho^2} \\ \mathcal{Q}_{22} &= \frac{\pi_2}{\rho} \\ \mathcal{Q}_{23} &= \frac{\rho}{\pi_1} \\ \mathcal{Q}_{24} &= 0 \\ \mathcal{Q}_{25} &= -B_2 \\ \mathcal{Q}_{26} &= -B_1 \\ \mathcal{Q}_{27} \dots \mathcal{Q}_{211} &= 0\end{aligned}$$

$$\begin{aligned}\mathcal{Q}_{31} &= \frac{1}{2\rho^2}((-1+\gamma)\pi_1^2 + (-3+\gamma)\pi_2^2 + (-1+\gamma)\pi_3^2) \\ \mathcal{Q}_{32} &= \frac{(1-\gamma)\pi_1}{\rho} \\ \mathcal{Q}_{33} &= \frac{(3-\gamma)\pi_2}{\rho} \\ \mathcal{Q}_{34} &= \frac{(1-\gamma)\pi_3}{\rho} \\ \mathcal{Q}_{35} &= (2-\gamma)\gamma B_1 \\ \mathcal{Q}_{36} &= -\gamma B_2 \\ \mathcal{Q}_{37} &= (2-\gamma)B_3 \\ \mathcal{Q}_{38} &= \frac{\gamma-1}{2} \\ \mathcal{Q}_{39} \dots \mathcal{Q}_{211} &= 0\end{aligned}$$

$$\begin{aligned}\mathcal{Q}_{41} &= -\frac{\pi_2\pi_3}{\rho^2} \\ \mathcal{Q}_{42} &= 0 \\ \mathcal{Q}_{43} &= \frac{\pi_3}{\rho} \\ \mathcal{Q}_{44} &= \frac{\rho}{\pi_2} \\ \mathcal{Q}_{45} &= 0 \\ \mathcal{Q}_{46} &= -B_3\end{aligned}$$

$$\mathcal{Q}_{47} = -B_2$$

$$\mathcal{Q}_{48} \dots \mathcal{Q}_{411} = 0$$

$$\mathcal{Q}_{51} \dots \mathcal{Q}_{510} = 0 , \quad \mathcal{Q}_{511} = 1$$

$$\mathcal{Q}_{61} \dots \mathcal{Q}_{611} = 0$$

$$\mathcal{Q}_{71} \dots \mathcal{Q}_{78} = 0 , \quad \mathcal{Q}_{79} = -1 , \quad \mathcal{Q}_{710} = 0 , \quad \mathcal{Q}_{711} = 0$$

$$\mathcal{Q}_{81} = \frac{1}{\rho^3}(\rho(-U\gamma + \gamma B_1^2 + \gamma B_2^2 + \gamma B_3^2)\pi_2 + (-2 + 2\gamma)\pi_1^2\pi_2 + \pi_2((-2 + 2\gamma)\pi_2^2 + (-2 + 2\gamma)\pi_3^2))$$

$$\mathcal{Q}_{82} = \frac{1}{\rho^2}((2 - 2\gamma)\pi_1\pi_2)$$

$$\mathcal{Q}_{83} = \frac{1}{\rho^2}(\rho(U\gamma - \gamma B_1^2 - \gamma B_2^2 - \gamma B_3^2) + (1 - \gamma)\pi_1^2 + (3 - 3\gamma)\pi_2^2 + (1 - \gamma)\pi_3^2)$$

$$\mathcal{Q}_{84} = \frac{1}{\rho^2}((2 - 2\gamma)\pi_2\pi_3)$$

$$\mathcal{Q}_{85} = \frac{1}{\rho^2}(2\rho E_3 - 2\gamma B_1\pi_2)$$

$$\mathcal{Q}_{86} = -\frac{1}{\rho^2}(2\gamma B_2\pi_2)$$

$$\mathcal{Q}_{87} = \frac{1}{\rho^2}(-2\rho E_1 - 2\gamma B_3\pi_2)$$

$$\mathcal{Q}_{88} = \frac{\gamma\pi_2}{\rho^2}$$

$$\mathcal{Q}_{89} = -2B_3$$

$$\mathcal{Q}_{810} = 0$$

$$\mathcal{Q}_{89} = 2B_1$$

$$\mathcal{Q}_{91} \dots \mathcal{Q}_{95} = 0 , \quad \mathcal{Q}_{96} = \eta , \quad \mathcal{Q}_{97} \dots \mathcal{Q}_{911} = 0$$

$$\mathcal{Q}_{101} \dots \mathcal{Q}_{1011} = 0$$

$$\mathcal{Q}_{111} \dots \mathcal{Q}_{114} = 0 , \quad \mathcal{Q}_{115} = -\eta , \quad \mathcal{Q}_{116} \dots \mathcal{Q}_{1111} = 0$$

$$\mathcal{R}_{11} \dots \mathcal{R}_{13} = 0 , \quad \mathcal{R}_{14} = 1 , \quad \mathcal{R}_{15} \dots \mathcal{R}_{111} = 0$$

$$\mathcal{R}_{21} = -\frac{\pi_1\pi_3}{\rho^2}$$

$$\mathcal{R}_{22} = \frac{\pi_3}{\rho}$$

$$\mathcal{R}_{23} = 0$$

$$\mathcal{R}_{24} = \frac{\pi_1}{\rho}$$

$$\mathcal{R}_{25} = -B_3$$

$$\mathcal{R}_{26} = 0$$

$$\mathcal{R}_{27} = -B_1$$

$$\mathcal{R}_{28} \dots \mathcal{R}_{211} = 0$$

$$\mathcal{R}_{31} = -\frac{\pi_2\pi_3}{\rho^2}$$

$$\mathcal{R}_{32} = 0$$

$$\mathcal{R}_{33} = \frac{\pi_3}{\rho}$$

$$\mathcal{R}_{34} = \frac{\pi_2}{\rho}$$

$$\mathcal{R}_{35} = 0$$

$$\mathcal{R}_{36} = -B_3$$

$$\mathcal{R}_{37} = -B_2$$

$$\mathcal{R}_{38} \dots \mathcal{R}_{311} = 0$$

$$\mathcal{R}_{41} = \frac{1}{2\rho^2}((-1 + \gamma)\pi_1^2 + (-1 + \gamma)\pi_2^2 + (-3 + \gamma)\pi_3^2)$$

$$\begin{aligned}
\mathcal{R}_{42} &= \frac{(1-\gamma)\pi_1}{\rho} \\
\mathcal{R}_{43} &= \frac{(1-\gamma)\pi_2}{\rho} \\
\mathcal{R}_{44} &= \frac{(3-\gamma)\pi_3}{\rho} \\
\mathcal{R}_{45} &= (2-\gamma)\gamma B_1 \\
\mathcal{R}_{46} &= (2-\gamma)B_2 \\
\mathcal{R}_{47} &= -\gamma B_3 \\
\mathcal{R}_{48} &= \frac{\gamma-1}{2} \\
\mathcal{R}_{49} \dots \mathcal{R}_{211} &= 0
\end{aligned}$$

$$\mathcal{R}_{51} \dots \mathcal{R}_{59} = 0, \quad \mathcal{R}_{510} = -1, \quad \mathcal{R}_{511} = 0$$

$$\mathcal{R}_{61} \dots \mathcal{R}_{68} = 0, \quad \mathcal{R}_{69} = 1, \quad \mathcal{R}_{610} = 0, \quad \mathcal{R}_{611} = 0$$

$$\mathcal{R}_{71} \dots \mathcal{R}_{711} = 0$$

$$\begin{aligned}
\mathcal{R}_{81} &= \frac{1}{\rho^3}(\rho(-U\gamma + \gamma B_1^2 + \gamma B_2^2 + \gamma B_3^2)\pi_3 + (-2 + 2\gamma)\pi_1^2\pi_3 + (-2 + 2\gamma)\pi_2^2\pi_3 + (-2 + 2\gamma)\pi_3^3) \\
\mathcal{R}_{82} &= \frac{1}{\rho^2}((2 - 2\gamma)\pi_1\pi_3) \\
\mathcal{R}_{83} &= \frac{1}{\rho^2}((2 - 2\gamma)\pi_2\pi_3) \\
\mathcal{R}_{84} &= \frac{1}{\rho^2}(\rho(U\gamma - \gamma B_1^2 - \gamma B_2^2 - \gamma B_3^2) + (1 - \gamma)\pi_1^2 + (1 - \gamma)\pi_2^2 + (3 - 3\gamma)\pi_3^2) \\
\mathcal{R}_{85} &= \frac{1}{\rho^2}(-2\rho E_2 - 2\gamma B_1\pi_3) \\
\mathcal{R}_{86} &= \frac{1}{\rho^2}(2\rho E_1 - 2\gamma B_2\pi_3) \\
\mathcal{R}_{87} &= -\frac{1}{\rho^2}(2\gamma B_3\pi_3) \\
\mathcal{R}_{88} &= \frac{\gamma\pi_3}{\rho^2} \\
\mathcal{R}_{89} &= 2B_2 \\
\mathcal{R}_{810} &= -2B_1 \\
\mathcal{R}_{89} &= 0
\end{aligned}$$

$$\mathcal{R}_{91} \dots \mathcal{R}_{95} = 0, \quad \mathcal{R}_{96} = -\eta, \quad \mathcal{R}_{97} \dots \mathcal{R}_{911} = 0$$

$$\mathcal{R}_{101} \dots \mathcal{R}_{104} = 0, \quad \mathcal{R}_{105} = \eta, \quad \mathcal{R}_{106} \dots \mathcal{R}_{1011} = 0$$

$$\mathcal{R}_{111} \dots \mathcal{R}_{1111} = 0$$

The corresponding right hand side from the equation (4.65) can be separated into two parts $\mathbf{f} = \Delta t(\theta \mathbf{h} + (1 - \theta)\bar{\mathbf{h}})$. The first one \mathbf{h} is part of linearization and second $\bar{\mathbf{h}}$ is old time contribution from time discretization.

$$\begin{aligned}
h_1 &= 0 \\
h_2 &= B_2(2B_2^x - \gamma B_2^x - B_1^y) + B_3(2B_3^x - \gamma B_3^x - B_1^z) + B_1(-\gamma B_1^x - B_2^y - B_3^z) \\
h_3 &= B_1(-B_2^x + 2B_1^y - \gamma B_1^y) + B_3(2B_3^y - \gamma B_3^y - B_2^z) + B_2(-B_1^x - \gamma B_2^y - B_3^z) \\
h_4 &= B_1(-B_3^x + 2B_1^z - \gamma B_1^z) + B_2(-B_3^y + 2B_2^z - \gamma B_2^z) + B_3(-B_1^x - B_2^y - \gamma B_3^z) \\
h_5 &= 0 \\
h_6 &= 0 \\
h_7 &= 0 \\
h_8 &= \frac{1}{\rho^2}((\rho^x\gamma B_1^2 + \rho^x\gamma B_2^2 + \rho^x\gamma B_3^2)\pi_1 + (\rho^y\gamma B_1^2 + \rho^y\gamma B_2^2 + \rho^y\gamma B_3^2)\pi_2 + (\rho^z\gamma B_1^2 + \rho^z\gamma B_2^2 + \rho^z\gamma B_3^2)\pi_3 + \rho(\pi_1(-2\gamma B_1 B_1^x - 2\gamma B_2 B_2^x - 2\gamma B_3 B_3^x) + \pi_2(-2\gamma B_1 B_1^y - 2\gamma B_2 B_2^y - 2\gamma B_3 B_3^y) + \pi_3(-2\gamma B_1 B_1^z - 2\gamma B_2 B_2^z - 2\gamma B_3 B_3^z)) + \rho(E_3(-2B_2^x + 2B_1^y) + B_3(2E_2^x - 2E_1^y) + E_2(2B_3^x - 2B_1^z) + E_1(-2B_3^y + 2B_2^z) + B_2(-2E_3^x + 2E_1^z) + B_1(2E_3^y - 2E_2^z)) + B_1^2(-\gamma\pi_1^x - \gamma\pi_2^y - \gamma\pi_3^z) + B_2^2(-\gamma\pi_1^x - \gamma\pi_2^y - \gamma\pi_3^z) + B_3^2(-\gamma\pi_1^x - \gamma\pi_2^y - \gamma\pi_3^z))) \\
h_9 \dots h_{11} &= 0
\end{aligned}$$

$$\begin{aligned}
\bar{h}_1 &= \frac{\rho}{(1-\theta)\Delta t} - \pi_1^x - \pi_2^y - \pi_3^z \\
\bar{h}_2 &= \frac{\pi_1}{(1-\theta)\Delta t} + (1/(2\rho^2))((\rho^x - \rho^x\gamma)\pi_2^2 + (\rho^x - \rho^x\gamma)\pi_3^2 + \pi_1((3\rho^x - \rho^x\gamma)\pi_1 + 2\rho^y\pi_2 + 2\rho^z\pi_3) + \\
&\quad + \rho(\pi_2(-2\pi_2^x + 2\gamma\pi_2^x - 2\pi_1^y) + \rho(xU - xU\gamma + B_2(-4B_2^x + 2\gamma B_2^x + 2B_2^y) + B_3(-4B_3^x + 2\gamma B_3^x + \\
&\quad + 2B_3^z) + B_1(2\gamma B_1^x + 2B_1^y + 2B_1^z)) + \pi_3(-2\pi_3^x + 2\gamma\pi_3^x - 2\pi_1^z) + \pi_1(-6\pi_1^x + 2\gamma\pi_1^x - 2\pi_2^y - 2\pi_3^z))) \\
\bar{h}_3 &= \frac{\pi_2}{(1-\theta)\Delta t} + (1/(2\rho^2))(\pi_1((\rho^y - \rho^y\gamma)\pi_1 + 2\rho^x\pi_2) + (\rho^y - \rho^y\gamma)\pi_3^2 + \pi_2((3\rho^y - \rho^y\gamma)\pi_2 + 2\rho^z\pi_3) + \\
&\quad + \rho(\pi_1(-2\pi_2^x - 2\pi_1^y + 2\gamma\pi_1^y) + \rho(yU - yU\gamma + B_1(2B_2^x - 4B_1^y + 2\gamma B_1^y) + B_3(-4B_3^y + 2\gamma B_3^y + \\
&\quad + 2B_3^z) + B_2(2B_1^x + 2\gamma B_1^y + 2B_2^z)) + \pi_3(-2\pi_3^y + 2\gamma\pi_3^y - 2\pi_2^z) + \pi_2(-2\pi_1^x - 6\pi_2^y + 2\gamma\pi_2^y - 2\pi_3^z))) \\
\bar{h}_4 &= \frac{\pi_3}{(1-\theta)\Delta t} + (1/(2\rho^2))((3\rho^z - \rho^z\gamma)\pi_3^2 + \pi_1((\rho^z - \rho^z\gamma)\pi_1 + 2\rho^x\pi_3) + \pi_2((\rho^z - \rho^z\gamma)\pi_2 + 2\rho^y\pi_3) + \\
&\quad + \rho(\rho(zU - zU\gamma + B_1(2B_3^x - 4B_1^z + 2\gamma B_1^z) + B_2(2B_3^y - 4B_2^z + 2\gamma B_2^z) + B_3(2B_1^x + 2B_2^y + 2\gamma B_3^z)) + \\
&\quad + \pi_1(-2\pi_3^x - 2\pi_1^z + 2\gamma\pi_1^z) + \pi_2(-2\pi_3^y - 2\pi_2^z + 2\gamma\pi_2^z) + \pi_3(-2\pi_1^x - 2\pi_2^y - 6\pi_3^z + 2\gamma\pi_3^z))) \\
\bar{h}_5 &= \frac{B_1}{(1-\theta)\Delta t} - E_3^y + E_2^z \\
\bar{h}_6 &= \frac{B_2}{(1-\theta)\Delta t} + E_3^x - E_1^z \\
\bar{h}_7 &= \frac{B_3}{(1-\theta)\Delta t} - E_2^x + E_1^y \\
\bar{h}_8 &= \frac{U}{(1-\theta)\Delta t} + (1/(\rho^3))((2\rho^z - 2\rho^z\gamma)\pi_3^3 + \pi_2((2\rho^y - 2\rho^y\gamma)\pi_3^2 + \pi_2((2\rho^y - 2\rho^y\gamma)\pi_2 + (2\rho^z - \\
&\quad - 2\rho^z\gamma)\pi_3)) + \pi_1((2\rho^x - 2\rho^x\gamma)\pi_2^2 + (2\rho^x - 2\rho^x\gamma)\pi_3^2 + \pi_1((2\rho^x - 2\rho^x\gamma)\pi_1 + (2\rho^y - 2\rho^y\gamma)\pi_2 + \\
&\quad + (2\rho^z - 2\rho^z\gamma)\pi_3)) + \rho(\rho(\pi_1(-xU\gamma + 2\gamma B_1 B_1^x + 2\gamma B_2 B_2^x + 2\gamma B_3 B_3^x) + \pi_2(-yU\gamma + 2\gamma B_1 B_1^y + \\
&\quad + 2\gamma B_2 B_2^y + 2\gamma B_3 B_3^y) + \pi_3(-zU\gamma + 2\gamma B_1 B_1^z + 2\gamma B_2 B_2^z + 2\gamma B_3 B_3^z) + \rho(E_3(2B_2^x - 2B_1^y) + \\
&\quad + B_3(-2E_2^x + 2E_1^y) + E_2(-2B_3^x + 2B_1^z) + E_1(2B_3^y - 2B_2^z) + B_2(2E_3^x - 2E_1^z) + B_1(-2E_3^y + \\
&\quad + 2E_2^z)) + U(-\gamma\pi_1^x - \gamma\pi_2^y - \gamma\pi_3^z) + B_1^2(\gamma\pi_1^x + \gamma\pi_2^y + \gamma\pi_3^z) + B_2^2(\gamma\pi_1^x + \gamma\pi_2^y + \gamma\pi_3^z) + B_3^2(\gamma\pi_1^x + \\
&\quad + \gamma\pi_2^y + \gamma\pi_3^z)) + \pi_1(U\rho^x\gamma - \rho^x\gamma B_1^2 - \rho^x\gamma B_2^2 - \rho^x\gamma B_3^2 + \pi_2(-2\pi_2^x + 2\gamma\pi_2^x - 2\pi_1^y + 2\gamma\pi_1^y) + \\
&\quad + \pi_3(-2\pi_3^x + 2\gamma\pi_3^x - 2\pi_1^z + 2\gamma\pi_1^z) + \pi_1(-3\pi_1^x + 3\gamma\pi_1^x - \pi_2^y + \gamma\pi_2^y - \pi_3^z + \gamma\pi_3^z)) + \pi_2(U\rho^y\gamma - \\
&\quad - \rho^y\gamma B_1^2 - \rho^y\gamma B_2^2 - \rho^y\gamma B_3^2 + \pi_3(-2\pi_3^y + 2\gamma\pi_3^y - 2\pi_2^z + 2\gamma\pi_2^z) + \pi_2(-\pi_1^x + \gamma\pi_1^x - 3\pi_2^y + 3\gamma\pi_2^y - \\
&\quad - \pi_3^z + \gamma\pi_3^z)) + \pi_3(U\rho^z\gamma - \rho^z\gamma B_1^2 - \rho^z\gamma B_2^2 - \rho^z\gamma B_3^2 + \pi_3(-\pi_1^x + \gamma\pi_1^x - \pi_2^y + \gamma\pi_2^y - 3\pi_3^z + 3\gamma\pi_3^z))) \\
\bar{h}_9 \dots \bar{h}_{11} &= 0
\end{aligned}$$

7.6 Table of basis functions

In the section 4.8 we introduced derivation of Lagrange interpolation functions. In this part we present shape functions for several orders of interpolation polynomials.

The first order basis functions are following

$$\phi_1 = l_1 \quad \phi_2 = l_2 \quad \phi_3 = l_3$$

The second order basis functions are

$$\begin{aligned}
\phi_1 &= (2l_1 - 1)l_1 & \phi_2 &= (2l_2 - 1)l_2 & \phi_3 &= (2l_3 - 1)l_3 \\
\phi_4 &= 4l_1 l_2 & \phi_5 &= 4l_2 l_3 & \phi_6 &= 4l_1 l_3
\end{aligned}$$

The third order basis functions are

$$\begin{aligned}
\phi_1 &= \frac{1}{2}(3l_1 - 1)(3l_1 - 2)l_1 & \phi_2 &= \frac{1}{2}(3l_2 - 1)(3l_2 - 2)l_2 & \phi_3 &= \frac{1}{2}(3l_3 - 1)(3l_3 - 2)l_3 \\
\phi_4 &= \frac{9}{2}l_1 l_2 (3l_1 - 1) & \phi_5 &= \frac{9}{2}l_1 l_2 (3l_2 - 1) & \phi_6 &= \frac{9}{2}l_2 l_3 (3l_2 - 1) \\
\phi_7 &= \frac{9}{2}l_2 l_3 (3l_3 - 1) & \phi_8 &= \frac{9}{2}l_1 l_3 (3l_3 - 1) & \phi_9 &= \frac{9}{2}l_1 l_3 (3l_1 - 1) \\
\phi_{10} &= 27l_1 l_2 l_3
\end{aligned}$$

The fourth order basis functions are

$$\begin{aligned}
\phi_1 &= \frac{1}{3}l_1(4l_1 - 1)(2l_1 - 1)(4l_1 - 3) & \phi_2 &= \frac{1}{3}l_2(4l_2 - 1)(2l_2 - 1)(4l_2 - 3) \\
\phi_3 &= \frac{1}{3}l_3(4l_3 - 1)(2l_3 - 1)(4l_3 - 3) & \phi_4 &= \frac{16}{3}l_1l_2(4l_1 - 1)(2l_1 - 1) \\
\phi_5 &= 4l_1l_2(4l_1 - 1)(4l_2 - 1) & \phi_6 &= \frac{16}{3}l_1l_2(4l_2 - 1)(2l_2 - 1) \\
\phi_7 &= \frac{16}{3}l_2l_3(4l_2 - 1)(2l_2 - 1) & \phi_8 &= 4l_2l_3(4l_2 - 1)(4l_3 - 1) \\
\phi_9 &= \frac{16}{3}l_2l_3(4l_3 - 1)(2l_3 - 1) & \phi_{10} &= \frac{16}{3}l_1l_3(4l_3 - 1)(2l_3 - 1) \\
\phi_{11} &= 4l_1l_3(4l_1 - 1)(4l_3 - 1) & \phi_{12} &= \frac{16}{3}l_1l_3(4l_1 - 1)(2l_1 - 1) \\
\phi_{13} &= 32l_1l_2l_3(4l_1 - 1) & \phi_{14} &= 32l_1l_2l_3(4l_2 - 1) \\
\phi_{15} &= 32l_1l_2l_3(4l_3 - 1)
\end{aligned}$$

The fifth order basis functions are

$$\begin{aligned}
\phi_1 &= \frac{1}{120}l_1(5l_1 - 1)(5l_1 - 1)(5l_1 - 3)(5l_1 - 4) & \phi_2 &= \frac{1}{120}l_2(5l_2 - 1)(5l_2 - 1)(5l_2 - 3)(5l_2 - 4) \\
\phi_3 &= \frac{1}{120}l_1(5l_3 - 1)(5l_3 - 1)(5l_3 - 3)(5l_3 - 4) & \phi_4 &= \frac{25}{24}l_1l_2(5l_1 - 1)(5l_1 - 2)(5l_1 - 3) \\
\phi_5 &= \frac{25}{12}l_1l_2(5l_1 - 1)(5l_1 - 2)(5l_2 - 1) & \phi_6 &= \frac{25}{12}l_1l_2(5l_1 - 1)(5l_2 - 1)(5l_2 - 2) \\
\phi_7 &= \frac{25}{24}l_1l_2(5l_2 - 1)(5l_2 - 2)(5l_2 - 3) & \phi_8 &= \frac{25}{24}l_2l_3(5l_2 - 1)(5l_2 - 2)(5l_2 - 3) \\
\phi_9 &= \frac{25}{12}l_2l_3(5l_2 - 1)(5l_2 - 2)(5l_3 - 1) & \phi_{10} &= \frac{25}{12}l_2l_3(5l_2 - 1)(5l_3 - 1)(5l_3 - 2) \\
\phi_{11} &= \frac{25}{24}l_3l_2(5l_3 - 1)(5l_3 - 2)(5l_3 - 3) & \phi_{12} &= \frac{25}{24}l_1l_3(5l_3 - 1)(5l_3 - 2)(5l_3 - 3) \\
\phi_{13} &= \frac{25}{12}l_1l_3(5l_3 - 1)(5l_3 - 2)(5l_1 - 1) & \phi_{14} &= \frac{25}{12}l_1l_3(5l_3 - 1)(5l_1 - 1)(5l_1 - 2) \\
\phi_{15} &= \frac{25}{24}l_1l_3(5l_1 - 1)(5l_1 - 2)(5l_1 - 3) & \phi_{16} &= \frac{125}{6}l_1l_2l_3(5l_1 - 1)(5l_1 - 2) \\
\phi_{17} &= \frac{125}{4}l_1l_2l_3(5l_1 - 1)(5l_2 - 1) & \phi_{18} &= \frac{125}{6}l_1l_2l_3(5l_2 - 1)(5l_2 - 2) \\
\phi_{19} &= \frac{125}{4}l_1l_2l_3(5l_2 - 1)(5l_3 - 1) & \phi_{20} &= \frac{125}{6}l_1l_2l_3(5l_3 - 1)(5l_3 - 2) \\
\phi_{21} &= \frac{125}{4}l_1l_2l_3(5l_1 - 1)(5l_3 - 1)
\end{aligned}$$

Bibliography

- Aschwanden, M., 2005. Physics of the Solar Corona. Springer.
- Aschwanden, M. J., 2007. From solar nanoflares to stellar giant flares: Scaling laws and non-implications for coronal heating. *Advances in Space Research* 39, 1867–1875.
- Bak, P., Tang, C., Wiesenfeld, K., Jul. 1987. Self-organized criticality - An explanation of 1/f noise. *Physical Review Letters* 59, 381–384.
- Bárta, M., Büchner, J., Karlický, M., Jan. 2010. Multi-scale MHD approach to the current sheet filamentation in solar coronal reconnection. *Advances in Space Research* 45, 10–17.
- Bárta, M., Büchner, J., Karlický, M., Kotrč, P., Mar. 2011a. Spontaneous Current-layer Fragmentation and Cascading Reconnection in Solar Flares. II. Relation to Observations. *ApJ730*, 47.
- Bárta, M., Büchner, J., Karlický, M., Skála, J., Aug. 2011b. Spontaneous Current-layer Fragmentation and Cascading Reconnection in Solar Flares. I. Model and Analysis. *ApJ737*, 24.
- Bárta, M., Karlický, M., Žemlička, R., Dec. 2008. Plasmoid Dynamics in Flare Reconnection and the Frequency Drift of the Drifting Pulsating Structure. *Sol. Phys.* 253, 173–189.
- Bhattacharjee, A., Huang, Y., Yang, H., Rogers, B., Nov. 2009. Fast reconnection in high-Lundquist-number plasmas due to the plasmoid Instability. *Physics of Plasmas* 16 (11), 112102–+.
- Biskamp, D., Sep. 2000. Magnetic Reconnection in Plasmas.
- Bochev, P. P., Gunzburger, M. D., 2009. Least-Squares Finite Element Methods. Springer Science+Business Media, LLC, 233 Spring Street, New York, NY 10013, USA.
- Büchner, J., Jun. 2006. Theory and Simulation of Reconnection. *Space Science Reviews* 124, 345–360.
- Büchner, J., Elkina, N., Aug. 2006. Anomalous resistivity of current-driven isothermal plasmas due to phase space structuring. *Physics of Plasmas* 13 (8), 082304.1–9.
- Carmichael, H., 1964. A Process for Flares. NASA Special Publication 50, 451.
- Chen, F. F., 1984. Úvod do fyziky plazmatu. Academia Praha.
- Chung, T. J., Mar. 2002. "Computational Fluid Dynamics". Cambridge University Press.
- Cliver, E., Nov. 2000. Solar Flare Classification. IOP.
- Czaykowska, A., de Pontieu, B., Alexander, D., Rank, G., Aug. 1999. Evidence for Chromospheric Evaporation in the Late Gradual Flare Phase from SOHO/CDS Observations. *ApJ521*, L75–L78.

- Dai, W., Woodward, P. R., Feb. 1998. On the Divergence-free Condition and Conservation Laws in Numerical Simulations for Supersonic Magnetohydrodynamic Flows. *ApJ*494, 317.
- Dennis, J. E. J., Schmabel, R. B., 1996. Numerical Methods for Unconstrained Optimization and Nonlinear Equations. Soc for Industrial & Applied Math.
- Dere, K. P., Brueckner, G. E., Howard, R. A., Michels, D. J., Delaboudiniere, J. P., May 1999. LASCO and EIT Observations of Helical Structure in Coronal Mass Ejections. *ApJ*516, 465–474.
- Drake, J. F., Shay, M. A., Thongthai, W., Swisdak, M., Mar. 2005. Production of Energetic Electrons during Magnetic Reconnection. *Physical Review Letters* 94 (9), 095001.1–4.
- Emslie, A. G., Dennis, B. R., Holman, G. D., Hudson, H. S., Nov. 2005. Refinements to flare energy estimates: A followup to “Energy partition in two solar flare/CME events” by A. G. Emslie et al. *Journal of Geophysical Research (Space Physics)* 110, 11103.
- Forbes, T. G., Acton, L. W., Mar. 1996. Reconnection and Field Line Shrinkage in Solar Flares. *ApJ*459, 330.
- Furth, H. P., Killeen, J., Rosenbluth, M. N., Apr. 1963. Finite-Resistivity Instabilities of a Sheet Pinch. *Physics of Fluids* 6, 459–484.
- Galsgaard, K., Nordlund, Å., 1996. Coronal Heating by Flux Braiding. *Astrophysical Letters and Communications* 34, 175.
- Glasser, A. H., Tang, X. Z., Dec. 2004. The SEL macroscopic modeling code. *Computer Physics Communications* 164, 237–243.
- Goedbloed, J. P., Poedts, S., 2004. Principles of magnetohydrodynamics: with applications to laboratory and astrophysical plasmas. Cambridge University Press.
- Gopalswamy, N., Jul. 2007. Energetic Phenomena on the Sun. In: Hasan, S. S., Banerjee, D. (Eds.), Kodai School on Solar Physics. Vol. 919 of American Institute of Physics Conference Series. pp. 275–313.
- Gopalswamy, N., 2009. Coronal mass ejections and space weather. In: Tsuda, T., Fujii, R., Shibata, K., Geller, M. A. (Eds.), Climate and Weather of the Sun-Earth System (CAWSES) Selected Papers from the 2007 Kyoto Symposium. Edited by T. Tsuda, R. Fujii, K. Shibata, and M.A. Geller. Tokyo: TERRAPUB, 2009, p.77-120. pp. 77–120.
- Hanaoka, Y., Kurokawa, H., Enome, S., Nakajima, H., Shibasaki, K., Nishio, M., Takano, T., Torii, C., Sekiguchi, H., Kawashima, S., Bushimata, T., Shinohara, N., Irimajiri, Y., Koshiishi, H., Shiomi, Y., Nakai, Y., Funakoshi, Y., Kitai, R., Ishiura, K., Kimura, G., Apr. 1994. Simultaneous observations of a prominence eruption followed by a coronal arcade formation in radio, soft X-rays, and H(alpha). *PASJ*46, 205–216.
- Harra, L. K., Démoulin, P., Mandrini, C. H., Matthews, S. A., van Driel-Gesztelyi, L., Culhane, J. L., Fletcher, L., Aug. 2005. Flows in the solar atmosphere due to the eruptions on the 15th July, 2002. *A&A*438, 1099–1106.
- Hestenes, M. R., Stiefel, E., 1952. Methods of Conjugate Gradients for Solving Linear Systems. *JResNatBurStand* 49, 409–436.
- Hirayama, T., Feb. 1974. Theoretical Model of Flares and Prominences. I: Evaporating Flare Model. *Sol. Phys.*34, 323–338.

- Huang, Y., Bhattacharjee, A., Jun. 2010. Scaling laws of resistive magnetohydrodynamic reconnection in the high-Lundquist-number, plasmoid-unstable regime. *Physics of Plasmas* 17 (6), 062104–+.
- Hudson, H. S., Willson, R. C., Jul. 1983. Upper limits on the total radiant energy of solar flares. *Sol. Phys.* 86, 123–130.
- Isliker, H., Anastasiadis, A., Vlahos, L., Oct. 2001. MHD consistent cellular automata (CA) models. II. Applications to solar flares. *A&A*377, 1068–1080.
- Jardin, S. C., Breslau, J. A., May 2005. Implicit solution of the four-field extended-magnetohydrodynamic equations using high-order high-continuity finite elements. *Physics of Plasmas* 12 (5), 056101.
- Jiang, B., 1998. The Least-Squares Finite Element Method. Springer-Verlag Berlin Heidelberg, Springer-Verlag Berlin Heidelberg, Germany.
- Jiang, B.-N., Mar. 1993. Non-oscillatory and non-diffusive solution of convection problems by the iteratively reweighted least-squares finite element method. *J. Comput. Phys.* 105 (1), 108–121.
URL <http://dx.doi.org/10.1006/jcph.1993.1057>
- Karlický, M., Apr. 2004. Series of high-frequency slowly drifting structures mapping the flare magnetic field reconnection. *A&A*417, 325–332.
- Kirk, J. G., Melrose, D. B., Priest, E. R., 1994. Plasma Astrophysics. Springer-Verlag Berlin Heidelberg.
- Kliem, B., Karlický, M., Benz, A. O., Aug. 2000. Solar flare radio pulsations as a signature of dynamic magnetic reconnection. *A&A*360, 715–728.
- Kopp, R. A., Pneuman, G. W., Oct. 1976. Magnetic reconnection in the corona and the loop prominence phenomenon. *Sol. Phys.* 50, 85–98.
- Kracík, J., Tobiáš, J., 1966. Fyzika plazmatu. Academia Praha.
- Lazarian, A., Vishniac, E. T., Jun. 1999. Reconnection in a Weakly Stochastic Field. *ApJ*517, 700–718.
- Loureiro, N. F., Schekochihin, A. A., Cowley, S. C., Oct. 2007. Instability of current sheets and formation of plasmoid chains. *Physics of Plasmas* 14 (10), 100703–+.
- Lukin, V. S., Jan. 2008. Computational study of the internal kink mode evolution and associated magnetic reconnection phenomena. Ph.D. thesis, Princeton University, Princeton, New Jersey 08544 USA.
- Magara, T., Mineshige, S., Yokoyama, T., Shibata, K., Aug. 1996. Numerical Simulation of Magnetic Reconnection in Eruptive Flares. *ApJ*466, 1054–1066.
- Mandrini, C. H., Feb. 2010. Magnetic energy release: flares and coronal mass ejections. In: A. G. Kosovichev, A. H. Andrei, & J.-P. Roelot (Ed.), IAU Symposium. Vol. 264 of IAU Symposium. pp. 257–266.
- McKenzie, D. E., Hudson, H. S., Jul. 1999. X-Ray Observations of Motions and Structure above a Solar Flare Arcade. *ApJ*519, L93–L96.
- Nickeler, D. H., Wiegmann, T., Mar. 2012. Relation between current sheets and vortex sheets in stationary incompressible MHD. *Annales Geophysicae* 30, 545–555.

- Orszag, S., Tang, C., 1979. Small-scale structure of two-dimensional magnetohydrodynamic turbulence. *J. Fluid Mech.* 90, 129.
- Parker, E. N., Dec. 1957. Sweet's Mechanism for Merging Magnetic Fields in Conducting Fluids. *J. Geophys. Res.* 62, 509–520.
- Petschek, H. E., 1964. Magnetic Field Annihilation. NASA Special Publication 50, 425.
- Press, W. H., Teukolsky, S. A., Vetterling, W. T., Flannery, B. P., 2007. Numerical Recipes. Cambridge University Press, The Edinburgh Building, Cambridge CB2 8RU, UK.
- Priest, E. R., 1982. Solar Magnetohydrodynamics. Springer.
- Priest, E. R., 1984. Solar magneto-hydrodynamics. *Geophysics and Astrophysics Monographs*, Dordrecht: Reidel, 1984.
- Priest, E. R., Forbes, T., 2000. Magnetic Reconnection. Cambridge University Press.
- Rathod, H. T., Nagaraja, K. V., Ramesh, N. L., 2004. Gauss Legendre quadrature over a triangle. *J Indian Inst Sci* 84, 183–188.
- Ryu, D., Jones, T. W., Mar. 1995. Numerical magnetohydrodynamics in astrophysics: Algorithm and tests for one-dimensional flow. *ApJ* 442, 228–258.
- Ryu, D., Jones, T. W., Frank, A., Oct. 1995. Numerical Magnetohydrodynamics in Astrophysics: Algorithm and Tests for Multidimensional Flow. *ApJ* 452, 785.
- Samtaney, R., Loureiro, N. F., Uzdensky, D. A., Schekochihin, A. A., Cowley, S. C., Sep. 2009. Formation of Plasmoid Chains in Magnetic Reconnection. *Physical Review Letters* 103 (10), 105004–+.
- Schindler, K., Hesse, M., Birn, J., Jun. 1988. General magnetic reconnection, parallel electric fields, and helicity. *J. Geophys. Res.* 93, 5547–5557.
- Shibata, K., 1998. Theory of Flares ; MHD Jets. In: Koyama, K., Kitamoto, S., Itoh, M. (Eds.), *The Hot Universe*. Vol. 188 of IAU Symposium. p. 9.
- Shibata, K., Tanuma, S., Jun. 2001. Plasmoid-induced-reconnection and fractal reconnection. *Earth, Planets, and Space* 53, 473–482.
- Simnett, G. M., Tappin, S. J., Plunkett, S. P., Bedford, D. K., Eyles, C. J., St. Cyr, O. C., Howard, R. A., Brueckner, G. E., Michels, D. J., Moses, J. D., Socker, D., Dere, K. P., Korendyke, C. M., Paswaters, S. E., Wang, D., Schwenn, R., Lamy, P., Llebaria, A., Bout, M. V., Oct. 1997. LASCO Observations of Disconnected Magnetic Structures Out to Beyond 28 Solar Radii During Coronal Mass Ejections. *Sol. Phys.* 175, 685–698.
- Skála, J., Bárta, 2012. LSFEM Implementation of MHD Numerical Solver. *Applied Mathematics* 3 (11), 1842–1850.
- Skála, J., Bárta, M., Varady, M., 2011. MHD modelling of multi-scale magnetic reconnection using the Finite Element Method. *Central European Astrophysical Bulletin* 35, 195–204.
- Skála, J., Barufa, F., Rampp, M., Büchner, J., 2015. The 3D MHD code GOEMHD3 for astrophysical plasmas with large Reynolds numbers. *A&A*.
- Solin, P., 2005. Partial Differential Equations and the Finite Element Method. J. Wiley & Sons.
- Solin, P., Andrs, D., Cerveny, J., Simko, M., 2010. Pde-independent adaptive hp-fem based on hierachic extension of finite element spaces. *J. Comput. Appl. Math.* 233, 3086–3094.

- Solin, P., Cerveny, J. and Dolezel, I., 2008. Arbitrary-level hanging nodes and automatic adaptivity in the hp-fem. *Math. Comput. Simul.* 77, 117 – 132.
- Solin, P. e. a., 2012. Hermes - Higher-Order Modular Finite Element System (User's Guide). URL <http://hpfem.org/>
- Somov, B. V., 2006. Plasma Astrophysics, part I. Springer.
- Sovinec, C. R., Glasser, A. H., Gianakon, T. A., Barnes, D. C., Nebel, R. A., Kruger, S. E., Schnack, D. D., Plimpton, S. J., Tarditi, A., Chu, M. S., Mar. 2004. Nonlinear magnetohydrodynamics simulation using high-order finite elements. *Journal of Computational Physics* 195, 355–386.
- Sturrock, P. A., Aug. 1966. Model of the High-Energy Phase of Solar Flares. *Nature* 211, 695.
- Sweet, P. A., 1958. Electromagnetic phenomena in cosmic physics. Cambridge University Press, 123–134.
- Tsuneta, S., Hara, H., Shimizu, T., Acton, L. W., Strong, K. T., Hudson, H. S., Ogawara, Y., Oct. 1992. Observation of a solar flare at the limb with the YOHKOH Soft X-ray Telescope. *PASJ44*, L63–L69.
- Usoskin, I. G., Oct. 2008. A History of Solar Activity over Millennia. *Living Reviews in Solar Physics* 5, 3.
- Vlahos, L., 2007. Magnetic Complexity, Fragmentation, Particle Acceleration and Radio Emission from the Sun. In: Klein, K.-L., MacKinnon, A. L. (Eds.), *Lecture Notes in Physics*, Berlin Springer Verlag. Vol. 725 of *Lecture Notes in Physics*, Berlin Springer Verlag. pp. 15–31.
- Vlahos, L., Isliker, H., Lepreti, F., Jun. 2004. Particle Acceleration in an Evolving Network of Unstable Current Sheets. *ApJ608*, 540–553.
- Yokoyama, T., Akita, K., Morimoto, T., Inoue, K., Newmark, J., Jan. 2001. Clear Evidence of Reconnection Inflow of a Solar Flare. *ApJ546*, L69–L72.